Fundamental Physics with Laser Interferometry

Sander M. Vermeulen

Submitted for the degree of Doctor of Philosophy

Gravity Exploration Institute, School of Physics and Astronomy, Cardiff University

29th June, 2023

Supervisor: Prof. Dr. H. Grote
Co-supervisor: Prof. Dr. K. L. Dooley

Board of Examiners: Prof. Dr. S. Fairhurst
Prof. Dr. A. Freise

Preface

Laser interferometry is a technique where beams of light, created by a laser source, are superimposed to produce interference. By analysing the interfering light, perturbations that were imparted on the light beams as they travelled can be measured. The aim of the work in this dissertation is to measure thus perturbations from physical phenomena that have never been observed before.

This dissertation is a collection of work that develops, analyses, and demonstrates the use of laser interferometry to investigate the fundamental laws of Nature. It is far from a comprehensive collection; rather the subjects included became so for reasons of curiosity and opportunity. Their commonalities are arguably their relevance in fundamental physics, and consequently their planned investigation in a laser interferometry experiment being commissioned at Cardiff University.

Part of the work for this PhD at Cardiff University comprised contributions to the design and commissioning of this laser interferometry experiment, known as 'QUEST', and this is described in the first chapter. The phenomena we seek to measure with laser interferometry, in this context, are Quantum Gravity, Dark Matter, and Gravitational Waves, and each is discussed in a separate chapter of this thesis.

Much of the work covered in this dissertation has been published (or will soon be published) as articles in the literature. An overview of these articles is given below:

- Vermeulen, S. M. *et al.* "An experiment for observing quantum gravity phenomena using twin table-top 3D interferometers". *Classical and Quantum Gravity* **38,** 085008. ISSN: 0264-9381, 1361-6382 (Apr. 2021)
- Vermeulen, S. M. *et al.* "Direct limits for scalar field dark matter from a gravitational-wave detector". *Nature* **600.** ISSN: 1476-4687 (Dec. 2021)
- Aiello, L. *et al.* "Constraints on Scalar Field Dark Matter from Colocated Michelson Interferometers". *Phys. Rev. Lett.* **128,** 121101 (12 Mar. 2022)
- Ejlli, A. *et al.* "Probing dark matter with polarimetry techniques". arXiv:2211.09922, accepted for publication in Phys. Rev. D. Nov. 2022
- Stegmann, J. & Vermeulen, S. M. "Detecting the heterodyning of gravitational waves". arXiv:2301.02672, to be submitted to a journal. Jan. 2023

Summary

Laser interferometry is an experimental technique that has been developed over the past decades to achieve superlative sensitivity to changes in optical path length. This dissertation discusses the use of laser interferometers to detect quantum gravity phenomena, dark matter, and gravitational waves.

In the first chapter, the laser interferometry experiment known as QUEST is discussed, which consists of twin co-located table-top interferometers. The experiment will be sensitive to displacements of the order 10^{-19} m/$\sqrt{\text{Hz}}$ between 1-250 MHz. Emphasis is given to the development and testing of the FPGA-based high-frequency data acquisition system that performs cross-correlation and averaging of the data.

In the second chapter, the detection of quantum space-time fluctuations with laser interferometers is discussed. Contemporary literature on holographic quantum space-time fluctuations is reviewed. A basic model for computing interferometric signals from quantum space-time fluctuations is formulated, and prospects of detecting a signal with QUEST are analysed.

In the third chapter, we demonstrate the use of laser interferometry to search for scalar field dark matter. Analysis of the data from the GEO600 gravitational-wave detector and the Fermilab Holometer for the presence of dark matter signals was performed; no signals were detected, and constraints are placed on dark matter coupling strengths that exceed previous constraints by orders of magnitude. A polarimetric experiment to search for scalar and pseudoscalar dark matter is proposed, and we discuss prospective dark matter searches with QUEST.

In the fourth chapter, we present a new approach for detecting gravitational waves using existing and future detectors that exploits the mixing, or heterodyning, of gravitational waves. We show that this method could allow gravitational-wave detectors such as LISA to detect low-frequency gravitational waves outside of their designed bandwidth using the same infrastructure. We also comment on the prospects of detecting high-frequency (MHz) gravitational waves with QUEST.

Contents

1: The QUEST Experiment

In this chapter, the QUEST experiment is discussed. The QUEST experiment consists of two identical table-top laser interferometers, with the primary purpose of detecting the noise produced by holographic quantum space-time fluctuations. The experiment will be sensitive to displacements of the order 10^{-19} m/$\sqrt{\text{Hz}}$ in the MHz band (1-250 MHz), and will also be used to search for high-frequency gravitational waves and certain kinds of dark matter. The laser interferometers are built using technologies originally developed for the construction of gravitational-wave detectors. Cross-correlation of signals from the two co-located interferometers will be used to significantly enhance the sensitivity of the experiment.

Contributions to published work in this chapter

Sections 1.2.3, 1.2.4, 1.3, 1.5 of this chapter are based on parts of the article

- Vermeulen, S. M. *et al.* "An experiment for observing quantum gravity phenomena using twin table-top 3D interferometers". *Classical and Quantum Gravity* **38,** 085008. ISSN: 0264-9381, 1361-6382 (Apr. 2021).

S.M.V. lead the writing of that manuscript, and produced the majority of the content and text of the manuscript, with the exception of sections 5.1, 6, and a part of section 7 therein [1].

1.1 Introduction: The QUEST Experiment

Laser interferometers were extensively developed in the decades-long effort to develop a gravitational-wave detector. This effort produced interferometers that are sensitive to displacements on the order of 10^{-19} m, significantly exceeding other methods of measuring lengths, and enabling length measurements with a relative uncertainty better than one part in 10^{23}[6]. The highly sensitive interferometers built by the LIGO collaboration made the first detection of gravitational waves in 2015 [7].

It was realised by many that such sensitive instrumentation could potentially be applied to measure other physical phenomena with unprecedented sensitivity. This requires the phenomenon to interact with the light in the interferometer and hence perturb the interference pattern such that a signal is produced. The QUEST experiment, which comprises a pair of table-top laser interferometers, was motivated in particular by proposals to use laser interferometry to observe quantum fluctuations of space-time [8–11]. Additionally, the experiment will be used to search for certain proposed kinds of dark matter [12, 13] with unprecedented sensitivity. By design, the QUEST experiment will be the most sensitive gravitational-wave detector in its respective frequency band [14, 15], and will therefore also allow the detection or exclusion of the presence of high-frequency (MHz) gravitational waves above a certain amplitude.

A quantitative understanding of the coupling between the phenomenon of interest and the laser interferometer is required to assess the scientific potential of an experiment, to inform the exact design of the interferometer, and to interpret the measurements produced by the instrument. In this thesis, the last sections of the next chapters (i.e. 2.4, 3.6, and 4.3) explicate the scientific prospects of the QUEST experiment for detecting the fundamental physical phenomena of interest.

1.1.1 History of the QUEST Experiment

The QUEST experiment was conceived primarily as a follow-up to the Fermilab Holometer [16], a pair of co-located and co-aligned laser interferometers with 40-m arms. The Holometer was built to look for an exotic form of noise hypothesised to arise due to the holographic quantum nature of gravity [17] (see Chapter 2). No such signals were found in the initial phase of the Holometer programme [18]. It was then postulated that the holographic quantum gravity noise could only be detected in a configuration where the arms of the interferometer do not extend purely radially from the beamsplitter [19, 20]. The Fermilab Holometer was therefore reconfigured with a 'bent' arm [21], and more measurements were performed. Again, no signal was found [21] and the experiment has now been decommissioned.

It was argued by the Holometer collaboration that a table-top experiment, with

improved sensitivity, would be suited to continue a search for signatures of quantum gravity. The QUEST experiment initially planned for an arm design similar (but shorter by a factor 10) to that of the Holometer, where one arm of each interferometer is 'bent' at 90 degrees by a mirror halfway along the arm (see Fig. 2.3). However, after reviewing the developing literature [8, 22], this author argued that the interferometers should not use bent arms, and that a design with straight arms where the angle between the arms can be reconfigured (see Sec. 1.2.2) was better motivated.

1.1.2 Improvements over the Fermilab Holometer

The individual interferometers of the Holometer have reached a sensitivity to displacements of the order of $10^{-18}\,\mathrm{m}/\sqrt{\mathrm{Hz}}$ at frequencies between 1 and 25 MHz, limited by photon shot noise. The main improvements to the design that will allow QUEST to surpass the displacement sensitivity of the Holometer are the inclusion of optical mode cleaners, higher optical input power, and the injection of squeezed states of light, which all will allow for the mitigation of photon shot noise (see Secs. 1.2, and 1.3). The displacement sensitivity of the individual interferometers of QUEST is projected to be better than that of the Holometer by an order of magnitude, and the projected sensitive frequency band of QUEST, between 1 and 250 MHz, is also greater by an order of magnitude (see Sec 1.5).

The compact table-top design allows the experiment to be built on a single vibration-isolated optical bench in a laboratory under stable environmental conditions. This will mitigate environmental noise to enhance sensitivity at lower frequencies, and help keep the interferometer at its operating point (reducing the occurrence of 'lock loss'), which improves the experiment's duty cycle.

Moreover, the small scale of QUEST will allow the above-mentioned reconfiguration of the interferometer geometry, e.g. a change of the angle between the arms at the beamsplitter.

For comparison, the main experimental parameters for both the Holometer and the QUEST experiment are summarised in Table 1.1.

1.1.3 Present and Future of the QUEST experiment

At the time of writing, the QUEST experiment is being commissioned and is expected to start its measurement campaign within the coming year. It is expected that the accuracy of the measurements will be limited by random noise (specifically quantum shot noise, see Sec. 1.3.1).

The observable of primary interest in the QUEST experiment is the cross-correlation of length changes in the two interferometers; all physical phenomena of interest (quantun space-time fluctuations, dark matter, and gravitational waves) are hypothesised to

Table 1.1. The main experimental parameters for both the Fermilab Holometer and the QUEST experiment are summarised. Here, 'Effective CD' is the effective contrast defect, defined as the ratio of the power as measured on the photodetector and the circulating power at the beamsplitter on a minimum of the interference pattern. This is different from the more conventional definition of the CD in Sec. 1.3, which would not allow for a direct comparison of the CD due to the absence of an OMC in the Fermilab Holometer. Detected SQZ is the level of light squeezing as detected at the output (see Sec. 1.3.1); squeezing is not employed in the Fermilab Holometer.

Parameter	*Fermilab*	*QUEST (planned)*
Optical path length	40 m	3 m
Input power	2 W	10 W
Circulating power	2 kW	10 kW
Bandwidth	25 MHz	250 MHz
Effective CD	$2 \cdot 10^{-5}$	$< 10^{-6}$
Detected SQZ (initial/final target)	–	6/10 dB

produce correlated signals in the two interferometers [1]. As with any measurement that is limited by a random error, the accuracy of the measurement can be improved by acquiring more data and taking the average, whereby statistically the accuracy improves with the square root of the number of measurements. Therefore, the average cross-correlation can be measured with an accuracy that increases as more data is collected, and phenomena that produce correlated signals can be resolved over time (see Sec. 1.2.1).

For the QUEST experiment, the plan is to initially accumulate data for a total time of 10^6 s. Given that QUEST's interferometers perform as designed (see Sec. 1.5), this amount of data will provide an effective integrated sensitivity that exceeds that of the Fermilab Holometer, enabling the possible detection of new physics.

1.2 Overview of the Experimental Design

The QUEST experiment comprises two sensitive laser interferometers that incorporate many of the technologies developed for the construction of gravitational-wave detectors. In this section, we give an overview on the experimental strategy and design of the QUEST experiment.

1.2.1 Cross-correlation of Twin Interferometers

The sensitivity of the QUEST experiment to quantum space-time fluctuations, gravitational waves, and dark matter will be achieved through cross-correlation of the signals from two interferometers. A custom-designed FPGA-based data acquisition system will sample the signals from the interferometers at $f_s = 500$ MHz and perform real-time cross-correlation and integration of the data, as detailed in Sec. 1.4.

This cross-correlation approach exploits the fact that given a signal that is correlated between two detectors, and given noise that is not, the cross-spectrum converges to the correlated signal over time. As shot noise is expected to be the dominant in the interferometer outputs (see Sec. 1.3), this uncorrelated noise can be averaged down significantly over time to reveal underlying correlated signals. Specifically, the sensitivity, defined as the magnitude of the noise cross power spectral density (CSD), is the geometric mean of the noise auto power spectral densities of the individual interferometers (PSD1, PSD2), and scales with the inverse square root of the total measurement time T_{tot} in the absence of correlations [16, 23], i.e.

$$|\text{CSD}(f)| = \sqrt{\frac{\text{PSD1}(f) \cdot \text{PSD2}(f)}{N_{\text{spec}}}} \propto \sqrt{\frac{1}{T_{\text{tot}}}}, \tag{1.1}$$

where N_{spec} is the number of measured spectra.

Unlike uncorrelated noise, correlated noise cannot be averaged down as in Eq. 1.1, and will manifest as an irreducible noise floor in the cross-spectrum. A primary concern in achieving high sensitivity will be the reduction of noise that is correlated between the interferometers. The elimination of such noise comes down to perfecting the isolation between the instruments and removing external noise sources that are coherent on scales greater than the separation between the instruments.

While it can be shown that the time-averaged CSD does not provide more statistical power than the two time-averaged auto-spectra from the individual interferometers (PSD1, PSD2) combined [24], there are significant practical advantages to analysing the former data product. To discern an unknown signal from quantum space-time fluctuations in the time-averaged PSDs, one could look for excess (unexplained) spectral power in these auto-spectra. To do this, all known sources of noise would need to

be accurately subtracted from the mean auto-PSDs, such that the residual PSD can be confidently attributed to the unknown signal. In other words, if the error on the estimation of the known noise auto-PSD is greater than the signal, the signal can never be identified. As the signal of interest is predicted to be $\gtrsim 3$ orders of magnitude smaller than the expected shot noise, the known noise would have to be quantified with an uncertainty much less than $1/10^3 = 0.1\%$ to be accurately subtracted from the mean. This would also require calibration of the experiment to that accuracy. In addition, any non-stationarity of the interferometer noise would need to be quantified and accounted for when analysing the auto-PSDs. No subtractions have to be performed on the cross-spectrum, which drastically simplifies the experiment (as there is no need for extremely accurate calibration) and the data analysis.

1.2.2 Reconfigurable Geometry

The initial stage of the QUEST experiment will use twin co-located interferometers with a 1.8-m arm length. The angle between the arms γ can be varied, which will allow the experiment to test theories that predict a characteristic angular correlation pattern of quantum gravity fluctuations (see Sec. 2.2.5). The reconfiguration of the inter-arm angle can in theory be done without having to replace any components (with the exception of the beamsplitter). The central vacuum chambers that house the beamsplitter and power-recycling mirrors have been designed with a large number of flanges around their circumference to facilitate reconfiguration; the flanges are spaced such that the inter-arm angle γ can be set to seven angles between 10° and 170°. To further facilitate reconfiguration of the interferometer arms, the injection optics (laser, amplifier, mode-matching telescope, etc.), the detection optics (optical mode cleaner, photodiodes, etc.), and the squeezed light sources, are all placed on their own breadboards that can easily be moved across the optical bench.

A future stage of the experiment may feature a 3D geometry with arms that include a radial and a non-radial segment to introduce a sensitivity to transverse quantum space-time fluctuations (see Sec. 2.3).

1.2.3 Optics

An overview of the optical layout of a single interferometer of QUEST is shown in Fig. 1.2. The input light for each interferometer will be provided by a tunable continuous-wave laser (Coherent Mephisto), with a maximum optical output power of 0.5 W at a wavelength of 1064 nm. A total input power of up to 20 W will be achieved through the use of optical amplification stages (neoLASE). The addition of an input mode cleaner to suppress non-resonant optical modes and provide temporal filtering of the input beam is being considered. A beamsplitter with one reflective and one anti-reflective surface

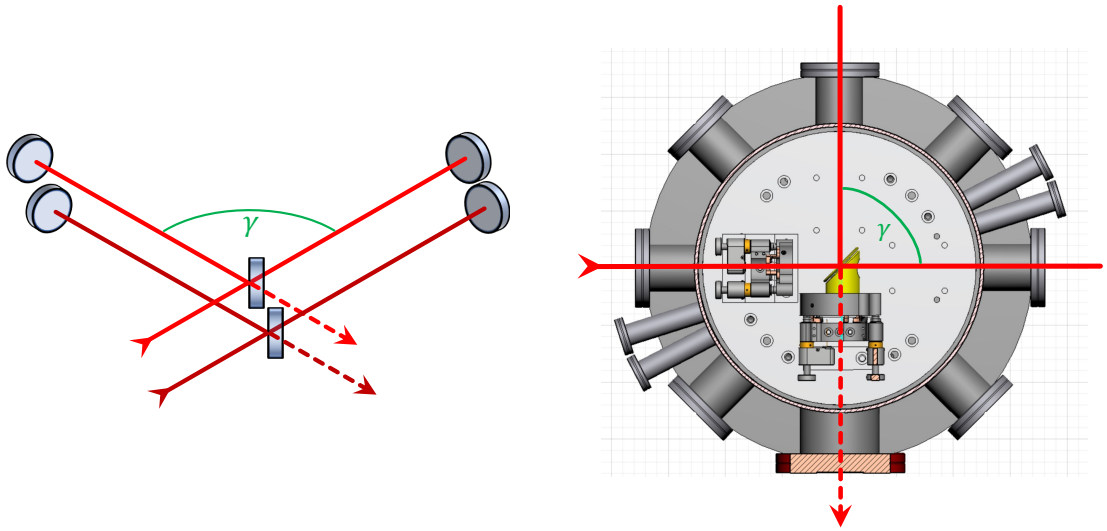

Figure 1.1. The initial geometrical configuration of QUEST's twin co-located interferometers (left) and a top view of the design of the central vacuum chambers that house the beamsplitters (right). The arms will comprise a single radial segment with a length of 1.8 m, and the inter-arm angle γ can be varied between 10° and 170° by using different flanges around the circumference of the central vacuum chamber for the arms and the input and output beams. The diagram of the central vacuum chamber shows the mounts for the beamsplitter and the power-recycling mirror in the interior, which would need to be reconfigured when changing the inter-arm angle.

will split and recombine the light into and from the arms with a 50:50 ratio. The co-located interferometers are designed to operate with circulating optical powers of roughly 10 kW by using a power-recycling configuration [25]. The power-recycling cavity of each interferometer will be compounded by the interferometer arms, delimited by two concave end mirrors and a single flat power-recycling mirror. The spatial mode and frequency of the input light will be tuned to the power-recycling cavity so that resonant build-up of the light occurs. The interference pattern produced by light from the two arms will be imaged on a photodetector in the output channel. Between the beamsplitter and the photodetector, an optical mode cleaner (OMC) will be installed to suppress higher-order spatial modes of light in the output channel. In addition, squeezed vacuum states of light, produced using a dedicated setup known as a squeezer [26, 27], will be injected into the optical paths of the interferometers through a Faraday rotator, which will allow quantum noise to be reduced (see Sec. 1.3.1). Signals will be obtained using DC-readout [28, 29].

1.2.4 Vacuum System

The twin interferometers will each be built in independent but identical vacuum systems that will contain the optics from the power-recycling mirrors to the end mirrors. The rest of the optics, such as the output (and input) mode cleaners, injection optics, and squeezers, will be built in air, to allow for easier manipulation. Each of the twin vacuum systems will consist of three cylindrical vacuum chambers. A single, larger chamber will house the power-recycling mirror and beamsplitter, and two slightly smaller chambers will accommodate the end mirrors. To connect the vacuum chambers and allow for alignment, stainless steel vacuum tubes with short bellows at the ends will be used, which connect with adjoining vacuum chambers through manual gate valves. To maximise the options for intervention and adjustment, each vacuum chamber will have its own mechanical (turbo-molecular) pumps, pressure gauges, and valves for vacuum isolation. This feature will contribute to the fast reconfigurability of the geometry of the interferometers.

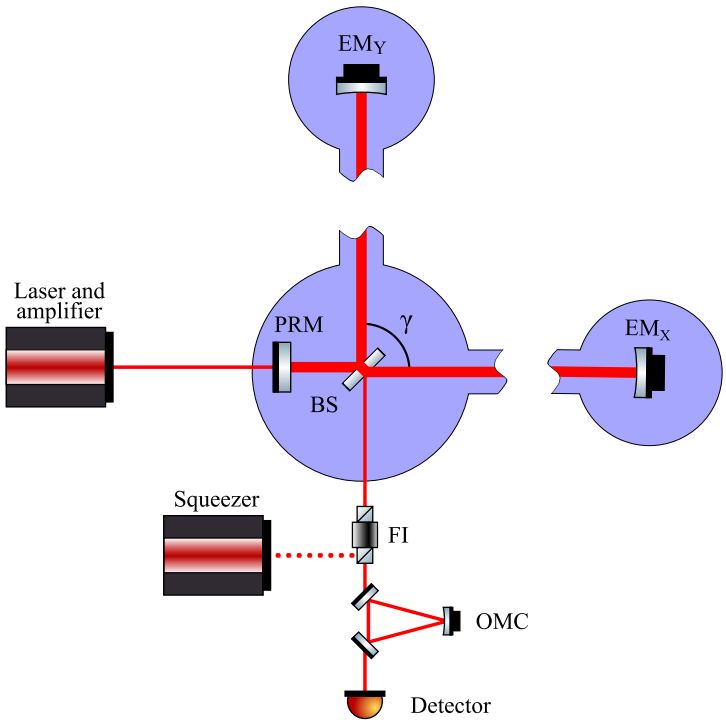

Figure 1.2. Simplified optical layout of a single power-recycled interferometer of the QUEST experiment. Up to 20 W of input power will be provided by a 1064 nm laser and optical amplifiers. The frequency and spatial mode of the input laser beam will be tuned to be resonant with the power-recycling cavity, causing a build-up of circulating optical power of ~ 10 kW. The power-recycling cavity is delimited by the flat power-recycling mirror (PRM) and the concave end mirrors ($EM_{X,Y}$). A 50:50 low-absorption beamsplitter will split and recombine the light in the two arms. The angle between the arms γ can be varied. At the output of the interferometer, an optical squeezer will be used to inject squeezed vacuum states of light into the interferometer through a Faraday rotator (FI) to reduce quantum noise. An output mode cleaner (OMC) will suppress higher-order optical modes in the output channel. Shaded areas represent vacuum chambers.

1.3 Mitigation of Noise

As can be seen in Eq. 1.1, the cross-correlated sensitivity is linear in the geometric mean of the interferometer auto-PSDs, and inversely proportional to the square root of the measurement time. Decreasing the level of uncorrelated stochastic noise in each interferometer is therefore a primary strategy towards increasing the sensitivity in the integrated cross-spectrum. In this section, the sources of different kinds of noise and the strategies for their mitigation are discussed, as summarised in Table 1.2.

Noise Source	*Mitigation Strategy*
Shot noise	High input power, power recycling, squeezed states of light
Additional shot noise due to contrast defect	High-performance optics and alignment, output mode cleaner
Seismic and acoustic noise	Vibration-isolated optical bench, quiet cleanroom environment
Residual gas noise	Ultra-high-vacuum system
Noise from stray light	Baffles in vacuum tubes (optional)
Thermal noise	No mitigation needed

Table 1.2. Relevant sources of noise and strategies for their mitigation.

1.3.1 Shot Noise

Shot noise at the Standard Quantum Limit

It is evident in similar state-of-the-art interferometry experiments, specifically gravitational wave interferometers and the Fermilab Holometer, that the maximum experimentally attainable sensitivity in the MHz range is currently limited by photon shot noise with a magnitude that is given by the standard quantum limit for optical interferometers [30].

The origin of this type of noise is the Heisenberg uncertainty relation for the particle number and phase observables of an optical state,

$$\Delta N_\gamma \, \Delta\phi \geq 1, \tag{1.2}$$

where ΔN_γ and $\Delta\phi$ are the root mean square (RMS) uncertainty of the number of photons N_γ and the phase ϕ. The uncertainty of the phase, which is the observable measured through interference at the beamsplitter, is equivalent to an uncertainty in

the length measured with the interferometer:

$$\Delta L = \frac{\lambda \Delta \phi}{2\pi} \tag{1.3}$$

The RMS uncertainty of the number of photons is described by Poisson statistics, and is related to the power of the optical state P as

$$\Delta N_\gamma = \sqrt{N_\gamma} = \sqrt{\frac{P_{BS}\tau}{\hbar\omega}}, \tag{1.4}$$

where τ is the total measurement time, ω the angular frequency of the light, and we consider the optical state at the beamsplitter with power $P = P_{BS}$. For a coherent optical state, the Heisenberg uncertainty relation (1.2) is an exact equality i.e. $\Delta N_\gamma = 1/\Delta\phi$. Thus, combining the two equations above, there is a lower limit on the uncertainty of measured length

$$\Delta L = \frac{\lambda \Delta \phi}{2\pi} = \frac{\lambda}{2\pi \Delta N_\gamma} = \sqrt{\frac{c\hbar\lambda}{2\pi P_{BS}\tau}}, \tag{1.5}$$

where we used that $\omega = (2\pi c)/\lambda$. This lower limit on interferometric length measurements is known as the standard quantum limit (SQL)[30]. Given a series of length measurements each of duration $\tau = 1/f_s$, one can compute the corresponding RMS amplitude spectral density $S_{\Delta L}(f)$ of the apparent displacements ΔL using that by definition [31]:

$$\int_0^{\mathrm{f_s}} S_{\Delta L}(f) df = \frac{\Delta L}{\sqrt{2}}. \tag{1.6}$$

If the noise is assumed to be constant at all frequencies (white), the shot noise amplitude spectral density is thus [30, 32]

$$S_{\Delta L}^{\mathrm{SQL}}(f) = \sqrt{\frac{c\hbar\lambda}{4\pi P_{BS}}}. \tag{1.7}$$

It can be seen that the RMS amplitude of the shot noise depends inversely on the circulating power at the beamsplitter P_{BS}.

Measured shot noise at the photodetector

The SQL (Eq. 1.7) represents a fundamental lower limit on the displacement noise for an interferometric measurement on a coherent state. In practice, the measured photon shot noise is often greater. The measured shot noise manifests as fluctuations of the current produced by a photodetector at the output of the interferometer; these current fluctuations can equivalently be described as fluctuations of the optical power of the

light at the output. Power fluctuations ΔP can be expressed in terms of fluctuations of the number of photons and can be shown to be proportional to the square root of the power:

$$\Delta P = \frac{\Delta N_\gamma \hbar\omega}{\tau} = \sqrt{\frac{\hbar\omega P}{\tau}}, \implies \Delta P \propto \sqrt{P}, \tag{1.8}$$

where we used Eq. 1.4 for the second equality.

To calculate the total amount of shot noise in terms of power fluctuations, we consider the output power P_{out} in a realistic interferometer that uses DC-readout, where a deliberate offset from the dark fringe Φ_{off} is used [28]. We further consider a small differential optical phase between the arms φ to exist, which could be due to e.g. a signal. Lastly, we take into account the existence of differential imperfections between the interferometer arms, which yields different amounts of light in each arm. Because of this, the contrast of the interference pattern is imperfect and an amount of extra power $P_{\text{CD}} = P_{BS} \cdot \text{CD}$ (where CD is the dimensionless contrast defect, see below) is present at the output that does not depend on the differential optical path length between the arms. The output power is thus [33]

$$P_{\text{out}} = P_{BS} \sin^2(\varphi + \Phi_{\text{off}}) + P_{\text{CD}} \tag{1.9}$$

$$\approx P_{BS} (\varphi + \Phi_{\text{off}})^2 + P_{\text{CD}} \tag{1.10}$$

$$\approx P_{BS} \left(2\varphi\Phi_{\text{off}} + \Phi_{\text{off}}^2 + \text{CD}\right) = P_\varphi + P_{\text{off}} + P_{\text{CD}}, \tag{1.11}$$

where we used the small angle approximation and neglect terms $\mathcal{O}(\varphi^2)$; $P_\varphi = 2P_{BS}\varphi\Phi_{\text{off}}$, and $P_{\text{off}} = P_{BS}\Phi_{\text{off}}^2$. The total RMS power fluctuation at the photodetector, i.e. the measured shot noise, is then

$$\Delta P_{\text{out}} = \sqrt{(\Delta P_\varphi)^2 + (\Delta P_{\text{off}})^2 + (\Delta P_{\text{CD}})^2} \propto \sqrt{P_{BS}}\sqrt{2\varphi\Phi_{\text{off}} + \Phi_{\text{off}}^2 + \text{CD}}, \tag{1.12}$$

where we add fluctuations in quadrature and we used Eq. 1.8. Moreover, we evaluate the signal-to-shot-noise ratio (SNR)

$$\text{SNR} = \frac{P_\varphi}{\Delta P_{\text{out}}} \propto \frac{2\varphi\Phi_{\text{off}}\sqrt{P_{BS}}}{\sqrt{2\varphi\Phi_{\text{off}} + \Phi_{\text{off}}^2 + \text{CD}}}, \tag{1.13}$$

which can thus be seen to increase with the square of the power at the beamsplitter, and to decrease due to the contrast defect.

We note that a measured change in output power P_φ corresponds to a measured differential displacement

$$\delta L = \frac{\lambda P_\varphi}{4\pi\Phi_{\text{off}} P_{BS}}. \tag{1.14}$$

If we set the differential phase between the arms equal to the minimum phase uncertainty of a coherent optical state in this equation, i.e. $\varphi = \Delta\phi = 1/\Delta N_\gamma$ and plug in Eq. 1.4, we recover the minimum displacement uncertainty as given by the standard quantum limit (i.e. Eq. 1.5 with $\Delta L = \delta L$).

To increase the signal-to-shot-noise ratio, the QUEST experiment will employ power recycling to reach high circulating optical powers, which thus allows the effective mitigation of shot noise according to Eqs. 1.5 and 1.12 [34]. In order to improve the detector sensitivity beyond the standard quantum limit for coherent states (Eq. 1.7), squeezed states of light will be used [27]. Independent or entangled squeezed vacuum states will be injected into the anti-symmetric ports of the interferometers [35]. The initial target is to reach a level of detected squeezing of around 6 dB (this level has recently been reached in GEO 600 [36], and is double that currently used in Advanced LIGO [37]). A goal for a future stage will be to achieve 10 dB of detected squeezing.

Contrast defect and higher order modes

As mentioned above, in a realistic interferometer the light power in the two arms is not equal, and perfect destructive interference cannot occur which produces excess output power. We focus here on the contrast defect due to the imperfect destructive interference of higher order optical modes (HOMs)[1] at the beamsplitter, which is expected to be the dominant contribution to the CD[1]. HOM light at the anti-symmetric port is a significant part of the CD in state-of-the-art interferometry experiments, such as gravitational wave detectors and the Fermilab Holometer. These interferometers use DC-readout, and as such operate at a small offset from the dark fringe [28, 29]. Ideally, the magnitude of the offset is chosen such that the CD represents an insignificant fraction of the power incident on the photodetector compared to the TEM00 light due to this intentional dark fringe offset. If there is a significant amount of HOM light at the output, this would require operating at a large offset, which has the disadvantage that noise from other sources is more strongly coupled to the output [28, 29]. In addition, a large offset to dominate significant amounts of HOM light would entail high power incident on the photodetector, which is undesirable, as high-bandwidth photodetectors are subject to technical limitations at high incident power. This therefore effectively constrains the circulating power that can be used in the interferometers, which in turn limits the shot-noise mitigation that can be achieved.

The QUEST experiment will be designed with a target of attaining a CD due to TEM00 light $< 10^{-6}$, and a CD due to HOM light $< 10^{-5}$. As a reference, the lowest

[1]The fundamental Gaussian optical mode (TEM00) is the lowest order solution of the paraxial wave equation. An infinite number of higher-order solutions exist which are referred to as higher-order modes [38].

CD reported in the Fermilab Holometer was about $2 \cdot 10^{-5}$ [39]. The latter requirement is less stringent, as the contribution of HOM light will be reduced by at least an order of magnitude at the output by including an optical mode cleaner (OMC) in the output channel of each interferometer (see Fig. 1.2), with the target of suppressing HOM power by at least an order of magnitude (OMCs are also employed in gravitational wave detectors, but not in the Fermilab Holometer). The addition of the OMCs will reduce the amount of HOM light incident on the photodetectors, thereby facilitating the use of a smaller dark fringe offset. The OMCs will thus not only improve the shot-noise-limited sensitivity directly by suppressing the HOM power, but also by allowing higher circulating power within the interferometers. The relevant parameters for the suppression of HOM light using an OMC are summarised in Table 1.3.

Table 1.3. Experimental parameters concerning the suppression of shot noise due to contrast defect from higher order optical modes using an optical mode cleaner. The CD is the ratio of the circulating power and the power at the ant-symmetric port as measured on a dark fringe, before the OMC. The OMC will suppress HOM light by at least an order of magnitude to yield an effective CD at the output of $< 10^{-6}$ such that the experiment will be limited by shot noise due to vacuum fluctuations.

Parameter	*Value*
CD target (TEM00/HOM light)	$<10^{-6}/<10^{-5}$
OMC HOM power suppression factor	≥ 10
OMC Finesse	> 11
OMC bandwidth	200 MHz
OMC round-trip length	< 13.5 cm

1.3.2 Seismic Noise, Residual Gas Noise, & Scattered light

Seismic vibrations, air turbulence, and acoustic noise cause the most problematic low-frequency noise in interferometry, as these sources produce phase noise through various coupling mechanisms. Seismic noise is filtered at higher frequencies by the vibration-isolated optical bench that the QUEST experiment will be placed on. Therefore, the effect of seismic noise on the displacement amplitude spectral density of the interferometer at frequencies above 1 MHz is expected to be below that of the shot noise by more than an order of magnitude. Environmental noise on the input beam due to air turbulence and dust will be mitigated by placing the whole apparatus in a quiet Class 10000 cleanroom with an air circulation and filtration system.

Fluctuations in the density of the residual gas in the vacuum system causes fluctuations of the absolute phase of the light which will manifest as phase noise in the

fundamental optical output mode. It was found [1] that the residual gas displacement noise as estimated using the results in [40] for a vacuum pressure $< 10^{-6}$ mbar will be less than the displacement shot noise by more than one order of magnitude at all frequencies. Another mechanism through which residual gas degrades the sensitivity is the absorption of light by hydrocarbons deposited onto optical surfaces. The deposition rate depends linearly on the residual gas pressure, as detailed in [39]. To increase the time needed to deposit a single hydrocarbon monolayer on an optical surface to six months, which corresponds to an increment of the coating absorption of 20 ppm, a vacuum with a pressure of $\leq 10^{-7}$ mbar will be used.

Another non-negligible source of noise is stray light produced by specular and diffuse reflections of light by dust or imperfections on the optical components. Specifically, it was found in gravitational-wave detectors that the coupling of seismic noise to vibrational excitations of interferometer components leading to phase modulation of stray light was a significant source of noise [41]. The QUEST experiment will be sensitive at much higher frequencies than ground-based gravitational wave detectors such as LIGO. Therefore, we expect the contribution of noise due to stray light modulated by seismic noise to be negligible. However, in case significant noise from stray light is present, this may be suppressed by installing baffles in the vacuum tubes that connect the chambers that house the mirrors.

The thermal excitation of atoms, or Brownian motion, excites the mechanical vibration modes of optical elements and as a consequence generates displacement fluctuations of the reflective surfaces. Given the dimensions and material properties of the optical elements, it is expected that the fundamental vibration mode and its harmonics lie at ≈ 477 kHz and multiples thereof. As this part of the thermal noise, which is expected to exceed the shot noise, consist of a number of narrow resonance peaks, it need not be mitigated. These peaks can be excluded in the data analysis with at the cost of a small reduction in useful signal bandwidth. It is expected that the thermal noise from Brownian motion in the optical coatings lies more than an order of magnitude below the shot noise level.

1.4 High-Frequency Data Acquisition System

This section describes the design and implementation of the high-frequency data acquisition system (HF-DAQ) for the QUEST experiment. The HF-DAQ digitises the output signals of the interferometers at 500 MHz, and performs FPGA-based real-time cross-correlation and averaging on the data.

1.4.1 Scientific Design Requirements

The primary signal of interest for the QUEST experiment is that produced by hypothetical holographic quantum fluctuations of space-time (Sec. 2.2). The time-domain correlation length of such a signal is predicted to be given by the light-crossing time of the interferometer, L/c. Correspondingly, the frequency-domain signal is predicted to be strongest on the order of the light-crossing frequency, c/L. The signal is also predicted to be relatively broadband (see Sec. 2.4). In order to fully resolve the desired signal in the output of the interferometer, data must therefore be collected with a time resolution higher than the light-crossing time. More practically, this means the electronic signal from the photodiodes at the output of the interferometer must be sampled and digitised at a frequency greater than twice the light-crossing frequency, $2c/L$ (according to the Nyquist-Shannon sampling theorem), which is roughly 300 MHz for the current configuration of the QUEST experiment. In addition, acquiring data over a greater frequency band is desirable, as it allows one to search a larger part of the parameter space of possible signals from parametrically modelled sources, e.g. dark matter and gravitational waves.

The design of the QUEST experiment uses twin co-located interferometers under the assumption that any signal of interest will be common to both instruments. The output signals of the interferometers are predicted to be dominated by shot noise; the correlated signals of interest superposed on this noise are predicted to have an amplitude several ($\gtrsim 3$) orders of magnitude smaller than that of the noise. To filter out a common signal from the noise-dominated interferometer signals, cross-correlation has to be performed. To make optimal use of time and avoid the need for dedicated processing time after acquisition, cross-correlation has to be done at the same rate as data is acquired (i.e. real-time). As the signal from quantum space-time fluctuations is predicted to be time-invariant (stationary), the data may be averaged over time to improve the signal-to-noise ratio. This averaging would also compress the data, preventing the need for large amounts of data to be stored.

Given the requirement on the acquisition frequency, the necessarily high resolution of the data points, and the aim to perform real-time cross-correlation and averaging on the data, significant processing performance is required of the data acquisition system.

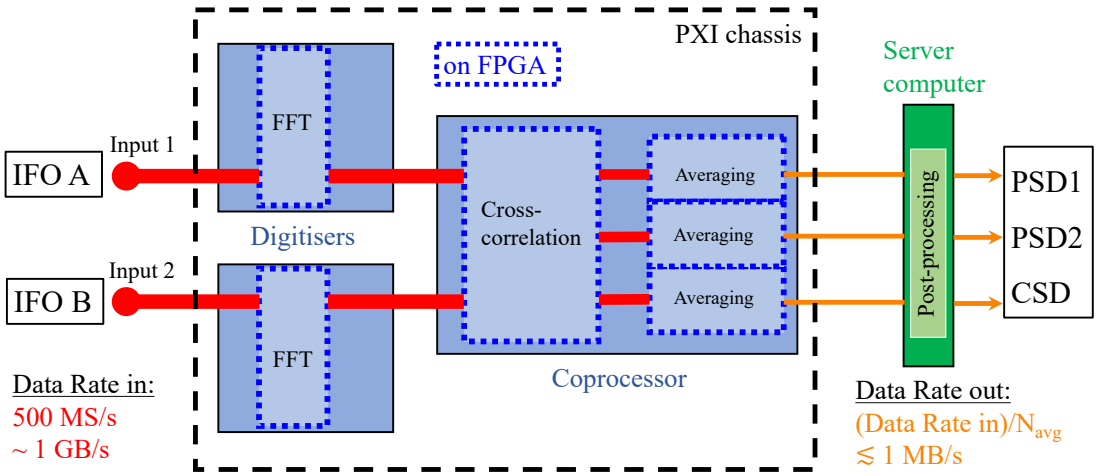

Figure 1.3. Diagram of the high-frequency data acquisition system of the QUEST experiment. Analog electronic signals from the photodetectors of each of the two interferometers (IFO A, IFO B) are sampled and digitised at a rate of 500 MSamples/s by digitisers, producing two raw data streams with a combined data rate of ~ 1 GB/s (red lines). The data is transformed to the frequency domain through an FFT implemented on the digitisers' on-board FPGAs. The spectral data is then sent from the digitisers to the coprocessor across the backplane of the PXI chassis that houses the digitisers and coprocessor. Next, cross-correlation of the data is performed on the coprocessor's FPGA, producing three data streams that correspond to the two auto-spectra (PSD1, PSD2) and one cross-spectrum (CSD) of the two inputs. Averaging on the coprocessor's FPGA reduces the data rate by a factor equal to the chosen number of averages ($N_{\text{avg}} = 10^3 - 10^6$), producing an output data rate of $\lesssim 1$ MB/s (orange lines). A server computer controls the digitisers and coprocessor and post-processes and stores the final data.

1.4.2 Design and Configuration

Hardware

The requirements above motivate the use of high-frequency high-resolution analog-to-digital converters (ADC). The HF-DAQ contains two identical 500-MS/s, 16-bit, 4-channel digitisers (NI PXIe-5763), one for each interferometer. The data is transformed to the frequency domain on the digitisers' on-board Xilinx Kintex UltraScale KU035 FPGAs. To perform real-time cross-correlation and averaging, we use an FPGA coprocessor module that contains a Xilinx Kintex UltraScale KU060 FPGA (NI PXIe-7915). The averaging reduces the data rate by a configurable factor of $10^3 - 10^6$. The digitisers and coprocessor are housed in a PXI chassis (NI PXIe-1092) connected to a server computer (Dell PowerEdge R7525), which receives the processed data and controls the digitisers and coprocessor. Communications between the PXI chassis and the server are implemented using a PXI remote control module (NI PXIe-8398).

Processing algorithm

The analog voltage signals from interferometers A and B are sampled by the digitisers with constant frequency f_s, which produces a stream of discrete data points

$$x_n^{A,B}, \quad n = 0, 1, \ldots, N_{\text{tot}} - 1, \tag{1.15}$$

where the time interval between points is $t_s = 1/f_s$, and the total number of points is $N_{\text{tot}} = \lfloor T_{\text{tot}} f_s \rfloor$, where T_{tot} is the total measurement time. Successive segments of L_{FT} data points are subjected to a discrete Fourier transform (DFT) to yield the spectra

$$S_{kl}^{A,B} = \sum_{n=lL_{FT}}^{(l+1)L_{\text{FT}}-1} x_n^{A,B} \cdot e^{-2\pi i \frac{kn}{L_{\text{FT}}}}, \tag{1.16}$$

where $k = 0, 1, \ldots, L_{\text{FT}} - 1$ denotes the frequency bin number, and $l = 0, 1, \ldots, N_{\text{spec}} - 1$, where $N_{\text{spec}} = N_{\text{tot}}/L_{\text{FT}}$. As the voltage measurements x_n are real,

$$S_{(L_{\text{FT}}-k)\,l}^{A,B} = S_{kl}^{A,B} \in \mathbb{C}, \tag{1.17}$$

and therefore the DFT transforms L_{FT} real time-domain data points into $(L_{\text{FT}}/2) + 1$ unique complex frequency-domain data points. Almost half of the frequency bins are therefore redundant, and the non-redundant bins correspond to the frequencies

$$f_k = k\frac{f_s}{L_{\text{FT}}}, \quad k = 0, 1, \ldots, \frac{L_{\text{FT}}}{2} - 1, \tag{1.18}$$

such that $S_k = S(f_k)$ is the Fourier coefficient at frequency f_k, and the frequency resolution is $\Delta f = f_s/L_{\text{FT}}$. The cross-spectrum of interferometers A and B, which fully captures cross-correlations encoded in the time-domain data, is computed as

$$S_k^{AB} = S_k^A (S_k^B)^* \in \mathbb{C}. \tag{1.19}$$

The auto power spectra are also computed for each interferometer:

$$S_k^{AA} = S_k^A (S_k^A)^* \in \mathbb{R}, \quad S_k^{BB} = S_k^B (S_k^B)^* \in \mathbb{R}. \tag{1.20}$$

We add together consecutive batches of $N_{\text{avg}} < N_{\text{spec}}$ spectra to create the averaged spectra

$$\begin{aligned}
\bar{S}_k^{AA}(\tau_j) &= \frac{1}{N_{\text{avg}}} \sum_{l=jN_{\text{avg}}}^{(j+1)N_{\text{avg}}-1} S_{kl}^{AA}, \\
\bar{S}_k^{BB}(\tau_j) &= \frac{1}{N_{\text{avg}}} \sum_{l=jN_{\text{avg}}}^{(j+1)N_{\text{avg}}-1} S_{kl}^{B}, \\
\bar{S}_k^{AB}(\tau_j) &= \frac{1}{N_{\text{avg}}} \sum_{l=jN_{\text{avg}}}^{(j+1)N_{\text{avg}}-1} S_{kl}^{AB}.
\end{aligned} \tag{1.21}$$

These time-averaged spectra represent the data integrated for the measurement time interval $t \in [\tau_j,\ \tau_j + T_{\text{frame}}]$, where

$$\tau_j = j\,T_{\text{frame}} = j\,\frac{N_{\text{avg}} L_{\text{FT}}}{f_s}, \quad j = 0, 1, \ldots, N_{\text{frame}}, \tag{1.22}$$

where $N_{\text{frame}} = \lfloor \frac{N_{\text{spec}}}{N_{\text{avg}}} - 1 \rfloor$. The spectra can be normalised as power spectral densities to give the spectral estimates in the conventional units of variance per unit of frequency:

$$\begin{aligned} \text{PSD1}(\tau_j) &= C_{\text{PSD}} \cdot \bar{S}_k^{AA}(\tau_j), \\ \text{PSD2}(\tau_j) &= C_{\text{PSD}} \cdot \bar{S}_k^{BB}(\tau_j), \\ \text{CSD}(\tau_j) &= C_{\text{PSD}} \cdot \bar{S}_k^{AB}(\tau_j), \end{aligned} \tag{1.23}$$

where $C_{\text{PSD}} = 2/(f_s L_{\text{FT}})$. We call the data $\{\text{PSD1}(\tau_j), \text{PSD2}(\tau_j), \text{CSD}(\tau_j)\}$ for a certain j a 'frame'. These frames are each written to file and thus collectively represent the full frequency-domain data of both interferometers with time resolution T_{avg} and frequency resolution Δf. This data has units of voltage (V^2/Hz) and calibration is needed to convert them to units of optical path length difference (m^2/Hz), which is the physical quantity measured with the interferometers. A cumulative average of each of these spectral densities is continuously accumulated over time:

$$\begin{aligned} \langle \text{PSD1} \rangle_{T=T_{\text{tot}}} &= \sum_{j=0}^{N_{\text{frame}}} \text{PSD1}(\tau_j), \\ \langle \text{PSD2} \rangle_{T=T_{\text{tot}}} &= \sum_{j=0}^{N_{\text{frame}}} \text{PSD2}(\tau_j), \\ \langle \text{CSD} \rangle_{T=T_{\text{tot}}} &= \sum_{j=0}^{N_{\text{frame}}} \text{CSD}(\tau_j). \end{aligned} \tag{1.24}$$

These cumulatively averaged spectra can then be used to look for stationary signals, such as the one predicted to be produced by quantum space-time fluctuations.

Implementation and programming

The processing algorithm above, up to and including the averaging of spectra, is performed on FPGAs programmed using the labVIEW FPGA module [42]. The LabVIEW FPGA module provides a graphical programming tool and a compiler for NI FPGA hardware. Using this module, a labVIEW FPGA programme can be compiled into files that are input to the Xilinx compilation tools. These compilation tools then produce an FPGA bitfile, which encodes the configuration of the logic gates of the FPGA to form the desired custom logical circuits. Note that this latter compilation process is not fully

deterministic; the allocation of the available logic gates on the FPGA is somewhat random; a random seed is used to select the starting point on the FPGA for allocating resources. This means that the compilation of programmes that require highly optimised configurations of the FPGA to be successfully implemented (e.g. those that require many sequential operations to be performed within a certain amount of time) often needs multiple attempts to be successful.

All operations performed on the data streams are implemented using labVIEW's so-called Single-Cycle Timed Loops (SCTL). This programming structure forces a set of operations to be completed once per FPGA clock cycle. An SCTL can therefore be implemented straightforwardly and efficiently on a set of connected logic gates driven by a single clock signal on the FPGA (known as a clock domain). The number of sequential operations that can be performed in an SCTL is necessarily subject to timing constraints; all sequential operations must complete within one clock cycle. The number of parallel operations that can be performed in one SCTL is limited by the number of resources on the FPGA. The processes of Fourier transforming (Eq. 1.16), cross-correlation (Eq. 1.19), and averaging (1.21) are each performed in a dedicated SCTL; the labVIEW code for these is shown in Fig. 1.7.

1.4.3 Testing using Simulated Signals

Methods

To test the performance of the HF-DAQ and identify spurious correlated noises inherent to the system, simulated signals were input to the digitisers and cross-correlation and averaging was performed on these signals for up to $T_{\text{int}} = T_{\text{tot}} = 10^6$ s.

Given continuous measurements of two independent realisations of random stationary noise, the magnitude of the cumulatively averaged cross-spectral density of these measurements scales down with the square root of the measurement time over the full bandwidth (see Eq. 1.1). In the presence of underlying cross-correlated noise, the average CSD will asymptotically converge to the power spectral density of this underlying cross-correlated noise. To test this scaling with integration time and identify cross-correlations between the two channels of the HF-DAQ, simulated uncorrelated white Gaussian noise signals were input to the two digitisers. These signals were produced using waveform generators, specifically two KeySight 33600A and two Liquid Instruments Moku:Pro, in various configurations. Cross-correlation measurements were also performed with nothing connected to the input to quantify the correlated ADC noise floor.

Results

Initial tests were done using a single KeySight 33600A waveform generator (WFG), set up to produce two independent realisations of Gaussian white noise over a bandwidth

of 80 MHz on its two output channels, which were then connected to the inputs of the two digitisers; the integration time for these measurements was $T_{\text{int}} = 10^5$ s. A second measurement was performed using two KeySight 33600A waveform generators powered from different wall sockets; each WFG was set up to produce Gaussian white noise over a bandwidth of 60 MHz and connected to a digitiser. The integration time for these measurements was $T_{\text{int}} = 10^6$ s. The variance of the simulated noise for both measurements was chosen to approximately match the expected power spectral density corresponding to the expected shot noise measured at the interferometers' photodiodes (see Sec. 1.5). The magnitudes of the cumulative average CSDs (Eq. 1.24) are plotted in Fig. 1.4.

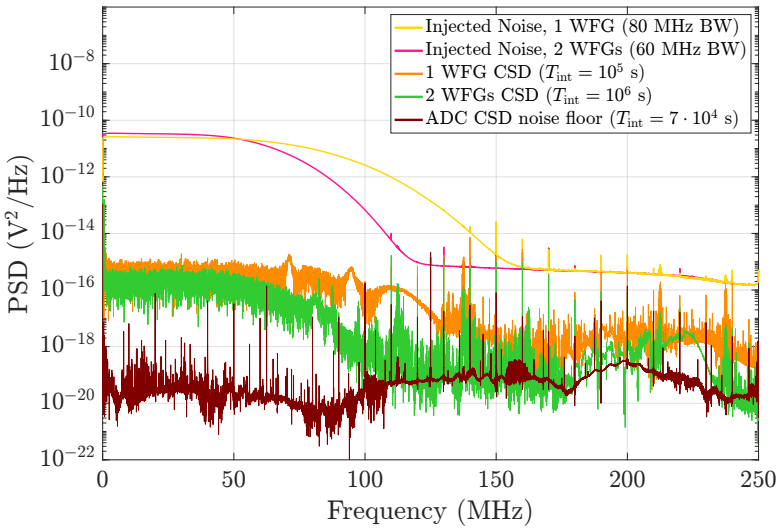

Figure 1.4. Power spectral densities of simulated signals produced by KeySight waveform generators cross-correlated and averaged using the HF-DAQ. The injected simulated noise auto-PSDs are shown together with the cumulative average CSDs.

A second set of measurements were performed using two Liquid Instruments Moku:Pro (Moku) devices configured as waveform generators producing independent noise with a power spectral density $\sim 10^{-12}$ V^2/Hz over a bandwidth of 250 MHz. Measurements were performed using two independent channels of one Moku, and using two separate Mokus (connected to a common power socket), respectively. The cumulative average CSDs for these measurements, using integration times of $T_{\text{int}} = 10^5$ and $T_{\text{int}} = 10^6$ s, respectively, are plotted in Fig. 1.5.

For all measurements described above, the median of the magnitude of the CSD, taken over the bandwidth of the injected noise, was computed for each data frame (Eq. 1.23). The time series of the medians of the CSDs thus obtained are plotted in

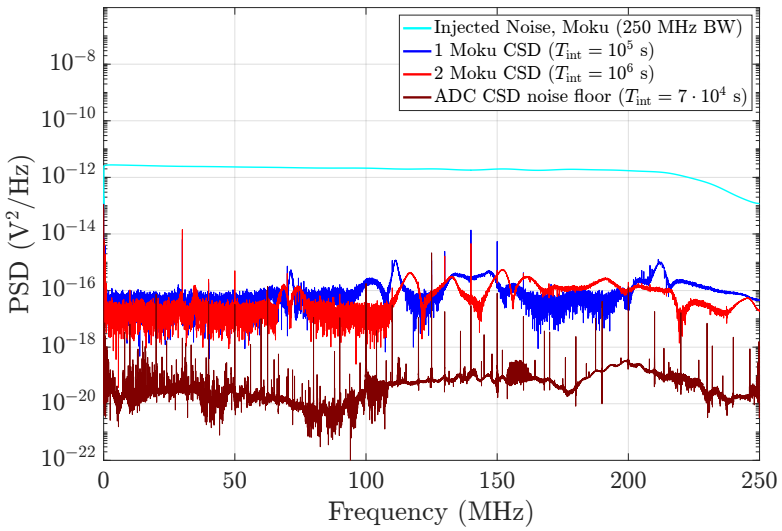

Figure 1.5. Power spectral densities of simulated signals produced by Moku:Pro waveform generators cross-correlated and averaged using the HF-DAQ. The injected simulated noise auto-PSDs are shown together with the cumulative average CSDs.

Fig. 1.6.

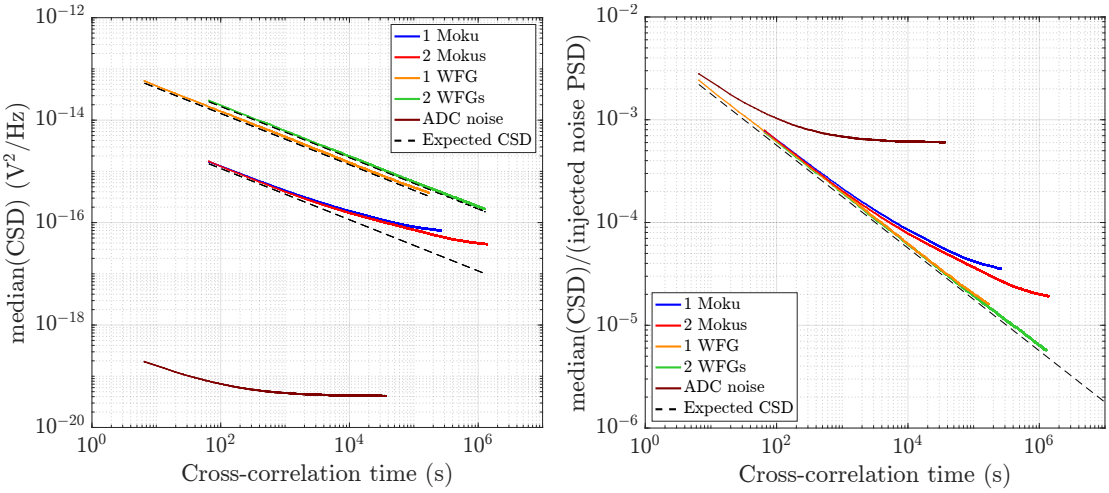

Figure 1.6. The median of the CSD of simulated noise signals cross-correlated and averaged by the HF-DAQ as a function of the cross-correlation time (T_{int}) is plotted. The plot on the right shows the median normalised to the injected noise auto-PSD.

Discussion & conclusion

A discrepancy between the observed scaling of the CSD with integration time and the theoretical scaling ($\propto 1/\sqrt{T_{\mathrm{tot}}}$) is evidence for the presence of correlations. Such discrepancies are present in all measurements at certain parts of the frequency band, and shows that spurious correlations are created at some point in the signal path that starts at the waveform generator and ends at the output of the digitisers' ADCs. If these correlations are created downstream from the waveform generators, they are likely to affect the final sensitivity of measurements with the QUEST experiment with integration times on the order 10^6 s or greater. It should be noted that spurious correlations of some magnitude will always be present due to unavoidable imperfections of the isolation between the two instruments and signal paths. The maximum integration time that can be achieved without encountering a cross-correlated noise floor is therefore always limited in any real measurement.

For the test with the Keysight waveform generators, the noise within the injection bandwidth scales down as would be expected in the absence of correlations (see Fig. 1.6), and reaches a level more than five orders of magnitude below the injected noise. It can be seen that correlations are present at frequencies above 50 MHz; the averaged CSDs show peaks between $\approx$ 70 and 90 MHz, which indicates underlying correlated noise (Fig. 1.4). In addition, it can be seen that the CSD for the measurement using two WFGs appears to converge to the underlying correlated ADC noise floor above 100 MHz, which suggests the correlations in this frequency range are created at the digitisers and are inherent to the HF-DAQ.

The measurements with the Moku:Pro waveform generators used injected noise with a smaller PSD than those with the Keysight waveform generators, which means underlying cross-correlated noise of a certain magnitude is resolved with shorter integration times. It can be seen that the cumulative average CSDs of these measurements do not have the same shape as the injected noise (Fig. 1.5); the spectra contain well-resolved features due to correlations, in particular above frequencies of 100 MHz. Correspondingly, the observed scaling of the median CSDs over time (Fig. 1.6) shows a discrepancy with the theoretical scaling for uncorrelated noise. The shape of the CSDs at frequencies above 100 MHz is different for the measurements using one and two Mokus, respectively. This suggests the correlations observed here depend on the configuration of the Mokus or the connections to the HF-DAQ and are created upstream of the digitisers.

In conclusion, the level of correlated noise inherent to the HF-DAQ at frequencies below 50 MHz was found to be smaller than $\sim 10^{-16}$ V^2/Hz. Given the expected shot noise PSD measured by the photodiodes, and assuming no correlations will be produced in the interferometers, the photodiodes, or the electronics between the photodiodes and the HF-DAQ, the QUEST experiment can reach a sensitivity at least five orders of

magnitude in power below the shot noise level through cross-correlation in this frequency range. At frequencies above 100 MHz, there are indications of correlated noise inherent to the HF-DAQ at a level of $\sim 10^{-19}$ V^2/Hz. These correlations might be produced through the electrical connection between the two digitisers established by the chassis that houses both, or could be due to crosstalk via another path. These correlations would limit the sensitivity of the QUEST experiment at frequencies above 100 MHz. However, the main signal of interest, that of quantum space-time fluctuations, is expected to be peaked at around $f = c/4L \approx 40$ MHz (for the current 1.8-m arm length, see Sec. 2.4).

Further cross-correlation measurements using more of the electronic components that will comprise the final signal paths of the QUEST experiment will be performed to search for correlated noises across the full bandwidth. In case it is found that correlated noise inherent to the HF-DAQ limits the sensitivity, the HF-DAQ could be reconfigured to electronically isolate the two digitisers by placing them in separate chassis, thereby reducing cross-talk. In this case, the data from one digitiser could be streamed via a fibre-optic connection to the other chassis that houses the coprocessor.

LabVIEW FPGA code

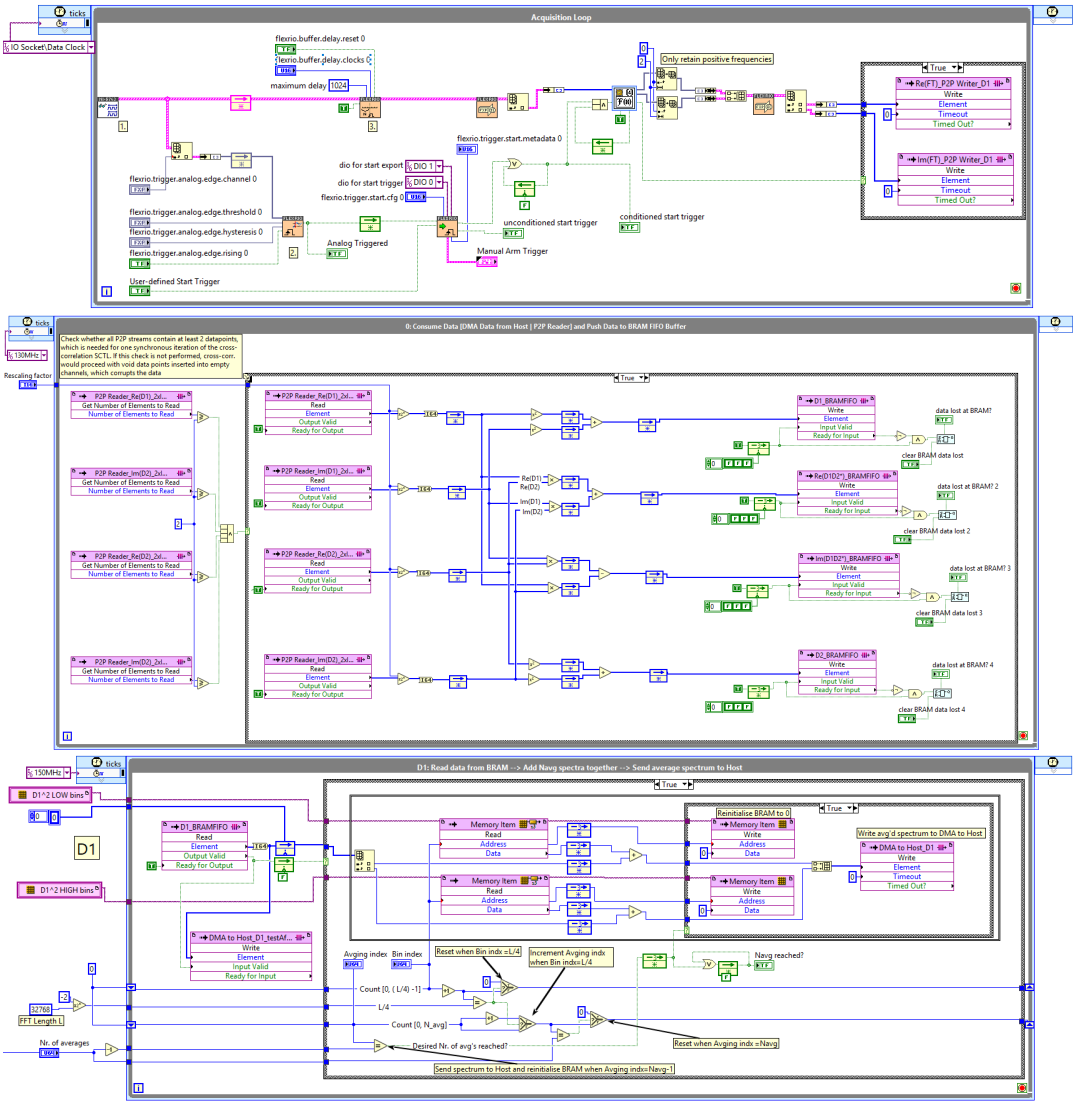

Figure 1.7. The labVIEW FPGA code implemented on the HF-DAQ of the QUEST experiment. The three main Single-Cycle Timed Loops (SCTL) that perform Fourier transformation, cross-correlation, and averaging, respectively, are shown. The top SCTL runs on the digitisers, and receives data from the back end of the ADCs. The data is subjected to an FFT and sent to the coprocessor over the PXI chassis backplane using a peer-to-peer stream. The middle SCTL receives spectral data from both digitisers and computes the real auto-power spectra and complex cross-spectra. The data is then sent to another clock domain on the coprocessor, where the bottom SCTL is executed. The bottom SCTL performs iterative summation of the incoming spectral data, and sends the cumulative sum to the server computer for post-processing every $(N_{\mathrm{avg}})^{\mathrm{th}}$ cycle.

1.5 Projected Sensitivity

The sensitivity of the QUEST experiment is designed to be limited by photon shot noise. All other sources of noise, except for thermal noise peaks from the optics, will be mitigated to below this shot noise floor as detailed in Sec. 1.3. Based on Eq. 1.7 and using the target circulating power $P_{\mathrm{BS}} = 10$ kW, the estimated shot-noise-limited displacement amplitude spectral density (or shot noise level, SNL for short) for a single interferometer is $5.17 \cdot 10^{-19}\,\mathrm{m}/\sqrt{\mathrm{Hz}}$ without squeezing. The estimated shot-noise-limited displacement noise amplitude spectral density is plotted in Fig. 1.8 for different levels of squeezing.

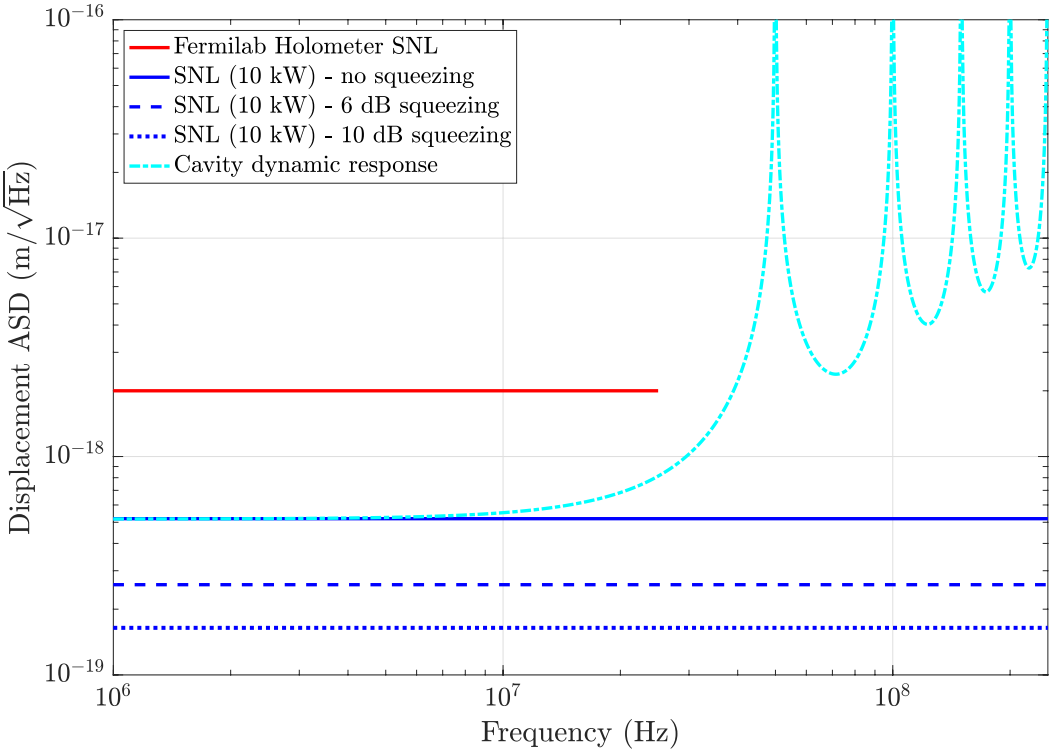

Figure 1.8. Comparision of the shot-noise-limited displacement noise amplitude spectral densities (SNL) of a single Fermilab Holometer interferometer and the projected SNL of a single QUEST interferometer using different levels of squeezing. Curves plotted are the reported final single interferometer SNL of the Fermilab Holometer (solid red line), projected single interferometer SNL for the QUEST experiment using 10 kW of circulating power with no squeezing (solid blue line), 6 dB of squeezing (dashed blue line), and 10 dB of squeezing (dotted blue line). In addition, the projected inverse sensitivity to harmonic arm length changes without squeezing is shown (dash-dotted cyan curve), assuming a interferometer arm length of 3 m (as was the original design).

In addition, a curve generated using FINESSE [43] is plotted in Fig. 1.8 that shows the inverse shot-noise-limited sensitivity to phenomena that harmonically modulate the length of the arms, as gravitational waves do. It can be seen that the sensitivity decreases at every multiple of the round-trip frequency $c/(2L)$, for an arm length $L = 3$ m (as in the original design). This is because the measured length change will be zero if an oscillatory signal changes phase by $k\pi$ ($k \in \mathbb{Z}$) within a single light-crossing time L/c.

2: Quantum Gravity

In this chapter, we discuss detecting quantum gravity phenomena with laser interferometers. It is argued that the description of gravity in concordance with quantum mechanics must include the existence of yet unobserved fluctuations in the measurements of distances. In theories that invoke the holographic principle, the magnitude of such quantum space-time fluctuations is predicted to be observably large. We review contemporary literature on holographic space-time fluctuations, and formulate a basic model to derive interferometric signals due to fluctuations of the space-time metric. We also discuss the prospects of detecting these quantum gravity phenomena with the QUEST experiment.

Contributions to published work in this chapter
Section 2.3 of this chapter is based on part of the article

- Vermeulen, S. M. *et al.* "An experiment for observing quantum gravity phenomena using twin table-top 3D interferometers". *Classical and Quantum Gravity* **38,** 085008. ISSN: 0264-9381, 1361-6382 (Apr. 2021).

S.M.V. lead the writing of that manuscript, and produced the majority of the content and text of the manuscript, with the exception of sections 5.1, 6, and a part of section 7 therein [1].

2.1 Introduction: The Pursuit of Quantum Gravity

2.1.1 The Need for Quantum Space-Time

The pursuit of physics is the accurate description of the dynamics of Nature. While arguably current physics already provides very accurate descriptions of matter, radiation, and their interactions for the majority of Natural systems, some systems cannot yet be described completely and consistently. While the scientific problem therein is only manifest for a limited number of observable systems (such as black holes), the theoretical problems of incompleteness and inconsistency are cause for dissatisfaction on their own and suggest a better description of Nature is to be pursued. The root cause of many of the problems in physics is the lack of understanding of the interplay of space-time described by general relativity and mass-energy described by quantum mechanics; a full understanding thereof would be the essence of a theory of Quantum Gravity.

The Einstein equations of general relativity describe how the curvature of the space-time manifold, which manifests as the phenomenon of gravity, depends on the distribution of mass-energy. The space-time manifold is a geometrical description of the conflation of space and time and defines the succession of causes and effects, the essence of propagation and dynamics. It is therefore apparent that any accurate and unequivocal description of dynamics requires a precise and unambiguous space-time manifold. It is exactly this requirement that proves problematic when one tries to compute dynamics using the Einstein equations while using a quantum mechanical description of the state of the mass-energy. In quantum mechanics, the mass-energy can exist in, for example, a superposition state of two individual states with well-defined mass-energy distributions. The superposition state however, does not have a well-defined distribution of mass-energy, and hence the space-time manifold is curved in an indeterminate way. No agreed upon or consistent way exists to account for such superposition states in the Einstein equations, and hence no unequivocal description of the dynamics can be made [44, 45].

Extensive efforts have been made to circumvent such issues by describing gravity not as the curvature *of* a space-time manifold but as a force that propagates *on* an uncurved space-time manifold. Following the successful description of other interactions as due to the exchange of force carriers that propagate on a flat space-time background, it was thought gravity could be described likewise. Such approaches however seem to disregard the fact that General Relativity is conceived as a logical consequence of the Equivalence Principle, and its inevitable implication that gravity is not a force that propagates causally, but is an alteration *of* causal propagation. It could therefore be argued

conversely that approaches to gravity that do not incorporate this aspect are destined to violate the Equivalence Principle, and therefore sure to fail. Examples of such approaches include effective field theory [46, 47], but also include the popular String Theory [48], which aims to describe gravity in direct conjunction with the other interactions. An example of a theory that does not require a background space-time is Loop Quantum Gravity, which furnishes its own description of space and time; however this version of space-time might not be consistent with General Relativity [49]. Scientifically, the problem of quantum gravity can not be considered solved until a consistent theory has been formulated and experimentally tested.

2.1.2 The search for Quantum Gravity Phenomena

It has long been believed that the problem of quantum gravity must be approached through mathematical reasoning towards a theoretical description. Many decades of such theoretical work has so far proven unsuccessful in formulating a consistent theory of quantum gravity. There is another option; the nature of quantum gravity could be gleaned empirically. To do this would require the observation of quantum gravity phenomena: physical effects that only exist for certain hypothetical combinations of quantum mechanics and gravity. Most of the proposed partial quantum-gravity theories, e.g. string theory and loop quantum gravity, state that such phenomena cannot yet be observed experimentally, as the effects are too slight (their magnitude would be on the Planck scale). However, semi-formal heuristic (i.e. without a complete underlying theory) arguments exist that predict the existence of quantum gravity phenomena of observable magnitude. Broadly speaking, the underlying consideration of these is that if gravity is geometrical, and if gravity is quantum mechanical, geometry must exhibit quantum mechanical properties, specifically quantum fluctuations.

A thought experiment

We consider here a thought experiment that illustrates such predictions. The origins of this thought experiment and the arguments that predict quantum gravity phenomena of observable magnitude go back to work by Wigner and Salecker [50, 51] in the 1950s, were also developed by Karolyhazy [52] in 1966, and by Ng and Van Dam [53] and Amelino-Camelia [54] in the 1990s (among others).

Consider the measurement of a distance L using the following method: a clock is placed at one end of L and a mirror is placed at the other; a photon is sent from the clock to the mirror and back. The time between emission and reception of the photon t is recorded with the clock, and using the known speed of light c, the distance can be inferred as $L = ct/2$. We now ask the question of how accurately this distance can possibly be measured. If we apply the laws of quantum mechanics to the experiment,

we find that the clock cannot be absolutely stationary; its momentum is uncertain by an amount Δp that is conjugate to the uncertainty of its position Δx:

$$\Delta x \Delta p \geq \hbar/2, \tag{2.1}$$

where $\hbar$ is the reduced Planck constant. Due to this uncertainty in the positions of the clock at the times of emission and reception, the measurement of the length L becomes uncertain by an amount

$$\delta L = \Delta x(t_0) + \Delta x(t) = \Delta x(t_0) + \frac{\Delta p t}{M} = \Delta x(t_0) + \frac{\hbar L}{\Delta x(t_0) M c}, \tag{2.2}$$

where M is the mass of the clock. If one minimises this uncertainty as a function of $\Delta x(t_0)$, the resulting minimal uncertainty of the length measurement that can be found is

$$\delta L_{QM} \geq \sqrt{\frac{\hbar L}{Mc}}, \tag{2.3}$$

which also corresponds to the Standard Quantum Limit encountered in laser interferometric measurements [30] (see also Sec. 1.3.1). It can be seen that this uncertainty can be made arbitrarily small by increasing the mass of the clock by an arbitrary amount.

So far, the argument has proceeded using the laws of quantum mechanics without considering gravity. However, we know that mass produces gravity and that this affects distances and the propagation of light. The heuristic combination of gravity and quantum mechanics in thought experiments like these can proceed in various ways and lead to different consequences. It seems reasonable to postulate that the uncertain position of the centre of mass of the clock in space is associated with an uncertainty in the gravitational field (the curvature of space-time), which in turn produces an uncertainty in the propagation of the photon. It might also be imagined that the clock is in a superposition of position eigenstates, and propose that the space-time would exist in a superposition state of two well-defined space-time manifolds (attempts to describe space-time as such have proven problematic [44]). Lastly, one could also consider the clock to exhibit quantum fluctuations of its mass-energy, and argue that this produces fluctuations of the space-time metric (note that the derivations of holographic quantum-space fluctuations Sec. 2.2 use a concrete consideration of an argument roughly analogous to this).

At the very least, General Relativity dictates that we cannot make the mass of the clock arbitrarily large; increasing the mass of the clock would perturb the space-time curvature and in the extreme case a black hole would be formed. It is thus argued for the present thought experiment, following [52, 53], that the uncertainty of the length

measurement cannot be smaller than the gravitational Schwarzschild radius r_s of the clock:

$$\delta L_{GR} > r_s = \frac{GM}{c^2}, \tag{2.4}$$

where G is the gravitational constant. This implies that it is required that

$$M < \frac{\delta L c^2}{G}. \tag{2.5}$$

If one combines this gravitational requirement with the uncertainty in length measurements due to the Standard Quantum Limit (Eq. 2.3), a fundamental uncertainty in the measurement of lengths from the combination of General Relativity and quantum mechanics is derived:

$$\delta L \geq (l_{\mathrm{P}})^{\frac{2}{3}} (L)^{\frac{1}{3}}, \tag{2.6}$$

where $l_{\mathrm{P}} = \sqrt{\hbar G/c^3}$. This result is notable for two reasons. First, the uncertainty is found to depend on the Planck length, but due to this constant being raised to the power 2/3, it is much greater than the 'conventional' estimates (e.g. those from string theory and loop quantum gravity) for the magnitude of the effects. Second, the uncertainty scales with the distance L that is measured. These two aspects could mean the measurement uncertainty is observably large.

The argument defined by Eq. 2.4 is not a rigorous one, as no consistent theory exists to describe the uncertainty in space-time given by uncertain mass-energy distributions. However, heuristic arguments that combine the basic concepts of gravity and quantum mechanics almost invariably find that there should be an irreducible variance of measurement of lengths that scales with the length measured. We refer to the underlying quantum-gravitational uncertainties that produce this variance as quantum space-time (QST) fluctuations. The different predictions for the magnitude of the root-mean-square uncertainty of the length measurement due to QST fluctuations can be expressed parameterically as [55]

$$\delta L \propto (l_{\mathrm{P}})^{\alpha} (L)^{1-\alpha}, \tag{2.7}$$

where α is a constant specific to each model of quantum gravity. Models that predict $\alpha = 1/2$ are often categorised as 'random walk models' [9, 56], and this value for α has been predicted more recently in theoretical work that invokes the holographic principle [8, 11]. Other, older theories predict $\alpha = 2/3$, and it has been argued that it is this value of α that is in concordance with the holographic principle [10, 52, 57]. Finally, conventional bottom-up approaches to quantum gravity such as string theory and loop

quantum gravity predict no accumulation of fluctuations over distance, which implies $\alpha = 1$ [58–60].

As the models with $\alpha = 1/2$ predict a length fluctuation of magnitude $\delta L \sim \sqrt{l_{\mathrm{P}} L}$, which might be observable with laser interferometers, and as these models based on the holographic principle have seen active development in recent years [8, 61–64], we focus on these theoretical predictions in this work.

2.2 Review of Holographic Quantum Space-Time Fluctuations

2.2.1 History

The proposal that fluctuations of space-time according to the holographic principle could be observed with interferometers, was first formulated in work by Ng and Van Dam [10]. However, the length fluctuations hypothesised there predicted a relatively small magnitude of the fluctuation of $\delta L \sim l_{\mathrm{P}}^{2/3} L^{1/3}$ (corresponding to $\alpha = 2/3$ in Eq. 2.7). Fluctuations of length measurements with a magnitude that scale with the square root of the measured length ($\alpha = 1/2$) as a consequence of the holographic principle were first proposed by Hogan [65]. Hogan made several attempts to formulate a theory to provide a mechanistic description of the quantum space-time (QST) fluctuations responsible for this phenomenology, but the proposed theories were not consistent with experimental constraints on Lorentz invariance and quantum mechanics [11, 17, 66]. This work nonetheless attracted significant interest when excess noise was observed in the GEO600 gravitational-wave detector, and it was speculated that this could be due to holographic quantum space-time fluctuations as proposed by Hogan. However, the noise was soon after found to have a different origin. Different and more precise phenomenological descriptions of holographic quantum space-time fluctuations have since been formulated by Hogan and Kwon [20, 67, 68].

More recently, in 2019, Verlinde and Zurek formulated an explicit mathematical model for holographic quantum vacuum space-time fluctuations, and showed this model produced the phenomenology given by Eq 2.7 for $\alpha = 1/2$. Further work by Verlinde, Zurek, Banks, and others, has developed this model in different theoretical frameworks [61–63, 69, 70].

2.2.2 The Holographic Principle

The holographic principle relates the geometry of space-time to the entropy it contains. Informally, it states that the amount of information that can be contained in volumes of space-time is limited by the area of an appropriate surface that is a boundary of the volume. Specifically, it states that, in d-dimensional space-time, given a $(d-2)$-dimensional spatial surface H with area A_H, the entropy S_C that can be contained in a $(d-1)$-dimensional hypersurface C bounded by H is limited:

$$S_C \leq \frac{A_H}{4G}, \tag{2.8}$$

where the hypersurface C is the causal development of H known as its light-sheet. This limit is known as the covariant entropy bound [71]. It is generally accepted that this bound is saturated in the case that H is the event horizon of a black hole [72].

The covariant entropy bound has profound implications for physics. The entropy is proportional to the number of degrees of freedom $N_{\text{d.o.f.}}$ in a physical system, i.e.

$$S \propto N_{\text{d.o.f.}}. \tag{2.9}$$

Conventional field theories state that the number of degrees of freedom is proportional to the volume of the system, as they are based on the postulate that a field comprises a harmonic oscillator at every point in space. The covariant entropy bound says this is false, as it states the entropy and therefore $N_{\text{d.o.f.}}$ is proportional not to the volume of a system but to the area of a surface that bounds this volume. This means field theories, if not wrong, at least overcount the number of degrees of freedom and give a description of Nature that contains unnecessary redundancies.

2.2.3 Heuristic Derivation of Holographic QST Fluctuations

Here we show in a hand-waving manner that the application of the covariant entropy bound to an interferometric measurement, supplemented with some additional assumptions, produces fluctuations of measured length $\delta L \propto \sqrt{l_{\text{P}} L}$. While this derivation is not rigorous, it captures the underlying reasoning of recent formal theoretical work, e.g. by Verlinde and Zurek [8, 61, 63].

We start by considering an interferometric measurement in Minkowski space-time using an interferometer with arms of length L (see Fig. 2.1). Input light is split at a beamsplitter, which starts the measurement. The light propagates in the interometer arms along null geodesics. After reflection off the arms' end mirrors, the light returns along null geodesics and is recombined at the beamsplitter where it interferes, completing the measurement. The intersection (or overlap) of the future light cone of the start of the measurement and the past light cone of the end of the measurement uniquely define a causally connected space-time volume known as a causal diamond (C). The boundary of the causal diamond is a causal horizon that can be described as a Rindler horizon or a conformal Killing horizon.

At any fixed time during the measurement (i.e. on any Cauchy surface), the outside boundary of the causal diamond is a two-dimensional space-like sphere. In the past half of the causal diamond, this surface grows at the speed of light as time progresses, reaching a radius of L, before shrinking back to a point in the future half of the causal diamond. This growth and shrinking of the space-like surface is thus the causal development of the boundary surface; i.e. it is the light sheet of the spherical surface with radius L.

This identification allows us to apply the covariant entropy bound to the interferometric measurement.

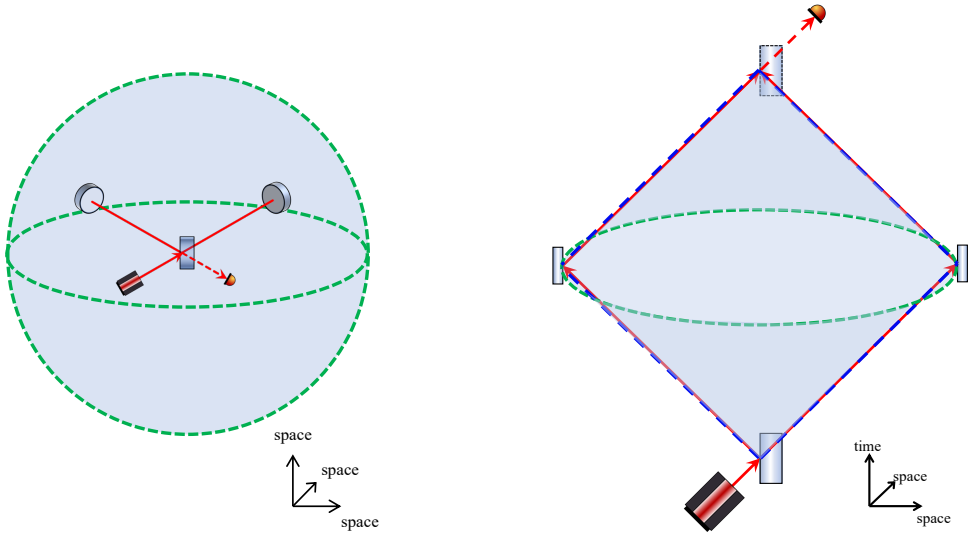

Figure 2.1. left: A diagram of an interferometer in three spatial dimensions. Light (red lines) from a laser is injected to the beamsplitter where it is split into two arms that are terminated by mirrors that return the light to the beamsplitter, where the light from the two arms is recombined. The interference of the light is measured at the output port of the interferometer using a photodetector. The green dashed sphere has a radius equal to the arm length of the interferometers, and is the space-like holographic boundary of the interferometric measurement. In applications of the holographic principle the area of this sphere bounds the entropy of the measurement. **right:** Space-time diagram of an interferometric measurement. The splitting of light at the start of the measurement and the recombination at the end of the measurement are events that uniquely define a causal diamond (blue shaded area). The light-sheet or causal development of the boundary of the causal diamond, also identifiable as a Rindler horizon or conformal Killing horizon, is shown by blue dashed lines. The holographic space-like boundary of the causal diamond is represented by the green dashed circle, which corresponds to the green dashed sphere shown on the left.

We assume that the covariant entropy bound is saturated for the causal diamond C, and that the entropy of the causal diamond is thus given by the area of a two-dimensional sphere of radius L:

$$S_C = \frac{A_H}{4G} = \frac{8\pi L^2}{(l_{\mathrm{P}})^2}. \tag{2.10}$$

This implies that the number of degrees of freedom that describe physics inside the causal diamond are limited, and scale with the surface area of the horizon in concordance

with the holographic principle:

$$N_{\text{d.o.f.}} \propto S_C \propto \frac{L^2}{(l_{\text{P}})^2}. \tag{2.11}$$

We further assume that these degrees of freedom are quantum mechanical, and exhibit quantum fluctuations of the total energy carried by these degrees of freedom E. We also assume the fluctuations obey Poisson statistics; i.e. we assume the magnitude of the fluctuation δE is proportional to the square root of the number of degrees of freedom. This gives

$$\frac{\delta E}{E} \propto \frac{\sqrt{N_{\text{d.o.f.}}}}{N_{\text{d.o.f.}}}. \tag{2.12}$$

Finally, we consider the scaling of the magnitude of strain fluctuations ($\delta L/L$) of the metric of the causal diamond produced by energy fluctuations according to General Relativity, which gives

$$\left(\frac{\delta L}{L}\right)^2 \propto \frac{\delta E}{E}, \tag{2.13}$$

(cf. the strain produced by a gravitational wave that carries energy E)[73]. Combining the three equations above, we find

$$\delta L \propto \sqrt{l_{\text{P}} L}. \tag{2.14}$$

2.2.4 Models of Holographic QST Fluctuations by Verlinde & Zurek et al.

Verlinde & Zurek et al. have used various approaches to describe holographic quantum space-time fluctuations in different theoretical settings. These arguments generally start from the assumption that the covariant entropy bound (Eq. 2.10) gives the number of quantum mechanical degrees of freedom in the causal diamond defined by an interferometric measurement, and it is assumed that these degrees of freedom fluctuate. The magnitude of the energy fluctuations of these degrees of freedom are also conjectured to be given by the entropy bound, and their hypothetical gravitational effect on an interferometric measurement is then computed using different methods. Below, we summarise their work describing quantum vacuum fluctuations of holographic degrees of freedom and their effect on interferometric measurements in flat space-time [8, 61, 63].

Modular Hamiltonian fluctuations

Verlinde and Zurek mainly consider energy fluctuations described in terms of the modular Hamiltonian K, which is defined via the density matrix that describes the quantum

state of the inside of the causal diamond

$$\rho = \frac{e^{-K}}{Z} \quad \text{with} \quad Z = \operatorname{tr}\left(e^{-K}\right). \tag{2.15}$$

One can in general associate an entropy $S_{\text{ent}} = -\operatorname{tr}(\rho \log \rho)$ [74] to this density matrix, and if this entropy is given by the area of the boundary of the causal diamond, saturating the covariant entropy bound, i.e.

$$S_{\text{ent}} = S = \frac{A_H}{4G}, \tag{2.16}$$

it is found that the fluctuations of the modular Hamiltonian $\Delta K = K - \langle K \rangle$ obey [62]

$$\langle \Delta K^2 \rangle = \frac{A_H}{4G}. \tag{2.17}$$

'Pixellon' fluctuations

More recently, Zurek has proposed a more explicit model of the holographic degrees of freedom, where the quantum mechanical excitations of the degrees of freedom are called 'pixellons'. It is proposed that their vacuum state is described by a thermal density matrix:

$$\rho_{\text{pix}} = \frac{1}{\mathcal{Z}} \exp\left[-\beta \int \frac{d^3\mathbf{p}}{(2\pi)^3} \left(\epsilon_{\mathbf{p}} - \mu\right) a^\dagger_{\mathbf{p}} a_{\mathbf{p}}\right], \tag{2.18}$$

with partition function

$$\mathcal{Z} = \prod_{\mathbf{p}} \frac{1}{1 - e^{-\beta(\epsilon_{\mathbf{p}} - \mu)}} \tag{2.19}$$

where $\epsilon_{\mathbf{p}}$ is the energy of pixellons with momentum p, μ is the chemical potential, $a^\dagger_{\mathbf{p}}, a_{\mathbf{p}}$ are the creation and annihilation operators of the pixellons, and $\beta = 1/T$ is the inverse temperature of the system. The occupation number of the pixellon states is assumed to be (see [63])

$$\sigma_{\text{pix}}(\mathbf{p}) = \frac{1}{e^{\beta\omega(\mathbf{p})} - 1} = \frac{a}{l_p \omega(\mathbf{p})}, \tag{2.20}$$

where $\omega(\mathbf{p}) = (\epsilon_{\mathbf{p}} - \mu)$. Thermodynamic energy fluctuations of the pixellons are then calculated from this model.

Gravitational effect on interferometric measurements

The quantum mechanical energy fluctuations above are assumed to produce a gravitational effect that affects the propagation of light in an interferometer. One approach considered the energy fluctuations to produce a series of gravitational shockwaves that affect the light as it propagates [62]. In another article [61] Zurek et al. compute the gravitational effect of the quantum fluctuations on the interferometric measurement using the Feynman-Vernon influence functional, which allows one to compute the influence of one quantum system (the holographic quantum degrees of freedom) on another (the mirror of the interferometer). A more recent approach computes the time delay of light in the arms due to holographic quantum fluctuations directly via the metric [63].

2.2.5 Angular Correlations of Holographic QST Fluctuations

It has been proposed that holographic quantum space-time fluctuations exhibit a certain pattern of correlations. In particular, in space-time regions bounded by horizons (e.g. causal diamonds), the fluctuations are thought to be correlated at points separated in directions transverse to the light sheet, or equivalently directions tangent to the space-like horizon. For a causal diamond defined by an interferometric measurement, the correlations in length fluctuations are thus described with a non-zero angular two-point correlation function

$$g(\boldsymbol{\gamma}) = \langle \delta L(\boldsymbol{\vartheta}) \delta L(\boldsymbol{\vartheta} + \boldsymbol{\gamma}) \rangle, \tag{2.21}$$

where $\boldsymbol{\gamma}$ is the angular separation of two points on the spherical boundary of a causal diamond and $\boldsymbol{\vartheta} = (\theta, \phi)$ represents the angular coordinates in a spherical coordinate system centred on the beamsplitter. For an interferometric measurement, a non-constant two-point function implies that the signal depends on the angle between the interferometer's arms $\gamma = |\boldsymbol{\gamma}|$.

Verlinde & Zurek propose that the boundary of the causal diamond responds gravitationally to the holographic quantum fluctuations according to a Green's function of a modified Laplacian on a two-dimensional sphere [8]. This function can be expanded into the spherical harmonics $Y_{l,m}(\boldsymbol{\vartheta})$ which gives

$$g(\boldsymbol{\gamma}) = \langle \delta L(\boldsymbol{\vartheta}) \delta L(\boldsymbol{\vartheta} + \boldsymbol{\gamma}) \rangle = \frac{l_{\mathrm{P}} L}{(4\pi)^2} \sum_{l,m} \frac{Y_{l,m}(\boldsymbol{\vartheta}) Y_{l,m}(\boldsymbol{\vartheta} + \boldsymbol{\gamma})}{l^2 + l + 1} \tag{2.22}$$

Before this relation was published in work by Verlinde & Zurek, 't Hooft proposed that black holes can obey unitarity if the quantum fluctuations at the horizon (e.g. Hawking radiation) are antipodally entangled [22]. This work by 't Hooft finds almost identical predictions for the angular two-point correlation function of the fluctuations [8, 75, 76].

The decomposition of the correlations into spherical harmonics $Y_{l,m}$ above has most of its power in low l modes, which motivates the prediction that the transverse correlations extend over macroscopic angular separations. Importantly, macroscopic transverse correlations imply that fluctuations are coherent over the typical diameter of a laser beam or telescope aperture. If this is the case, astrophysical constraints set on quantum space-time fluctuations by evaluating the blurring or degrading of images of distant objects [56, 77, 78] might not apply (see Sec. 2.2.8).

Moreover, it has been suggested that the angular power spectrum of the temperature fluctuations in the CMB can also be described by the angular two-point correlation function of holographic QST fluctuations on an inflationary horizon [79, 80].

2.2.6 Models of Holographic QST Fluctuations by Hogan & Kwon

Hogan and Kwon have proposed several phenomenological descriptions of holographic QST fluctuations, that all predict length fluctuations $\delta L \propto \sqrt{l_{\mathrm{P}} L}$. Mechanistic theoretical descriptions of the fluctuations by Hogan violated Lorentz invariance and were since abandoned [17]. Statistical models of the fluctuations were formulated, which yielded the first frequency-domain descriptions of signals from holographic QST fluctuations in interferometers [20, 67, 68].

After the Fermilab Holometer failed to detect a signal from holographic QST fluctuations (see Sec. 2.2.8), Hogan & Kwon hypothesised additional phenomenological aspects of the fluctuations [19]. Specifically, this work posits that holographic QST fluctuations may affect lengths in directions transverse to light-sheets, or equivalently in directions tangent to the space-like boundary of the causal diamond. Such 'rotational' fluctuations would not be observable when measuring lengths along radial directions as is done with interferometer arms that only extend radially from the beamsplitter (the radial direction is defined here by the spherical symmetry of the causal diamond defined by the measurement). Moreover, it was proposed that radial QST fluctuations might not be observable [64].

These theories motivate the consideration of interferometer designs with radial and non-radial arm segments (see Sec. 2.3 and Fig. 2.3).

2.2.7 Strain PSDs from Holographic QST Fluctuations

Verlinde & Zurek et al. and Hogan & Kwon have recently computed the strain power-spectral density (PSD) that holographic QST fluctuations would produce in interferometer signals using their respective models [63, 64]. In both cases, it is predicted that the majority of the spectral power of the signal exists at frequencies on the order of the light-crossing frequency c/L. Both also predict a peak strain amplitude spectral density on the order of 10^{-23} $\mathrm{Hz}^{-1/2}$. The predicted spectra are shown in Fig. 2.2.

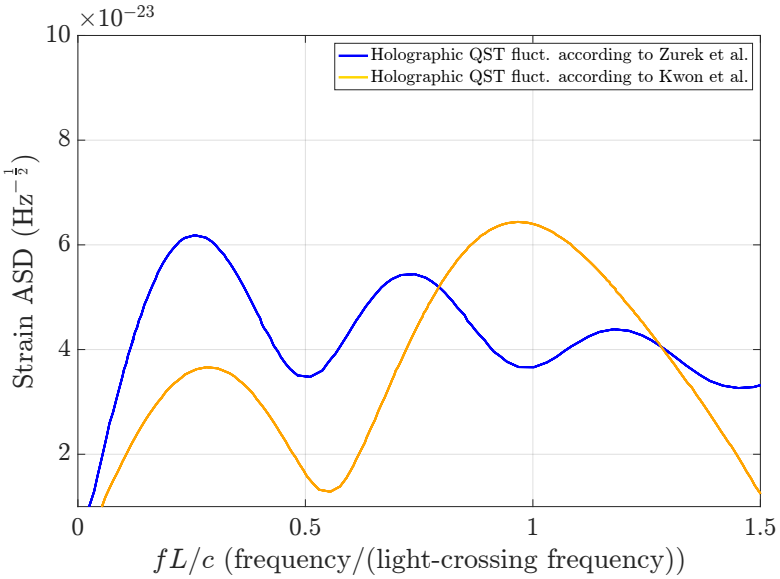

Figure 2.2. Theoretical predictions for the strain amplitude spectral densities due to holographic quantum space-time fluctuations as measured with an interferometer are shown. These signal spectra for the models by Zurek et al. and Kwon et al. are taken from [63], and [64], respectively. The frequency axis is normalised to the light-crossing frequency of the interferometer.

2.2.8 Experimental Constraints on QST Fluctuations

There is no experimental evidence for the existence of holographic QST fluctuations, but using interferometric and astronomical observations, some tentative constraints on the phenomenology can be set.

Constraints from astronomical observations

Given the general phenomenology of length fluctuations that scale with distance as described by Eq. 2.7, it has been argued that images of distant astronomical objects should appear blurred as the phase front of the light is distorted by the QST fluctuations. By analysing astronomical data from a variety of telescopes operating at different wavelengths, constraints were set on the parameter $\alpha < 0.72$, subject to important caveats [56, 77, 78]. Moreover, if the angular correlations of the fluctuations are macroscopic as implied by Eq. 2.22, no distortion of the phase front of light from distant sources is expected and the constraints do not apply.

Constraints from gravitational-wave detectors

If the QST fluctuations are transversely correlated over distances on the order of the diameter of typical laser beams, the resulting length fluctuations could be observable in interferometers, as they compare the phase fronts of two light beams that are separated by a large angle. Specifically, if the angular correlation length of the fluctuations is greater than the beam diameter (i.e. the width of the phase front) but smaller than the angular separation between the arms, the wavefronts in either arm are coherently perturbed, and the two arms undergo different perturbations. In this case, the perturbed light from the two arms interferes constructively at the output port of the beamsplitter and a signal is produced.

The gravitational-wave detectors used by the LIGO-Virgo-KAGRA collaboration [81] are currently the most sensitive interferometers in terms of strain sensitivity. To estimate their sensitivity to QST fluctuations, the expected signal power in the sensitive frequency range of these interferometers must be considered. Gravitational-wave detectors have in general a reduced sensitivity at higher frequencies due to the frequency response of optical cavities included in the interferometer design [82]. In addition, the output signals of the interferometers are currently sampled at frequencies less than twice the light-crossing frequency $2c/L$, and therefore signals on the order of $2c/L$ cannot be resolved. However, although the spectrum of the signal from holographic QST fluctuations is strongly suppressed at frequencies below $f \sim c/L$ (the signal PSD scales as $\propto f^2$ or even $\propto f^4$ at low frequencies), some constraints may still be set, as shown in [63].

It should be noted that it has not been conclusively established how the signal from holographic QST fluctuations as measured in an interferometer is affected by the inclusion of Fabry–Pérot cavities in the arms. It has been argued that the cavities reduce the signal [8, 83] by a factor on the order of the cavity's Finesse ($\sim 10^2$ for the arm cavities in gravitational-wave detectors), but more recently the opposite has been claimed [63]. Work is ongoing [84] on a model that describes the effect of QST fluctuations on propagating light that incorporates a more complete description of the optical states, which may resolve the conundrum.

Constraints from the Fermilab Holometer

The Fermilab Holometer consists of a pair of 40-m laser interferometers specifically designed to detect holographic QST fluctuations (see Sec. 1.1.2). Contrary to gravitational-wave interferometers, the Holometer's arms did not include optical cavities and the instrument was designed to be sensitive at the light-crossing frequency and above. Constraints were set on the magnitude of QST fluctuations parallel to the light sheet [18], as in the models by Verlinde & Zurek and the earlier models by Hogan, and fluctuations transverse to the light sheet [21], as in the later models by Hogan & Kwon (see also

Fig. 2.6). The reported constraints from the Fermilab Holometer are contingent on the assumption that the length fluctuations are fully correlated between the two instruments (which are separated by 0.9 m).

2.3 Basic Model of Quantum Space-Time Fluctuations in an Interferometer

In this section, a basic model of the coupling between quantum space-time fluctuations and laser interferometers is formulated and then used to derive a frequency-domain signal of the quantum space-time fluctuations in a 3D interferometer. We note that when this model was developed, much of the literature discussed in the previous section and in particular the concrete and precise frequency-domain signals discussed in Sec. 2.2.7 were not yet published.

2.3.1 Model of Fluctuations of Measured Length

Consider an interferometer as in Fig. 2.3 where the two arms X and Y, intersecting at the beamsplitter BS, are at an angle γ with respect to each other. The inner, radial, section of both arms has a length L_{I}. Mirrors $\mathrm{MM}_{\mathrm{X,Y}}$ are placed at the end of the first section to reflect the beams of either arm at an angle β into an outer, non-radial arm section with length L_{O}. The light in both arms is returned along the same path by end mirrors $\mathrm{EM}_{\mathrm{X,Y}}$.

To model the signal due to quantum space-time fluctuations that might be detected in such an experiment, it is assumed the experiment is done in flat (Minkowski) space-time η_{ij}, where quantum geometrical fluctuations manifest as small perturbations h_{ij} of the metric;

$$g_{ij} = \eta_{ij} + h_{ij}, \tag{2.23}$$

where roman indices denote spatial components. We choose a gauge in which the metric perturbations are purely spatial, and therefore only consider the spatial part of the metric.

Let a photon traverse an arm from beamsplitter to end mirror once. The arm length that is measured at a time t by comparing the phase of such a photon to a stable reference is given by the proper distance between beamsplitter and end mirror [8, 85, 86]:

$$L(t) = \int_0^t \sqrt{g_{ij}\,\lambda^{i\prime}\lambda^{j\prime}}\,ds, \tag{2.24}$$

where $g_{ij}(s)$ is the metric, $\lambda^i(s)$ is a parameterisation of the photon's path, and $\lambda^{i\prime}(s) = \frac{d\lambda^i}{ds}$ is the tangent vector, repeated indices are to be summed over, and $L(t)$ is the measured length of the arm at any time. Natural units are used unless specified otherwise.

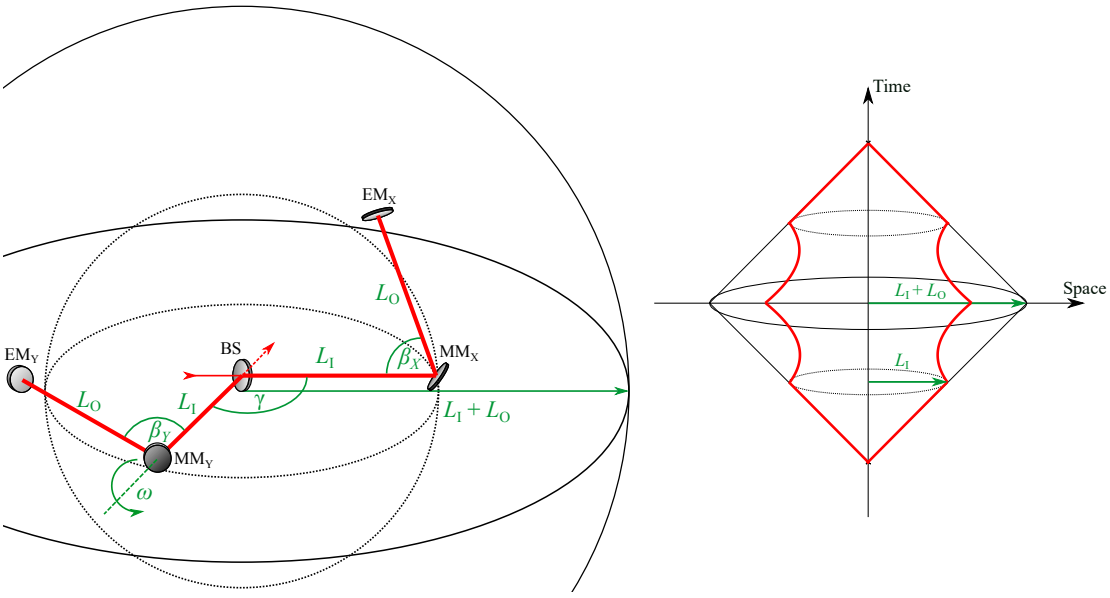

Figure 2.3. left: Schematic of the interferometer geometry in three spatial dimensions. The two arms A and B (red) consist of a radial and non-radial segment with lengths L_I and L_O respectively. The angle between the two arms at the beamsplitter BS is γ, and the angles between the two segments in either arm are β_X and β_Y respectively. ω is the angle between the two planes that contain each interferometer arm as measured when $\gamma = 0$. θ and ϕ are the polar and azimuthal angle, where the $\theta = 0$ plane is the plane defined by the two radial segments, and the $\phi = 0$ is the plane orthogonal to the $\theta = 0$ plane that contains the non-radial segment of arm X. The outer solid sphere with radius $L = L_I + L_O$ is a two-dimensional space-like boundary of a (3+1)-dimensional causal diamond defined by the experiment. **right:** Space-time diagram of two photons traversing both interferometer arms from beamsplitter to end mirror and back. The photon paths are projected onto the radial spatial direction, and the two transverse spatial directions are suppressed. The top and bottom vertices of the solid square correspond to the photons leaving and returning to the beamsplitter and define a causal diamond. The boundary of this causal diamond is the space-like circle around the origin, which represents the same surface as the solid sphere in the diagram on the left.

Using Eq. 2.23 in a Taylor expansion of Eq. 2.24, the measured length change due to quantum space-time fluctuations to first order can be written as [73]

$$\delta L(t) = \frac{1}{2}\int_0^t h_{ij}\,\lambda^{i\prime}\lambda^{j\prime}\,ds. \tag{2.25}$$

Note that this expression entails an integral of the fluctuations over a trajectory in the space-time volume of a causal diamond. In a full holographic theory, an integral of such a geodesic would require bulk reconstruction [69, 87]. Eq. 2.25 is to be seen as a

simplified model of how a length change due to quantum space-time fluctuations might arise.

2.3.2 Model of Statistics of Fluctuations

To be able to model the frequency domain signal that would be obtained if the phase of many photons successively traversing the arm once is measured, some assumptions about the statistics of the fluctuations $h_{ij}(s)$ need to be made. In the case that the fluctuations behave like homogeneous and isotropic white noise with a variance on the order of the Planck length, i.e. [8]

$$\langle h_{ij}(s_1)h_{kl}(s_2-\tau)\rangle = A^2 l_{\mathrm{P}}\delta(s_1-s_2+\tau)\delta_{ik}\delta_{jl}, \tag{2.26}$$

the two-time correlation function of length measurements of any photon path is:

$$\langle \delta L(t_1)\delta L(t_2)\rangle = \frac{1}{4}\left\langle \int_0^{t_1}\int_\tau^{t_2} h_{ij}\,\lambda^{i\prime}\lambda^{j\prime}h_{kl}\,\lambda^{k\prime}\lambda^{l\prime}\,ds_1\,ds_2\right\rangle = A^2 l_{\mathrm{P}} L\Lambda(\tau), \tag{2.27}$$

where angular brackets denote expectation values, A is some constant of order one, $\tau = t_2 - t_1$, and $\Lambda(\tau)$ is a triangle function defined as [20]

$$\Lambda(\tau) = \begin{cases} 1-|\tau|/L & 0<\tau<L \\ 0 & \text{otherwise.}\end{cases} \tag{2.28}$$

Eq. 2.27 does not allow all the phenomenologies of fluctuations of measured distance proposed in theory to be modelled. Specifically, it can be seen that the case that the space-time fluctuations behave like uncorrelated white noise with Planckian variance as in Eq. 2.26 leads to a scaling of length fluctuations as in Eq. 2.7 with $\alpha = 1/2$.

To reproduce all the different phenomenological predictions parmeterised by α for the scaling of measured length changes summarised in Eq. 2.7, to account for homogeneous but anisotropic quantum space-time fluctuations [67], and to allow the modelling of different arm geometries, it might be assumed that in general

$$\langle \delta L(t_1)\delta L(t_2)\rangle = \frac{1}{4}\left\langle \int_0^{t_1}\int_\tau^{t_2} h_{ij}\lambda^{i\prime}\lambda^{j\prime}\,h_{kl}\lambda^{k\prime}\lambda^{l\prime}\,ds_1 ds_2\right\rangle \tag{2.29}$$

$$= \left(\langle\lambda^{m\prime}\lambda^{n\prime}\rangle A_{mn}\right)^2 (l_{\mathrm{P}})^{2\alpha}(L)^{2(1-\alpha)}\Lambda(\tau), \tag{2.30}$$

where $A_{mn} \equiv \langle |h_{mn}|\rangle$. The expectation value of the magnitude of the length fluctuations,

$$\langle|\delta L(t)|\rangle \approx \sqrt{\langle \delta L(t)\delta L(t)\rangle}, \tag{2.31}$$

thus scales according to the phenomenological predictions in Eq. 2.7 as desired:

$$\langle\, |\delta L(t)|\, \rangle = \frac{1}{2}\left\langle \left| \int_0^t h_{ij}\, \lambda^{i\prime}\lambda^{j\prime}\, ds \right| \right\rangle \approx \langle \lambda^{i\prime}\lambda^{j\prime}\rangle A_{ij} (l_{\rm P})^{\alpha} (L)^{1-\alpha}. \tag{2.32}$$

Setting $\alpha = 1/2$ and $A_{ij} = A\delta_{ij}$ in this expression corresponds to the case of homogeneous isotropic white noise. Eq. 2.30 represents a generalisation of the phenomenology of the quantum space-time fluctuations. Note that for $\alpha \neq 1/2$, Eq. 2.30 implicitly assumes a two-point correlation function for quantum space-time fluctuations different from Eq. 2.26.

2.3.3 Geometrical Coupling Factors of 3D Interferometer Arms

The sensitivity to non-radial quantum space-time fluctuations depends on the geometry of the arms. Therefore, to inform the geometrical design of the interferometers, it is worthwhile to asses this dependency quantitatively. Eq. 2.32 can be evaluated for an interferometer arm geometry as in Fig. 2.3 in a spherical basis ($i \in \{r, \theta, \phi\}$):

$$\langle\, |\delta L(t)|\, \rangle = \frac{1}{2}\left\langle \int_0^{t_{\rm I}} \lambda'_{r_{\rm I}} h_{rr}\, ds_{\rm I} + \int_0^{t_{\rm O}} h_{ij}\, \lambda^{i\prime}_{\rm O}\lambda^{j\prime}_{\rm O}\, ds_{\rm O} \right\rangle \tag{2.33}$$

$$= A_{rr} (l_{\rm P})^{\alpha} (L_{\rm I})^{1-\alpha} + \langle \lambda^{i\prime}_{\rm O}\lambda^{j\prime}_{\rm O}\rangle A_{ij} (l_{\rm P})^{\alpha} (L_{\rm O})^{1-\alpha}, \tag{2.34}$$

where the subscripts I, O refer to the inner and outer arm segments, such that $L_{I,O}$ are the expectation values of the lengths of the inner and outer arm segment, respectively, and $t = t_I + t_O$. It can be seen from this expression that the inner arm segment is only sensitive to radial fluctuations (h_{rr}), which are those along light-sheets (transverse to boundaries of causal diamonds). The outer arm segment is in general sensitive to fluctuations in any direction, including those transverse to light-sheets ($h_{\theta\theta}$ and $h_{\phi\phi}$, along boundaries of causal diamonds). Specifically, the response of the outer arm segment to quantum space-time fluctuations depends on the geometrical coupling factors

$$G^{ij}_{\rm O}(\beta_{X,Y}, R) = \langle \lambda^{i\prime}_{\rm O}\lambda^{j\prime}_{\rm O}\rangle (L_{\rm O})^{1-\alpha}, \tag{2.35}$$

where $R = L_I/L_O$. To evaluate this expression, we consider a parameterisation of the photon path in the arms:

$$\lambda^i = \lambda^i_I + \lambda^i_O = r(s)\hat{r}^i + \theta(s)\hat{\theta}^i + \phi(s)\hat{\phi}^i \tag{2.36}$$

For both arms X and Y the inner radial segment can be trivially parameterised as

$$\lambda^i_I = s\hat{r}^i. \tag{2.37}$$

For the outer, non-radial segment,

$$\lambda^i_O = r_O(s)\hat{r}^i + \theta_O(s)\hat{\theta}^i + \phi_O(s)\hat{\phi}^i. \tag{2.38}$$

For arm X,

$$r^X_O(s) = \sqrt{s^2 + L_O^2 - 2sL_O\cos\beta_X}, \tag{2.39}$$

$$\theta^X_O(s) = \arcsin\left[\frac{s\sin(\beta_X)}{\sqrt{s^2 + L_O^2 - 2sL_O\cos\beta_X}}\right], \tag{2.40}$$

$$\phi^X_O(s) = 0. \tag{2.41}$$

For arm Y, the parameterisation can be obtained by performing a rotation on the parmaterisation of the X-arm by an angle ω (see Fig. 2.3).

Using this parameterisation, and taking for the expectation value of $\lambda^{i\prime}\lambda^{j\prime}$ the mean tangent vector over the photon path

$$\langle\lambda^{i\prime}\lambda'^{j}\rangle \equiv \overline{\lambda^{i\prime}\lambda'^{j}} = \frac{1}{t}\int_0^t \lambda^{i\prime}\lambda^{j\prime}ds, \tag{2.42}$$

the geometrical coupling factors $G^{rr}_{\rm O}$ and $G^{\theta\theta}_{\rm O}$ were evaluated numerically as functions of $\beta_{X,Y}$ and $R = L_I/L_O$, and the results are plotted in Figs. 2.4. This shows that the

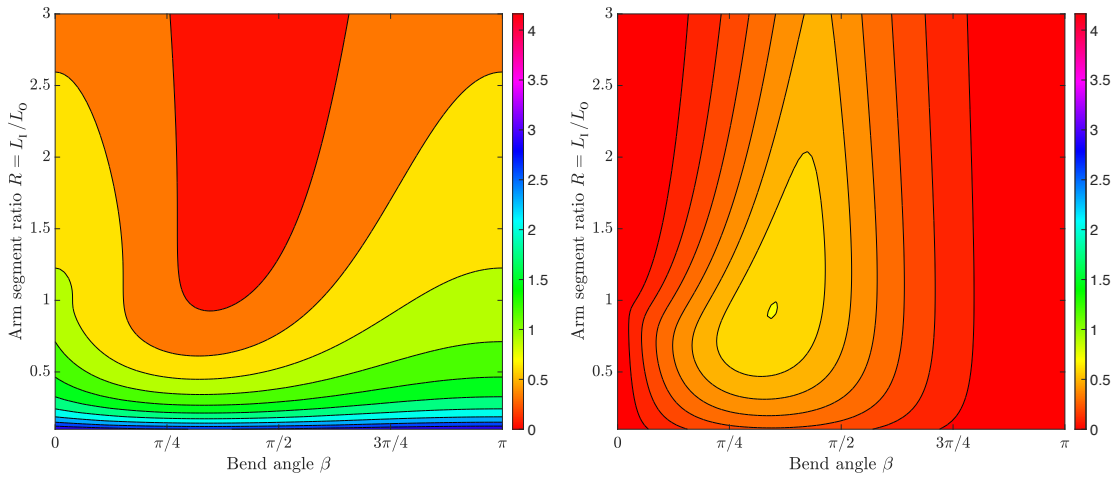

Figure 2.4. Geometrical coupling factors $G^{rr}_{\rm O}$ (**left**), and $G^{\theta\theta}_{\rm O}$ (**right**), which define the geometrical coupling of the light path in the non-radial interferometer arm segment to longitudinal and transverse quantum gravity fluctuations, respectively.

sensitivity to transverse fluctuations $h_{\theta\theta}$ can be maximised for a bend angle of the arms $\beta_{X,Y} \approx 60°$ and $R \approx 1$ (such that $L_I \approx L_O$).

2.3.4 Frequency Domain Signal

The frequency domain signal produced by the quantum space-time fluctuations, specifically the power spectral density of the length fluctuations, can be found by taking the Fourier transform of the two-time correlation function in Eq. 2.29:

$$P_{xx}(f) = \int_{-\infty}^{\infty} \langle \delta L(t_1) \delta L(t_2) \rangle \, e^{-2\pi i f \tau} \, d\tau, \tag{2.43}$$

which gives,

$$P_{xx}(f) = \frac{l_{\mathrm{P}}^{2\alpha}}{c} \left(A_{rr} (L_{\mathrm{I}})^{(\frac{3}{2}-\alpha)} \mathrm{sinc}\left(\frac{\pi L_{\mathrm{I}} f}{c}\right) + \left(\langle \lambda_{\mathrm{O}}^{i\prime} \lambda_{\mathrm{O}}^{j\prime} \rangle A_{ij}^2 \right)^{\frac{1}{2}} (L_{\mathrm{O}})^{(\frac{3}{2}-\alpha)} \mathrm{sinc}\left(\frac{\pi L_{\mathrm{O}} f}{c}\right) \right)^2, \tag{2.44}$$

in SI units (m^2/Hz), and the amplitude spectral density is the square root of $P_{xx}(f)$. When evaluated for $\alpha = 1/2$, Eq. 2.44 has the same form as previous results for quantised space-time signals in interferometers that consider the case $\alpha = 1/2$ [8, 20, 67].

2.3.5 Cross-Spectral Density Signal in Co-Located Interferometers

In theory, the signal described by Eq. 2.44 is detectable in a single instrument [8]. However, theories of quantum space-time fluctuations based on the holographic principle suggests that measurements within the same causally connected volume of space-time are correlated [88](see Sec. 2.2). Therefore, the signal due to quantum space-time fluctuations in a single instrument should be coherent to some degree with the signal in an identical interferometer in the same volume of space-time. As dominant sources of noise are expected to have limited coherence between the interferometers, it is expected that the common signal from quantum space-time fluctuations can be resolved in the time-integrated cross-spectral density of co-located instruments. This approach has significant practical advantages over the use of a single instrument, as explained in Sec. 1.2.1.

In a simple holographic scenario, it may be expected that the strength of the correlations of these measurements is proportional to the overlapping volume of the causal diamonds defined by the respective measurements (see Fig. 2.5) [20, 89]. In the unrealistic approximation that the interferometers are truly co-located, the causal diamonds defined by the two interferometers overlap fully, and the cross-spectral signal is equal to the auto-spectral signal (Eq. 2.44). The overlap of the individual causal diamond is itself a causal diamond of size $2L - d$, where d is the separation between the interferometers and $2L$ is the size of causal diamonds defined by a single interferometer [90]. Imperfections of the identicality of the twin interferometers, specifically in the

lengths and angles, may also decrease the overlap of the causal diamonds, but these geometrical imperfections can easily be limited such that their effect is much smaller than the effect of the separation between the interferometers. The signal in the cross-spectrum is thus expected to decrease as $\sim 2d/L$ to first order for inter-instrument separations that are small compared to the spatial radii of the individual causal diamonds.

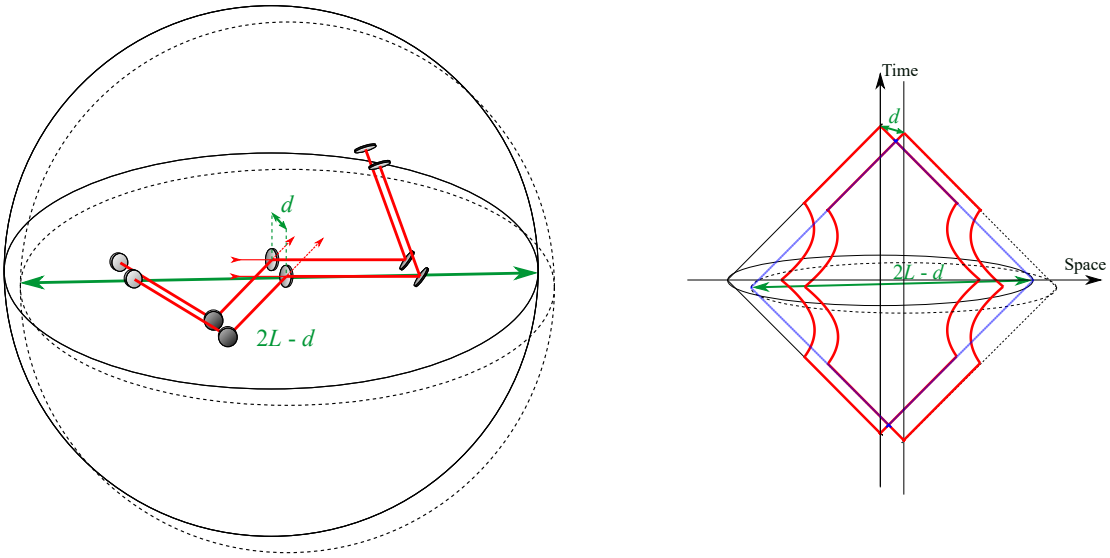

Figure 2.5. left: Schematic of the two identical co-located interferometers with three-dimensional arms of total optical path length L. The interferometers are separated by a distance d. The spheres are the boundaries of causal diamonds defined by the experiment. **right:** Space-time diagram of four photons traversing both arms in both interferometers from beamsplitter to end mirror and back. The photon paths are projected onto the radial spatial direction, and the two transverse spatial directions are suppressed. The solid and dashed squares are the causal diamonds defined by the departure and return of the photons from the beamsplitters in either interferometer. The boundaries of these causal diamonds are the solid and dashed space-like circles, which represent the same surfaces as the solid and dashed spheres in the diagram on the left. The blue rectangle is the overlap of these two causal diamonds, which is also a causal diamond of size $2L - d$.

2.3.6 Conclusions and Future Work

A simple model for the measured length changes of an interferometer arm due to quantum-space time fluctuations has been formulated. The model translates the established qualitative phenomenological predictions (Eq. 2.7) for the variance of distance measurements into a quantitative frequency domain signal as a function of the scaling of the fluctuations α and the geometry of the arm.

The model does not yet capture some important aspects of both the theorised quantum space-time fluctuations and the laser interferometers. Specifically, the model does not capture the proposed angular correlations [8] of the fluctuations. More importantly, the model does not incorporate the propagation of coherent states of light and their interaction with metric fluctuations. It also does not capture the interference of light at a beamsplitter and the measurement of the output state at the output port of the interferometer using a photodiode. The model also cannot accurately describe correlations between co-located interferometers. Work is ongoing on a more sophisticated model that addresses these issues [84].

2.4 Prospects for Detecting Quantum Gravity Phenomena with QUEST

Given the expected sensitivity of the QUEST experiment (Sec. 1.5), the prospects for detecting signals from holographic quantum space-time fluctuations can be evaluated. In Fig. 2.6, we show projected instantaneous and cross-correlated sensitivities of the QUEST experiment in terms of the strain noise amplitude spectral density, plotted as a function of frequency normalised to the interferometer arm light-crossing frequency (c/L). We also show the instantaneous and the time-integrated sensitivities achieved by the Fermilab Holometer [18]. The predicted signal spectra of holographic quantum space-time fluctuations [63, 64] are shown as well.

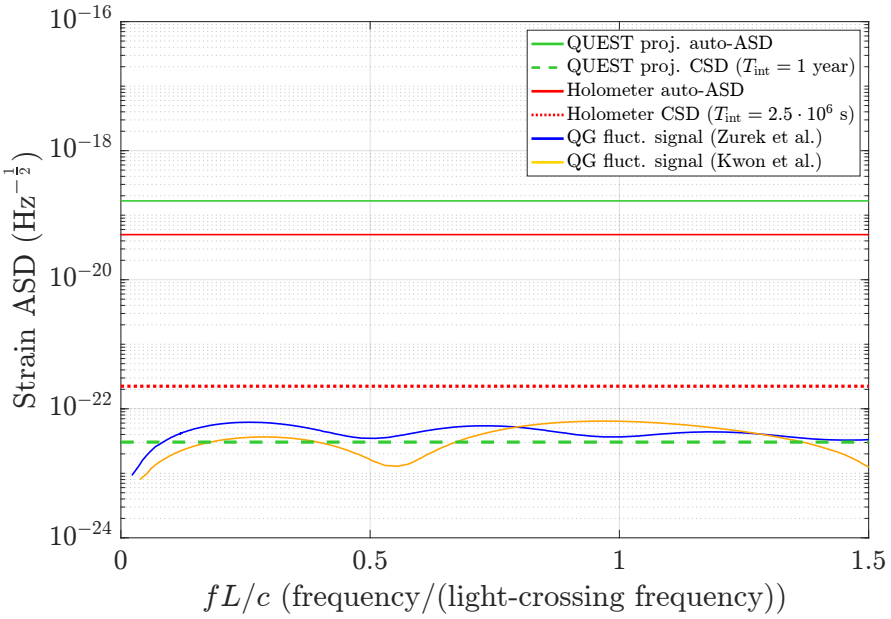

Figure 2.6. The projected sensitivity of the QUEST experiment is shown compared to the sensitivity of the Fermilab Holometer and the predicted signals due to holographic quantum space-time fluctuations. The projections for the QUEST experiment assume a shot-noise-limited sensitivity between 1 and 250 MHz with 6 dB of squeezing (See Sec. 1.5). The sensitivity of the Holometer is taken from [18]. The signal spectra for the models by Zurek et al. and Kwon et al. are taken from [63], and [64], respectively (see also Sec. 2.2).

It is thus estimated that a cross-correlation time on the order of a year is needed to reach a cross-spectral sensitivity on the order of the predicted magnitude of the quantum space-time time signal. The data can then be used to test the models of quantum

space-time fluctuations in literature, and may provide the first observation of quantum gravity phenomena.

3: Dark Matter

In this chapter, we demonstrate the use of laser interferometers to search for scalar field dark matter. We did not detect any signals from such dark matter, and could therefore place constraints on its properties. These constraints improve over those set by purpose-built dark matter detectors by orders of magnitude. We also present a design for a table-top polarimetric dark matter detector that could be used to test scalar and pseudoscalar dark matter models with unprecedented sensitivity.

We also comment on the prospects for searches for dark matter with the QUEST experiment.

Contributions to published work in this chapter
Section 3.3 of this chapter is based on the article

- Vermeulen, S. M. *et al.* "Direct limits for scalar field dark matter from a gravitational-wave detector". *Nature* **600.** ISSN: 1476-4687 (Dec. 2021).

S.M.V. lead the analysis, proposed the use of the modified LPSD method, and wrote a large majority of the manuscript. Section 3.4 of this chapter is based on the article

- Aiello, L. *et al.* "Constraints on Scalar Field Dark Matter from Colocated Michelson Interferometers". *Phys. Rev. Lett.* **128,** 121101 (12 Mar. 2022).

S.M.V. contributed to the analysis, in particular the analysis of the coupling of dark matter to co-located interferometers and the statistical analysis of spectral data, and wrote a large part of the manuscript. Section 3.5 of this chapter is based on the manuscript

- Ejlli, A. *et al.* "Probing dark matter with polarimetry techniques". arXiv:2211.09922, accepted for publication in Phys. Rev. D. Nov. 2022.

S.M.V. proposed the use of the polarimetry setup in question for detecting pseudoscalar dark matter, derived the coupling of scalar and pseudoscalar dark matter to birefringence, contributed to the noise budget and sensitivity projections, and wrote a large part of the manuscript.

3.1 Introduction: History and Current State of the Concept of Dark Matter

Dark matter is a concept that was introduced to explain several astronomical observations; it is also an essential part of cosmological theories. In this section, we expand on its inception, the current state of the field, and the use of laser interferometers in dark matter searches.

In general, it is assumed that General Relativity accurately describes the gravitational dynamics of astronomical objects and the Universe as a whole, according to the Einstein equations:

$$G_{\mu\nu} + \Lambda g_{\mu\nu} = T_{\mu\nu}. \tag{3.1}$$

The energy-momentum tensor $T_{\mu\nu}$ accounts for sources of gravity (e.g. mass) that curve the space-time manifold (described by the Einstein tensor $G_{\mu\nu}$) and thus give rise to certain dynamics. Using observations of light emitted by an astrophysical system, the energy-momentum tensor can be estimated under the assumption that the distribution of mass in the astrophysical system is related to the amount of electromagnetic radiation detected. If the expected dynamics of astronomical objects are then calculated from the Einstein equations under this assumption, a significant discrepancy is found with the observed dynamics. Examples of such discrepancies include the rotation speed of galaxy clusters [91], the rotation speed of individual galaxies [92], and gravitational lensing by galaxies [93].

Given these discrepancies, it is often concluded that the second assumption—the proportionality between light emitted by the system and the mass-energy in the system—must be false, rather than the first assumption (the validity of General Relativity). This then leads to the postulate that there exists unobserved mass-energy in the astrophysical system—specifically 'dark' matter that does not emit light—that needs to be added to the energy-momentum tensor on the right-hand side of Eq. 3.1 to restore the validity of General Relativity. Similarly, in cosmology, models that seek to describe the structure and expansion of the Universe according to General Relativity incorporate a parameter for the total amount of dark matter, the value of which is then fit to observations. These dark matter postulates mostly leave open the question what the nature of this dark matter is.

There are different approaches to the reconciliation of astronomical observations with theory that do not postulate the existence of dark matter. Instead of adding source terms to the right-hand side of Eq. 3.1, one could modify the left-hand side; these approaches are known as 'modified gravity'. A third solution can be imagined, where a

supersession of General Relativity, for example by a theory of quantum gravity, provides a new law of gravitation to supplant the Einstein equations. These solutions have always been regarded as less simple and therefore less scientific, but as some observations seem increasingly incompatible with the postulate of dark matter [94–97], this could change.

Around the time that the dark matter postulate gained popularity, contemporary physics was very successful in describing all known matter as a set of interacting quantum fields, collectively known as the Standard Model. It is within this particle physics paradigm that the nature of dark matter seemed readily explicable as just another quantum field, yet to be detected directly and yet to be included in the Standard Model. Moreover, aesthetic considerations, often called 'naturalness' or 'fine-tuning' problems, motivated the conjecture that additional undiscovered fields with certain properties should exist, i.e. supersymmetry. Some of these fields were conjectured, coincidentally, to have properties such that they would manifest as an energy density that would correspond to the energy density attributed to dark matter.

It was this apparent coincidence that drove the search for weakly-interacting particles with masses between $\sim$ 10 GeV and 1 TeV, known as WIMPs. Experiments sought to detect WIMPs by first creating them using particle colliders, or by looking for the scattering of WIMPs naturally present throughout our galaxy off atomic nuclei. None of the experimental searches for WIMPs have been successful so far, and therefore most of the original theories of such dark matter particles are falsified. Another more recent example of a particle dark matter theory largely motivated by 'fine-tuning problems' is that of the axion, which has likewise not been detected to date.

However, altogether undeterred or perhaps motivated by these failures, a large number of new theories of particle dark matter were formulated and continue to be formulated to this day. This theoretical work is undoubtedly enabled by the success of the Standard Model—which does not preclude the addition of new fields—and the utility of quantum field theory as a general framework to produce theoretical predictions. Dark matter particles contrived using this machinery often follow generic routines: an unobserved symmetry of Nature is presumed to exist and be broken, a Lagrangian is formulated, and parameterised couplings to the known fields of the Standard Model are added; these couplings are usually such that they are weak enough for the particle to have evaded detection thus far, strong enough to make the theory experimentally testable in the future, but otherwise entirely unconstrained. The theories of dark matter particles so produced therefore contain several free parameters (i.e. the mass of the field and strength of the various couplings) that can span tens of orders of magnitude.

The multitude of particle dark matter models and their lack of specificity poses a problem for experimental physics. The abundance and continuous production of predictions that are equally falsifiable (and all equally subjective in their motivation)

removes much of the incentive for a targeted long-term experimental effort. However, the discrepancies between theory and observation attributed to dark matter remain, and their reconciliation is undeniably a necessary pursuit of physical research. It has been argued that in the search for dark matter, "no stone should be left unturned", and "we should look for dark matter not only where theoretical predictions dictate that we 'must', but wherever we can" [98].

Laser interferometers provide a tool with which to do the latter. The instruments discussed in this chapter have been developed with the primary goals of detecting gravitational waves and signatures of quantum gravity, and we demonstrate their use in testing theories of particle dark matter. Our efforts represent searches for dark matter without the need for dedicated experiments, and moreover, these searches even outperform purpose-built dark matter detectors.

Several ideas have been put forward as to how different hypothetical forms of dark matter can couple to laser interferometers and produce a signal. Macroscopic dark matter candidates that couple with interferometers gravitationally, nongravitationally, or both, have been considered in the literature. One category of such scenarios entails detectable local stochastic interactions between 'clumpy' DM and interferometer components [99–101]. Primordial black holes are also macroscopic dark matter candidates, and their existence can be probed through searching for the high-frequency gravitational waves emitted during their coalescence.

Most proposals for couplings between dark matter and laser interferometers concern undiscovered weakly interacting, low-mass (sub-eV) fields. For example, undiscovered vector bosons (sometimes called dark photons) could exert an oscillatory force on interferometer components, producing an oscillatory signal at a frequency determined by the boson's mass [13]. In addition, undiscovered low-mass fields could form topological defects, which could produce a transient signal through the interaction between the interferometer and a passing defect [102]. Axion-like particles could be indirectly detected through the detection of gravitational-waves emitted from black hole superradiance [103].

The focus of the work presented here is a subclass of low-mass dark matter theories that postulates non-gravitational couplings of light scalar or pseudo-scalar fields to the electromagnetic field and fermions, whereby fundamental constants oscillate. This causes the size of interferometer components to oscillate, producing a signal at a frequency set by the mass of the field.

In this chapter we present the first ever direct search for scalar field dark matter with a gravitational wave-detector (the GEO 600 interferometer, see Sec. 3.3), a search for scalar field dark matter with the Fermilab Holometer (Sec. 3.4), and a proposed design for a polarisation interferometer (polarimeter) to search for scalar and pseudo-scalar dark matter (Sec. 3.5). We also discuss the prospects for searching for dark matter using

the QUEST experiment in Sec. 3.6.

3.2 Theory of Low-Mass Scalar and Pseudoscalar Dark Matter

3.2.1 Scalar Field Dark Matter

Equation of motion and coupling to the Standard Model

Models of weakly coupled low-mass ($\ll 1\,\mathrm{eV}$) scalar fields predict that such particles could be produced in the early Universe through a vacuum misalignment mechanism, and would manifest as a coherently oscillating field [104, 105],

$$\phi(t,\vec{r}) = \phi_0 \cos\left(\omega_\phi t - \vec{k}_\phi \cdot \vec{r}\right), \tag{3.2}$$

where $\omega_\phi = (m_\phi c^2)/\hbar$ is the angular Compton frequency, and $\vec{k}_\phi = (m_\phi \vec{v}_{\mathrm{obs}})/\hbar$ is the wave vector, with m_ϕ the mass of the field and $\vec{v}_{\mathrm{obs}}$ the velocity relative to the observer. The amplitude of the field can be set as $\phi_0 = (\hbar\sqrt{2\rho_{\mathrm{local}}})/(m_\phi c)$, under the assumption that this scalar field constitutes the local dark matter (DM) density ρ_{local} [106].

These models predict such DM would be trapped and virialised in gravitational potentials, leading to a Maxwell-Boltzmann-like distribution of velocities $\vec{v}_{\mathrm{obs}}$ relative to an observer. Non-zero velocities produce a Doppler-shift, giving an observed DM field frequency

$$\omega_{\mathrm{obs}} = \omega_\phi + \frac{m_\phi \vec{v}_{\mathrm{obs}}^2}{2\hbar}. \tag{3.3}$$

This virialisation therefore results in the DM field having a finite coherence time or, equivalently, a spread in observed frequency (linewidth) $\Delta\omega_{\mathrm{obs}} \approx 1/\tau_{\mathrm{coh}}$ [13, 107]. The linewidth is determined by the virial velocity, which is given by the depth of the gravitational potential. For DM trapped in the gravity potential of the Milky Way, as in the standard galactic DM halo model, the expected linewidth is $\Delta\omega_{\mathrm{obs}}/\omega_\phi \sim 10^{-6}$ and correspondingly the expected coherence time $\tau_{\mathrm{coh}} \approx 10^6/\omega_\phi$. The observed DM frequency is further modulated by the motion of the Earth with respect to the local DM's centre of mass. Note that the spatial frequency of the field is given by the De Broglie wavelength of the particle, $\lambda_\phi = 2\pi/|\vec{k}_\phi|$, which depends on the kinetic energy, and for dark matter in a galactic halo, this wavelength is around a thousand times larger than the field's Compton wavelength [107].

Scalar field DM could couple to the fields of the Standard Model (SM) in numerous ways. Such a coupling, sometimes called a 'portal', is modelled by the addition of a parameterised interaction term to the SM Lagrangian [108, 109]. In this work, we consider linear interaction terms with the electron rest mass m_e and the electromagnetic

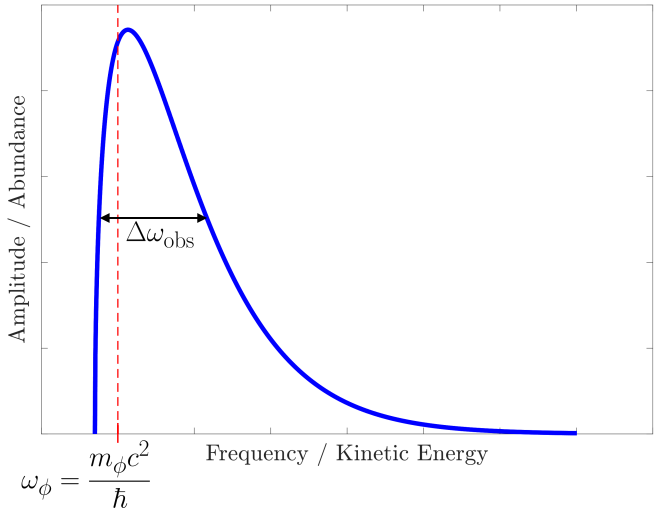

Figure 3.1. The spectrum of ultra-light dark matter trapped and virialised in a gravitational potential. The field would be observed with a frequency roughly equal to the Compton frequency of the particles (ω_ϕ), where the deviation is a Doppler-shift due to the particles' nonzero kinetic energy. As the particles would have a Maxwell-Boltzmann-like distribution of kinetic energies, the spectrum resembles this distribution. The width of the distribution $\Delta\omega_{\rm obs}$ is set by the depth of the gravitational potential that the field is trapped in, where for a conventional galactic dark matter halo $\Delta\omega_{\rm obs}/\omega_\phi \approx 10^{-6}$.

field tensor $F_{\mu\nu}$:

$$\mathcal{L}_{\rm int} \supset \frac{\phi}{\Lambda_\gamma}\frac{F_{\mu\nu}F^{\mu\nu}}{4} - \frac{\phi}{\Lambda_e} m_e \bar{\psi}_e \psi_e, \tag{3.4}$$

where ψ_e, $\bar{\psi}_e$ are the SM electron field and its Dirac conjugate, and Λ_γ, Λ_e parameterise the coupling. It has been argued that the scalar field should obey parity symmetry (Z_2 symmetry), or invariance of the Lagrangian under the transformation $\phi \to -\phi$. In that case linear couplings would not exist, and the simplest couplings would be terms quadratic in ϕ. As such scenarios entail additional assumptions about dark matter, we will not consider higher-order couplings.

The addition of extra terms to the SM Lagrangian necessarily changes the dynamics described by it. The presence of an oscillating DM field interacting with the SM fields gives rise to apparent oscillations of the fundamental constants at the frequency of the DM field. For the coupling given by Eq. 3.4, the electron rest mass m_e and the fine structure constant α will vary as [12, 105]

$$m_e \to m_e\left(1 + \frac{\phi}{\Lambda_e}\right), \quad \alpha \to \alpha\left(1 + \frac{\phi}{\Lambda_\gamma}\right). \tag{3.5}$$

Scalar field dark matter scenarios

A variety of specific scalar field dark matter models with linear couplings to the electromagnetic sector of the SM exist. These include the hypothetical moduli and dilaton fields motivated by string theory, which have couplings to the QCD part of the SM as well [110–112]. These other couplings make such undiscovered massive scalars subject to additional experimental constraints, although the predicted phenomenology due to the electromagnetic coupling terms (Eq. 3.4) remains unchanged. Relaxions are non-dilatonic scalars which couple to the standard model by mixing with the Higgs field [113]; however, their coupling to the electromagnetic sector can be effectively described by Eq. 3.4 and thus relaxion DM would produce the same variation of the fundamental constants. In addition, relaxion DM [113, 114] may form gravitationally bound objects and be captured in the gravitational potential of the Earth or Sun, producing a local DM overdensity where the field has a much narrower linewidth [115] than DM that forms a galactic halo. A relaxion halo centred on Earth for example, would entail a DM field with a linewidth smaller than that of galactic halo DM by three orders of magnitude, and a density greater by up to 19 orders of magnitude [114].

Given the large number of different scalar field dark matter models (which are not necessarily mutually exclusive) that can be tested with interferometers, we have to restrict the scope of our DM searches to a subset of scenarios for the nature and abundance of scalar field dark matter. Using contemporary literature as precedent provides a subjective preference for certain scenarios, of which we choose three to investigate with interferometers:

1. *Basic Scalar*: The scalar field DM is assumed to interact with the SM as given by the terms in 3.4, and is further assumed to be homogeneously distributed over the solar system with a density of $\rho_{\mathrm{GH}} = 0.4$ GeV/cm^3, as in the standard galactic DM halo model [106].

2. *Dilaton/Modulus*: In addition to the coupling to the electromagnetic sector as in Eq. 3.4, the field is assumed to have couplings to the QCD sector, and the coupling to the gluon field is assumed to be dominant [110–112, 116]. The local DM density is taken to be ρ_{GH}. Compared to the *Basic Scalar*, this scenario is subject to additional limits from tests of the equivalence principle, but is equally constrained by our result and those of other direct searches.

3. *Relaxion Halo*: In this scenario, the scalar field effectively couples to the SM as in the *Dilaton/Modulus* scenario, but these couplings arise through mixing with the Higgs boson [113, 114]. The local DM density in this scenario is taken to be dominated by a relaxion halo gravitationally bound to earth, which leads to

a local overdensity that depends on the field's mass and reaches values of up to $\rho_{\rm local}/\rho_{\rm GH} = 10^{19}$ for the mass range constrained in this work [115].

For all scenario's, we consider the electron and photon couplings (Eq. 3.4) to give rise to the dominant interferometric signal. While signals might arise due to couplings to other parts of the SM, the relative amplitude of these will be several orders of magnitude smaller than that from the electromagnetic couplings [117]. We consider a range of field masses m_ϕ corresponding to the sensitive frequency range of the interferometer in question.

Coupling to interferometers

The addition of the terms in Eq. 3.4 to the SM Lagrangian entails changes of the fine structure constant α and the electron rest mass m_e [102, 104]. The size of a solid is proportional to the atomic Bohr radius, i.e $l \propto a_B = 1/(m_e\alpha)$ [118], where α is the fine structure constant and m_e is the electron mass. The apparent variation of these fundamental constants therefore changes the lattice spacing of a solid, driving changes of its size l:

$$\frac{\delta l}{l} = \left(-\frac{\delta\alpha}{\alpha} - \frac{\delta m_e}{m_e}\right)\left(\left|1 - \frac{\omega_\phi^2}{\omega_0^2}\right|\right)^{-1}, \tag{3.6}$$

where δx denotes a change of the parameter x: $x \to x + \delta x$; ω_0 is the angular frequency of the fundamental longitudinal vibrational mode of the solid driven by the scalar field, and we consider a strongly underdamped system. The refractive index depends on the electronic resonances of the solid. If we only consider frequencies far away from the nearest electronic resonance $\omega_\phi \ll \omega_e$, the index of refraction is approximately inversely proportional to the electronic resonance of the solid, i.e. $1/n \propto \omega_e \propto m_e\alpha^2$, and so

$$\frac{\delta n}{n} = C_{\rm disp}\left(2\frac{\delta\alpha}{\alpha} + \frac{\delta m_e}{m_e}\right), \tag{3.7}$$

where $C_{\rm disp} = \omega/n \cdot \partial n/\partial\omega$ takes into account the chromatic dispersion of the solid. For a more careful consideration of the approximations used in deriving Eqs. 3.6, 3.7, see [12].

The thin cylindrical beamsplitter in a laser interferometer interacts asymmetrically with light from the two arms, as the front surface has a 50% reflectivity and the back surface has an anti-reflective coating. Therefore, a change in the size (δl) and index of refraction (δn) of the beamsplitter affects the two arms differently, and produces an effective difference in the optical path lengths of the arms $L_{x,y}$

$$\delta(L_x - L_y) \approx \sqrt{2}\left[\left(n - \frac{1}{2}\right)\delta l + l\delta n\right]^{1}, \tag{3.8}$$

The two terms in this equation correspond to the increase in the optical path length of the x-arm due to the increased thickness of the beamsplitter, and the increased optical path length of the x-arm due to the increased refractive index of the beamsplitter, respectively. The mirrors in the arms of interferometers would also undergo changes in their size and index of refraction, but as the wavelength of the DM field is much greater than the distance between the arm mirrors ($\lambda_\phi/L \gtrsim 10^3$) for all frequencies of interest here, and because the mirrors have roughly the same thickness, the effect is almost equal in both arms and thus does not produce a dominant signal.

To find the expected DM signal in a Michelson interferometer, we plug Eq. 3.5 into Eqs. 3.6 and 3.21; we then plug these equations into Eq. 3.8. Thus, it follows that the coupling of an oscillating scalar dark matter field to the beamsplitter of a Michelson interferometer is expected to produce a Doppler-shifted and -broadened signal of the form [3]

$$\delta(L_x - L_y) \approx \left(\frac{2\,c\,\sqrt{\rho_{\rm local}}}{\omega_\phi}\right) \cdot \cos(\omega_\phi t) \cdot \left[\mathrm{sinc}\left(\frac{\omega_\phi L}{c}\right)\right]^{-1} \tag{3.9}$$
$$\cdot\, l \cdot \left\{\left(n - \frac{1}{2}\right) \cdot \left(\left|1 - \frac{\omega_\phi^2}{\omega_0^2}\right|\right)^{-1} \cdot \left(\frac{1}{\Lambda_\gamma} + \frac{1}{\Lambda_e}\right) + nC_{\rm disp}\left(\frac{2}{\Lambda_\gamma} + \frac{1}{\Lambda_e}\right)\right\},$$

where the first two terms describe the oscillating dark matter field (with the dark matter amplitude set by the local dark matter density), and the sinc function describes the modulation of the signal due to the periodic frequency response of an interferometer with arms of length L. The terms on the second line of Eq. 3.9 describe the magnitude of the coupling of the dark matter field to the beamsplitter of the interferometer.

3.2.2 Pseudoscalar Dark Matter

Light pseudoscalar fields, including the axion and other axion-like particles, manifest themselves as an oscillating classical field, analogous to the scalar case [119–123]:

$$a(t, \vec{r}) = a_0\, \cos\Big(\omega_a t - \vec{k}_\phi \cdot \vec{r}\Big), \tag{3.10}$$

where $\omega_a = (m_a c^2)/\hbar$ is the angular Compton frequency for a pseudoscalar field mass m_a, the amplitude $a_0 = (\hbar\sqrt{2\rho_{\rm local}})/(m_a c)$, and the other variables are the same as for Eq. 3.2. We consider the coupling of the axion-like to the photon field parameterised by $g_{a\gamma}$ [124]

$$\mathcal{L}_{\rm int} = \frac{a}{g_{a\gamma}} \frac{F_{\mu\nu}\tilde{F}^{\mu\nu}}{4}, \tag{3.11}$$

[1]This expression includes a correction to Eq. 17 in [12]. In addition, a geometrical correction ($\approx 6.4\%$) from Snell's law is applied to Eqs. 3.8 for calculating the results in this work.

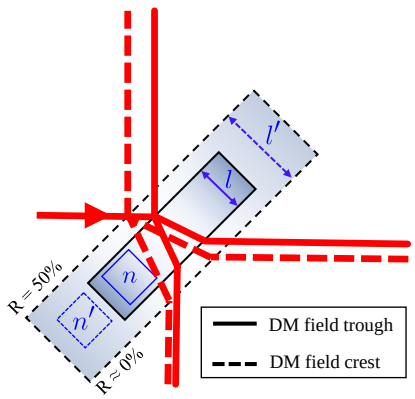

Figure 3.2. The geometry of light (red) incident on a beamsplitter in an interferometer. Wave-like low-mass scalar field dark matter changes the size and index of refraction of the beamsplitter in an oscillatory fashion. The size increase shifts the front surface (with a reflectivity $R = 50\%$) w.r.t. the beamsplitter's centre of mass, producing a difference in the optical path length of the two arms. The change of the index of refraction of the bulk of the beamsplitter also produces an optical path length difference. The back surface of the beamsplitter has an anti-reflective coating.

where $g_{a\gamma}$ is the axion-photon coupling constant, $\tilde{F}^{\mu\nu} = \epsilon^{\mu\nu\rho\sigma}F_{\rho\sigma}$, and $\epsilon^{\mu\nu\rho\sigma}$ is the Levi-Civita symbol. Due to this coupling of photons with the axion-like field, there would be a difference in the phase velocity of right- and left-handed circularly polarized light [125]:

$$v_{↻,↺} \approx 1 \pm \frac{g_{a\gamma}\dot{a}}{2k} \tag{3.12}$$

Therefore, the right- and left-hand circular polarisation components of light accumulate a relative phase difference, which produces a rotation of the plane of polarisation of linearly polarized light by an angle [126]

$$\rho(t,\tau) = \frac{g_{a\gamma}}{2}\left[a(t) - a(t-\tau)\right], \tag{3.13}$$

for light propagating between times $t-\tau$ and t. For propagation times $\tau \ll 1/\omega_a$, we have

$$\rho(\omega_a,\tau,t) \approx g_{a\gamma}a_0\omega_a\tau\sin(\omega_a t), \tag{3.14}$$

to first order. This rotation of the polarisation of light is not readily detectable in a Michelson interferometer with arms of length L, as the effect in both arms will be equal for dark matter wavelengths $\lambda_\phi \gg L$, which is the case in the sensitive frequency band of

most laser interferometers. In Sec. 3.5, we propose a design for a polarimetric experiment that would be sensitive to pseudoscalar dark matter.

3.3 Search for Scalar Field Dark Matter with GEO600

3.3.1 Introduction

The interferometer most sensitive to potential DM signals is the GEO 600 detector [127], as it has the highest sensitivity to optical phase differences between the two arms as evaluated at the beamsplitter. Although other GW detectors (LIGO/Virgo) are more sensitive to gravitational waves through the use of Fabry-Pérot cavities in the arms, these do not boost their sensitivity to signals induced at the beamsplitter, so their relative sensitivity to scalar DM is lower [12]. The GEO 600 interferometer has been in joint observing runs with the Advanced LIGO detectors since 2015, primarily to look for gravitational waves.

From Eq. 3.9 it follows that an oscillating scalar dark matter field is expected to produce a Doppler-shifted and -broadened signal in the GEO 600 interferometer. We can simplify this equation for signals that would be found in the data of GEO 600 by considering the properties of the instrument and the calibration of the data. Firstly, as the mechanical resonance frequency of the GEO 600 beamsplitter is much higher than any signal frequency captured by the data, we consider the adiabatic limit for the dark matter-driven size changes of the beamsplitter [12, 111, 128]. Secondly, we neglect the contribution of the refractive index changes to the signal, as it would be three orders of magnitude smaller than that of the size changes. Finally, the frequency response of the interferometer is already incorporated in the calibration of the data [129], so we omit the sinc function. A dark matter signal would thus have the following form in the data of the GEO 600 interferometer:

$$\delta(L_x - L_y) \approx \left(\frac{1}{\Lambda_\gamma} + \frac{1}{\Lambda_e}\right)\left(\frac{n\,l\,\hbar\sqrt{2\,\rho_{\rm local}}}{m_\phi\,c}\right)\cos\left(\omega_{\rm obs}t\right), \tag{3.15}$$

Given this prediction, we can examine the data from the interferometer for the presence of such oscillatory signals, and if none are found, place upper limits on the mass and coupling constants of scalar field DM.

3.3.2 Methods

Spectral analysis

We performed spectral analysis on seven $T \sim 10^5$ s segments of strain data from the GEO 600 interferometer [127] (acquired in 2016 and 2019) using a modified version of the LPSD (Logarithmic Power Spectral Density) technique [130]. This technique is designed to produce spectral estimates with logarithmically spaced frequency bins, and

thus allows for the production of spectral estimates with a frequency-dependent bin width; i.e. it is used to perform discrete Fourier transforms (DFT) with a frequency dependent length. This method was used to create spectra in which each frequency bin has a width equal to the expected linewidth of the DM signal; this approach yields the maximum attainable signal-to-noise ratio (SNR) given a certain amount of data (see Fig. 3.4). Using a modified version of the LPSD algorithm, we subdivided the $\sim 10^5$ s data segments into

$$N_f = \left\lfloor \frac{T - \tau_{\mathrm{coh}}(f)}{\tau_{\mathrm{coh}}(f)(1-\xi)} + 1 \right\rfloor \tag{3.16}$$

smaller overlapping subsegments $S_f^k(t)$ with a length equal to the expected coherence time $\tau_{\mathrm{coh}}(f)$ of the signal at a frequency f (where $\xi \in [0,1]$ is the fractional overlap of the subsegments, and $k \in [1, N_f]$). As the expected coherence time and linewidth is frequency dependent, this subdivision is unique for every frequency of interest.

After subdivision, the subsegments were multiplied with a window function $W_f(t)$ to suppress spectral leakage and subjected to a DFT at a single frequency:

$$a^k(f) = \sum_{t=0}^{T_{\mathrm{DFT}}} W_f(t)\, S_f^k(t)\, \mathrm{e}^{2\pi i f t}, \tag{3.17}$$

with $T_{\mathrm{DFT}} = \tau_{\mathrm{coh}}(f)$, where $a^k(f)$ is thus the complex spectral estimate at frequency f for the k^{th} subsegment. The absolute squared magnitudes $|a^k(f)|^2$ are then averaged over the subsegments to obtain the power spectrum

$$P(f) = \frac{C}{N_f} \sum_{k=1}^{N_f} |a^k(f)|^2, \tag{3.18}$$

where C is a normalisation factor. The amplitude spectrum $A(f) = \sqrt{P(f)}$ created in this way comprises $\approx 5 \cdot 10^6$ frequency bins between 50 Hz and 6 kHz. Computation times are ~ 10 s per frequency bin for each $\sim 10^5$ s data set, or $\sim 10^4$ CPU hours per spectrum.

As each frequency bin can be made to have a width equal to the DM signal's Doppler-broadened linewidth, this method yields in theory the maximum attainable signal-to-noise ratio (SNR) given a certain amount of data (see Sec. 3.3.2.4) [107, 131]. A matched filtering approach is not feasible as the phase of the signal varies stochastically.

Candidate signal search

We analysed the amplitude spectra of all seven strain data segments for the presence of DM signals by looking for significant peaks in the underlying noise. Peaks were

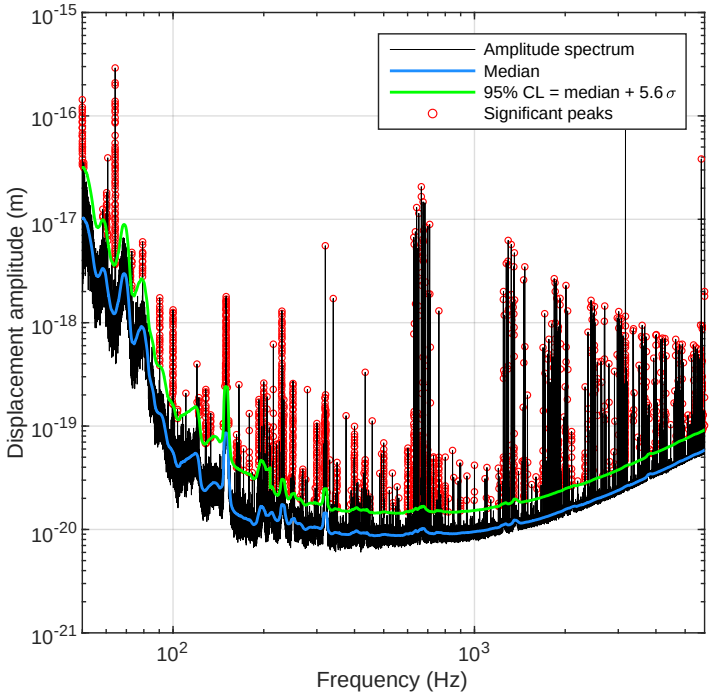

Figure 3.3. A typical amplitude spectrum (black) of the GEO600 detector produced with frequency bins that are tuned to the expected dark matter linewidth using the modified LPSD technique. The noise spectrum was estimated at each frequency bin from neighbouring bins to yield the local noise median (blue) and 95% confidence level (green). Peaks (red) above this confidence level were considered candidates for DM signals and subjected to follow-up analysis.

considered candidates when there is a less than 1% probability that the local maximum is due to noise, where we compensated for the look-elsewhere effect using a trial factor equal to the number of bins ($\approx 5 \cdot 10^6$). To determine this probability for every peak, the noise was assumed to be Gaussian with a frequency-dependent expectation value and variance. The local noise parameters were estimated at every frequency bin from $w = 5 \cdot 10^4$ neighbouring bins. This method allows the underlying noise distribution to be estimated in a way that is independent of narrow ($\ll w$) spectral features (such as those due to mechanical excitation of the mirror suspensions), under the assumption that the underlying noise spectrum is locally flat (that is, the auto-correlation length of the noise spectrum is assumed to be $\gg w$). The choice of w thus represents a trade-off between erroneously assuming instrumental spectral artefacts or signals to be features of the underlying noise spectrum versus erroneously assuming features of the underlying noise spectrum to be instrumental spectral artefacts or signals.

This analysis found $\sim 10^4$ peaks above the 95% confidence level ($\gtrsim 5.6\sigma$), where the total error includes a 10% amplitude calibration error inherent to GEO 600 data [132]. The frequency and amplitude stability of the peaks in time was then evaluated by cross-checking all candidates between spectra. Candidate peaks were rejected if their centre frequency differed between spectra by more than the Doppler shift expected from the earth's motion around the sun [133]. Peaks were also rejected if their amplitude changed significantly ($\gtrsim 5\sigma$) between spectra.

Using this procedure, we eliminated all but 14 candidate peaks, where the vast majority ($> 99\%$) of peaks was rejected because they did not appear in all data sets within the centre frequency tolerance.

Follow-up analysis of candidates

These 14 candidate peaks were subjected to further analysis to investigate if their properties matched that of a DM signal. 13 of the peaks were found to have insufficient width to be caused by DM ($\Delta f_{\mathrm{peak}}/\Delta f_{\mathrm{DM}} \lesssim 10$). Additional work revealed these 13 candidate peaks were not present in spectra created using the same data and the same LPSD algorithm implemented in a different programming language, whereas the noise floor and other spectral features were reproduced identically. These peaks are therefore likely artefacts of the numerical implementation of the LPSD technique. These peaks were therefore rejected as candidates for DM signals, as DM signals should appear as consistent peaks in the data, and as these peaks appear to have their origin in erroneous numerical processing.

The remaining candidate peak had sufficient frequency spread to be due to DM, but additional analysis showed this signal has a coherence time much greater than that expected for a galactic halo DM signal of that frequency ($\tau_c^{\mathrm{peak}}/\tau_c^{\mathrm{GH}} > 10$. This leaves open the possibility of the signal being due to scalar DM gravitationally bound to Earth, such as in a relaxion halo. The coherence time of the single remaining candidate peak was probed by evaluating its height in the amplitude spectrum as a function of the DFT length (see below). The height of the peak did not decrease for DFT lengths more than an order of magnitude greater than the expected DM coherence time, evidencing a coherence time much greater than that expected for a galactic DM signal of that frequency. To find the origin of the signal, and to check whether it could be due to the theoretically more coherent *Relaxion Halo* DM, we performed spectral analysis on data acquired on an auxiliary data acquisition system. The signal was not present in this data, whereas both noise and other signals from the interferometer were. This fact, in combination with high-resolution ($\Delta f/f \sim 10^{-7}$) spectra revealing that the frequency at which the peak occurs is very close to and indistinguishable from an integer ($f_{\mathrm{peak}} = 224 \pm (2 \cdot 10^{-5})$ Hz), implies the signal is most likely an artefact of a timing

signal in the main data acquisition electronics.

Validation of methods

To validate several aspects of our analysis methods, we simulated DM signals and injected them into sets of real and simulated data. The DM signals were created by superposing $\sim 10^2$ sinusoids at frequencies linearly spaced around a centre frequency (the simulated Doppler-shifted DM Compton frequency), where the amplitude of each sinusoid is given by the quasi-Maxwellian DM line shape proposed in [107] scaled by a simulated DM coupling constant; the relative phases of the sinusoids are randomised to capture the thermalisation of the scalar field DM.

To test the spectral estimation, signal search, and candidate rejection, a blind injection of simulated DM signals into several GEO 600 data sets was performed, where the frequency, amplitude, and number of signals was masked to the authors. All injected signals were recovered at their centre frequency and at an amplitude corresponding to the hypothetical coupling constant, and were subsequently identified through cross-checks between spectra as persistent candidate DM signals.

The formerly proposed [13, 107] and herein utilised condition of setting the frequency bin widths equal to the expected DM line width for attaining optimal SNR was tested using simulated DM signals as well. Mock DM signals and monochromatic sine signals were injected into real GEO 600 data and Gaussian noise, and spectra were made for which the width of the frequency bins Δf_{bin} (and correspondingly the length of the DFTs T_{DFT}) was varied over four orders of magnitude. The recovered amplitude of signals injected into GEO 600 data in spectra created using the LPSD algorithm is plotted in Fig. 3.4 (left). This shows that the recovered amplitude of signals starts to decrease as the DFT length exceeds the coherence time (a monochromatic sine has infinite coherence time), and validates the rejection of the remaining candidate signal above as its amplitude was found to be roughly constant for $T_{\mathrm{DFT}}/\tau_c > 10$. The recovered SNR of signals injected into Gaussian noise in spectra created using Welch's method [134] is plotted in Fig. 3.4 (right), which confirms that the SNR is maximal when the frequency bin width is roughly equal to the full-width at half-maximum Δf_{DM} of the spectral line shape of the signal. This is a consequence of the aforementioned decrease in recovered amplitude for smaller bin widths and the scaling of white Gaussian noise.

3.3.3 Results

Having determined that all significant peaks in the amplitude spectrum are not caused by scalar field DM, we can set constraints on the parameters of such dark matter at a 95% confidence level (corresponding to 5.6σ above the noise floor), using Eq. 3.15. We apply our results to three different scalar DM scenarios considered in literature: *Basic*

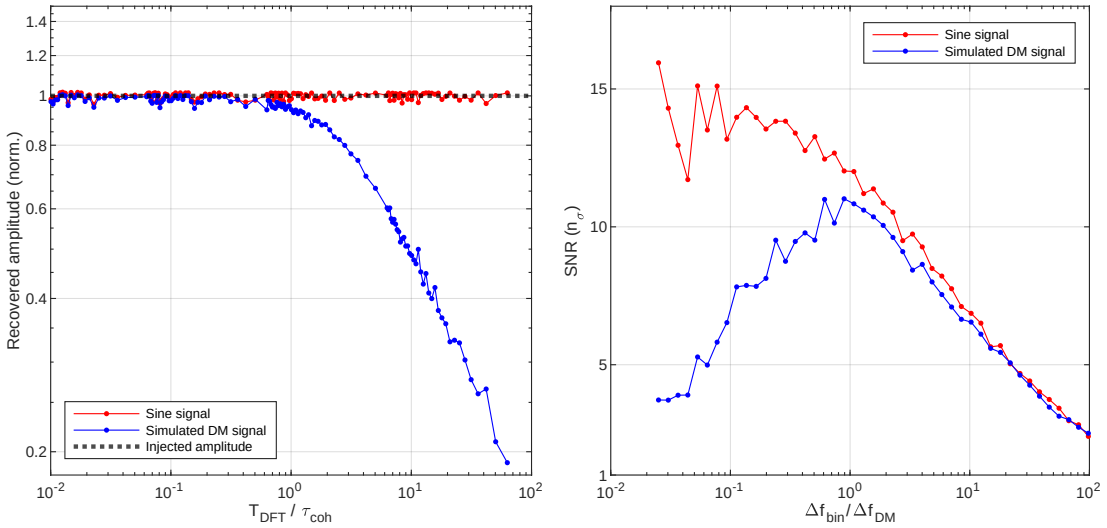

Figure 3.4. The spectral amplitude (left) and signal-to-noise ratio (SNR, right) of a simulated DM signal (blue) and monochromatic sine wave (red) as recovered from spectra created using different frequency bin widths ($\Delta f_{\mathrm{bin}} = 1/T_{\mathrm{DFT}}$). The plotted recovered amplitude is normalised by the injected amplitude. The SNR (n_σ) is measured as the difference between the signal amplitude and the noise amplitude divided by the standard deviation of the noise. The appearance of a maximum for the SNR as shown on the right is a direct consequence of both the decrease of the recovered amplitude of signals with limited coherence (as shown on the left) and the scaling of white Gaussian noise with increasing integration time. The plot on the left was produced by injecting a simulated dark matter signal and a perfect sine into a segment of GEO 600 data and creating spectra using the modified LPSD technique described above. The plot on the right was made by injecting the same signals into white Gaussian noise and creating spectra using Welch's method. Note that for any single bin and for equal T_{DFT} the spectral estimate obtained with the LPSD method (Eq. 3.17) is mathematically equal to that obtained with Welch's method.

Scalar, *Dilaton/Moduli*, and *Relaxion Halo* (see Sec. 3.2).

For each scenario, we set constraints on the electron and photon coupling parameters Λ_e, Λ_γ, as a function of the field's mass m_ϕ (where for each coupling constant we assume the other to be zero); the constraints are plotted in Figs. 3.5 and 3.6 together with previous upper limits. For the *Relaxion Halo* scenario, we assumed a mass-dependent halo density as described in [115].

Constraints from other direct experimental DM searches include those from various atomic spectroscopy experiments [135–138], a search using an optical cavity [139], and a resonant mass detector [140]. Tests of the equivalence principle (EP) using e.g. torsion

balances [116, 141, 142] have also been used to set constraints on the parameters of undiscovered scalar fields; these bounds assume the scalar field manifests as a 'fifth force' (FF), and is sourced by a test mass (e.g. the Earth) [109, 143, 144]. This detection method therefore assumes that the coupling terms in Eq. 3.4 are time-reversible; i.e. that a DM particle can be produced by electrons and photons. Moreover, the constraints on scalar fields inferred from these experiments depend in general on the composition and topography of the test masses and are independent of the local dark matter density. Therefore, constraints from such FF searches are not equivalent and are weaker than constraints from direct searches as they rely on a number of consequential additional assumptions.

3.3.4 Conclusions

In this work, we presented the first search for signals of scalar field dark matter in the data of a gravitational-wave detector. Scalar field dark matter would cause oscillations of the fine structure constant and electron mass, which in turn drive oscillations of the size and index of refraction of the beamsplitter in an interferometer. This would thus produce an oscillatory signal in a gravitational-wave detector at a frequency set by the mass of the dark matter particle.

As exquisite classical noise mitigation is employed in gravitational-wave detectors, quantum technologies such as squeezed light can provide a major increase in sensitivity. Such technologies facilitate measurements beyond the shot-noise quantum limit, and yield unprecedented sensitivity to scalar field dark matter in a wide mass range.

In addition, by tuning the frequency bin widths to the expected dark matter linewidth, our spectral analysis method improves on the analyses used in previous work that set constraints on dark photons using data from gravitational-wave detectors, and other searches for scalar fields in frequency space. In contrast to these other efforts, the spectral analysis presented here yields the optimal signal-to-noise ratio for potential dark matter signals across the full frequency range.

We excluded the presence of such signals in the data of the GEO 600 gravitational-wave detector, thereby setting new lower limits on dark matter couplings at up to $\Lambda_e, \Lambda_\gamma = 3 \cdot 10^{19}$ GeV for dark matter masses between 10^{-13} and 10^{-11} eV. The new constraints improve upon the current limits in this mass range obtained with atomic spectroscopy experiments by more than six orders of magnitude, and are up to four orders of magnitude more stringent than previous bounds from tests of the equivalence principle for some dark matter scenarios.

Tighter constraints on scalar field dark matter in various mass ranges can be set in the future using new yet-to-be-built gravitational-wave detectors or other similar precision interferometers. Using the same methods as in this work these instruments would allow

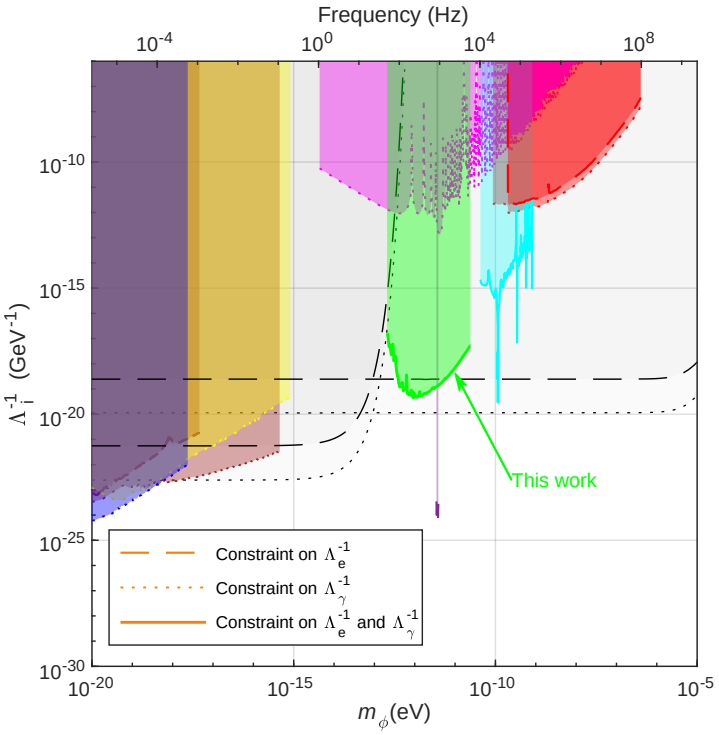

Figure 3.5. Constraints on the coupling parameters Λ_γ, Λ_e as a function of the field's mass m_ϕ, for scalar field DM as in the *Basic Scalar* scenario (see text). Dashed lines represent constraints on the electron coupling Λ_e and dotted lines represent constraints on the photon coupling Λ_γ, at the 95% confidence level. The green region denotes the parameter space excluded in the current study through the spectral analysis of data from the GEO 600 gravitational-wave detector. Other coloured regions indicate parameter space excluded through previous direct experimental searches; to wit, Hees et al [136] (blue), Van Tilburg et al [135] (yellow), Kennedy et al [145] (brown), Aharony et al [137] (magenta), Branca et al [140] (purple), Savalle et al [139] (cyan), and Antypas et al [138] (red)). The black curves and grey regions correspond to previous constraints from 'fifth-force' (FF) searches/tests of the equivalence principle (EP); to wit, the most stringent such constraints for this DM scenario are from the MICROSCOPE experiment [143, 144] (lower curves at low mass), and the Cu/Pb torsion pendulum experiment performed by the Eöt-Wash group [109, 116, 141] (at higher masses).

new limits to be set across their characteristic sensitive frequency range. Moreover, by slightly modifying the optics in such interferometers, e.g. by using mirrors of different thicknesses in each interferometer arm, their sensitivity to scalar field dark matter could be improved even further [12]. Through the reduction of losses, quantum technologies

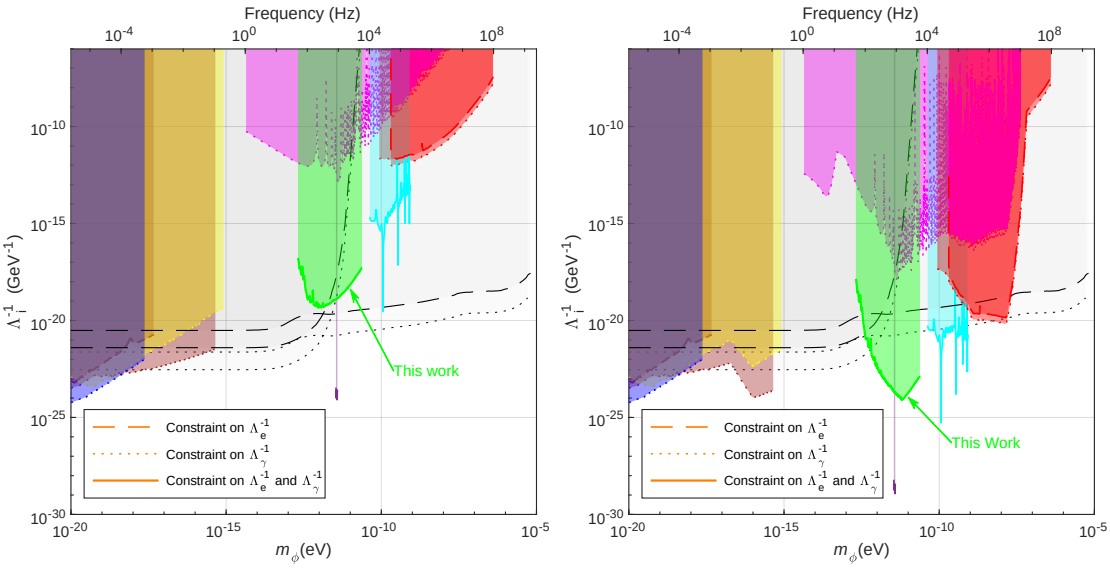

Figure 3.6. Constraints on the coupling parameters Λ_γ, Λ_e as a function of the field's mass m_ϕ, for scalar field DM as in the *Dilaton/Modulus* scenario (**left**) and the *Relaxion Halo* scenario (**right**). Dashed lines represent constraints on the electron coupling Λ_e and dotted lines represent constraints on the photon coupling Λ_γ, at the 95% confidence level. The green region denotes the parameter space excluded in the current study through the spectral analysis of data from the GEO 600 gravitational-wave detector. Other coloured regions indicate parameter space excluded through previous direct experimental searches ([135–138, 140, 145, 146], see caption of Fig. 3.5). The black lines and grey regions correspond to previous constraints from 'fifth-force' (FF) searches/tests of the equivalence principle (EP); to wit, the most stringent such constraints for this DM scenario are from the MICROSCOPE experiment [109, 143] (lower curves at low mass), and the Be/Ti torsion pendulum experiment performed by the Eöt-Wash group [109, 142] (at higher masses). The constraints for the *Relaxion Halo* scenario from direct experimental searches have been obtained by rescaling the originally reported constraints to account for the mass-dependent local overdensities as proposed in [115]. This produces novel constraints not reported before for *Relaxion Halo* DM from the results of [135–137, 140, 145]. The FF/EP constraints are independent of the local DM density and are thus unchanged.

such as squeezed light are also expected to improve, allowing for ever-increasing noise mitigation [35]. These and other forthcoming technological advances make precision interferometers operating beyond quantum limits indispensable tools for dark matter detection and fundamental physics in general.

3.4 Search for Scalar Field Dark Matter with the Holometer

3.4.1 Introduction

The Fermilab Holometer, which has been constructed to search for exotic quantum space-time correlations [16] (see Sec. 2.2.8), consists of two independent power-recycled Michelson interferometers with 40-metre arms, coaligned and separated by 0.9 m beamsplitter-to-beamsplitter. As the spatial coherence length of light scalar field dark matter ($\lambda_\phi = 2\pi/|\vec{k}_\phi|$ see Eq. 3.2) is much greater than the separation of the interferometers, possible DM signals in the two intstruments would appear in phase at any time. As dominant sources of noise (i.e. photon shot noise) are incoherent between the two systems, we can take a coherent average of the cross-spectrum over time to increase the signal-to-noise ratio for potential DM signals, which then increases with the square root of the total measurement time. Specifically, the coherently averaged cross-spectral sensitivity lies five orders of magnitude below the single-instrument noise floor for the current data set.

3.4.2 Methods

The magnitude of the expected signal due to scalar field dark matter in the cross-spectrum is given by Eq. 3.9, where $C_{\text{disp}} \approx 5 \cdot 10^{-3}$ for the Holometer's fused silica beamsplitter. The fundamental longitudinal vibration mode of the beamsplitter has an angular frequency $\omega_0 = 2\pi \cdot 226$ kHz [16]. The mechanical mounting of the beamsplitter has a very minor effect on this resonance: a basic model of the vibrational modes of a simple cylinder, with dimensions and material matching the beamsplitter, predicts a fundamental planar mode frequency of 225 kHz; i.e. the mount structure causes a frequency shift of less than 0.5%. A detailed description of this effect is reported in section 6.5.1 of [16].

Spectral analysis

We performed our analysis on a 704-hr dataset acquired between July 2015 and February 2016 [18, 147]. During the data taking, the photodetector signals of the two interferometers were sampled at 50 MHz. A high-frequency data acquisition system then performed Fourier transforms, cross-correlation, and averaging of batches of spectra in real time. A detailed description of the Holometer's data acquisition system can be found in section 5.3 of [16]. Unlike the potential DM signal in data from GEO 600, a cross-correlated DM signal as could be found in data from the Holometer would effectively have infinite coherence, removing the advantage of using the modified LPSD

method used for GEO 600. We therefore took a coherent average of the full data set of cross-spectra to yield maximum sensitivity to potential dark matter signals.

Candidate signal search

We searched for significant peaks relative to the background noise in the cross-spectral magnitude. A peak was considered a possible candidate when there was less than 5% probability that it was due to noise. This probability was determined under the assumption that the noise was Rayleigh-distributed and stationary (as the real and imaginary parts of the CSD, taken individually, are Gaussian-distributed and stationary [16]). The median of the local noise distribution of the time-averaged cross-spectrum was estimated at each frequency bin, using a moving average over neighbouring frequency bins. Different values for the number of neighbouring bins in the moving window (N) were used for different frequency regions. The choice of N represents a trade-off between erroneously assuming instrumental spectral artefacts or signals to be features of the underlying noise spectrum versus erroneously assuming features of the underlying noise spectrum to be instrumental spectral artefacts or signals. In other words, N has to be chosen such that the auto-correlation length of the noise spectrum is much greater than N. We used different window sizes N in five frequency regions, i.e. N=500 (840 kHz - 25 MHz), N=250 (650 - 840 kHz), N= 70 (250 - 650 kHz), N=20 (14 - 250 kHz) and N=4 (381 Hz - 14 kHz).

The frequency-dependent noise variance was estimated directly as the sample variance of all DFTs taken over time. The total error σ also includes a calibration error inherent to the apparatus [16]. The look-elsewhere effect was compensated with the application of a trial factor of approximately $\sim 6 \cdot 10^4$ to account for the number of bins in the cross-spectrum. The performed analysis resulted in the identification of two possible candidates above the 95% confidence level, i.e. $> 5.31\sigma$, as shown in Figure 3.7.

These two peaks were then subjected to further analysis to investigate if either was a DM signal. Both the identified relevant peaks in the amplitude spectrum were related to known harmonic sources inherent to the experiment. The first, at ∼13 MHz, is injected for diagnostic monitoring of the readout system by a LED placed directly in front of the photodetectors. The second peak, at $\sim$ 20.5 MHz, is the RF control sideband used to phase lock the lasers to the resonant interferometer cavities [148].

3.4.3 Results

Having ruled out the presence of signals due to scalar field DM, we set new constraints on the DM parameters at the 95% confidence level using Eq. 3.9, applying our analysis to the three different DM scenarios. The electron and photon coupling parameters, Λ_e and Λ_γ, respectively, are constrained for each scenario as a function of the field's mass

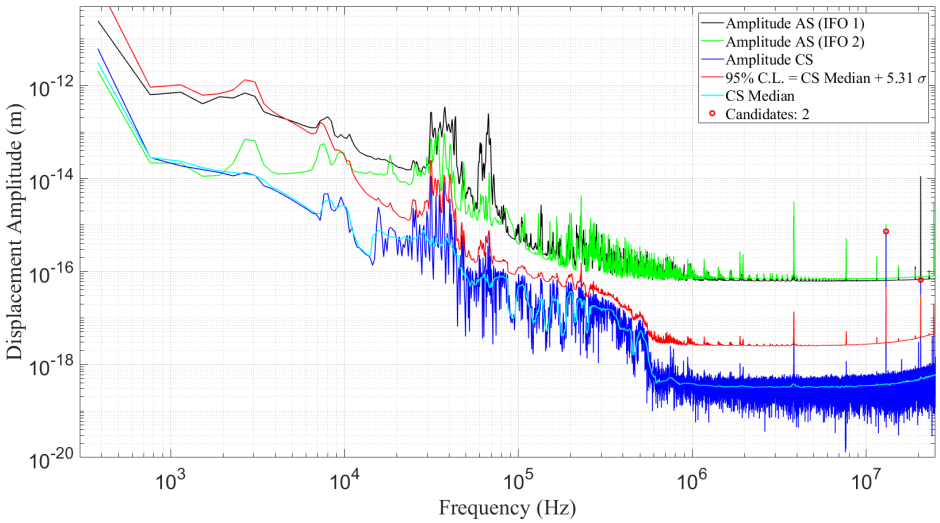

Figure 3.7. The amplitude auto-spectrum of the single interferometers (black and green) and the cross-spectrum magnitude (blue) obtained from the Holometer's coherently averaged data. At frequencies above ≈ 1 MHz the spectrum is dominated by photon shot noise; below ≈ 1 MHz environmental (mechanical) and laser noise dominate [16]. In particular, below 500 kHz the dominant noises are laser amplitude and phase noise - for a detailed description of their characterisation, see sections 6.4.1 and 6.4.2 of [16]. For each frequency bin, the local noise median (cyan) was estimated from its neighbouring bins. The 95% confidence level (red) was then computed assuming the noise to be Rayleigh distributed. Peaks (red) above the 95% confidence level were considered possible DM candidates and were investigated further.

m_ϕ, assuming for each coupling parameter the other to be zero. The new constraints obtained from our analysis, together with previously published upper limits, are plotted in Figs. 3.8 and 3.9. The feature at 226 kHz is due to the mechanical resonance of the beamsplitter, where the apparent depth of the minimum is limited by the frequency resolution (the Q-factor of the beamsplitter is more than an order of magnitude greater than the plotted amplitude enhancement).

3.4.4 Conclusions

In this work we have looked for signals of scalar field DM in the cross-spectrum of co-located interferometers, which constitutes the first direct search of scalar DM using correlated interferometry. Our analysis excluded the presence of scalar field DM signals in the data, placing lower limits on the DM coupling parameters for DM masses between $1.6{\cdot}10^{-12}$ eV and $1.0{\cdot}10^{-7}$ eV. These limits improve over previous direct experimental bounds in several subranges: we set limits in the previously unconstrained mass range

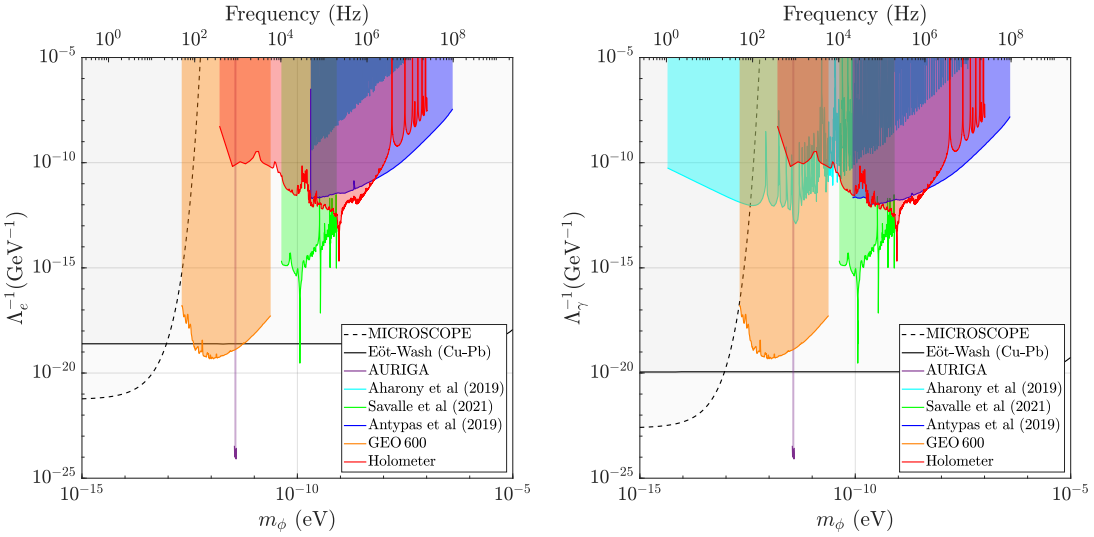

Figure 3.8. Computed constraints on the coupling parameters Λ_e (left) and Λ_γ (right) as a function of the field's mass m_ϕ for scalar field DM as in the *Basic Scalar* scenario. Electron and photon coupling constraints are at the 95% confidence level. The region coloured in red indicates the parameter space for the coupling parameters excluded by our analysis of the Holometer data. Other coloured regions mark the parameter space excluded by other direct searches [137–139], including the AURIGA experiment [140] and the GEO 600 interferometer [2]. The grey regions denoted by the black curves are constraints on general fifth-forces and tests of the equivalence principle [144]. These come from the space-based MICROSCOPE experiment [143], and the Cu/Pb and the Be/Ti torsion pendulum experiments performed by the Eöt-Wash group [116, 141, 142]. For the *Relaxion Halo* scenario, a mass-dependent DM halo density as described in [115] has been assumed. The constraints obtained for this scenario from direct experimental searches have been obtained by rescaling the original ones to account for this dependence. Constraints from fifth-force and equivalence principle tests do not depend on the local DM density and are thus the same as in the *Dilaton/Modulus* scenario.

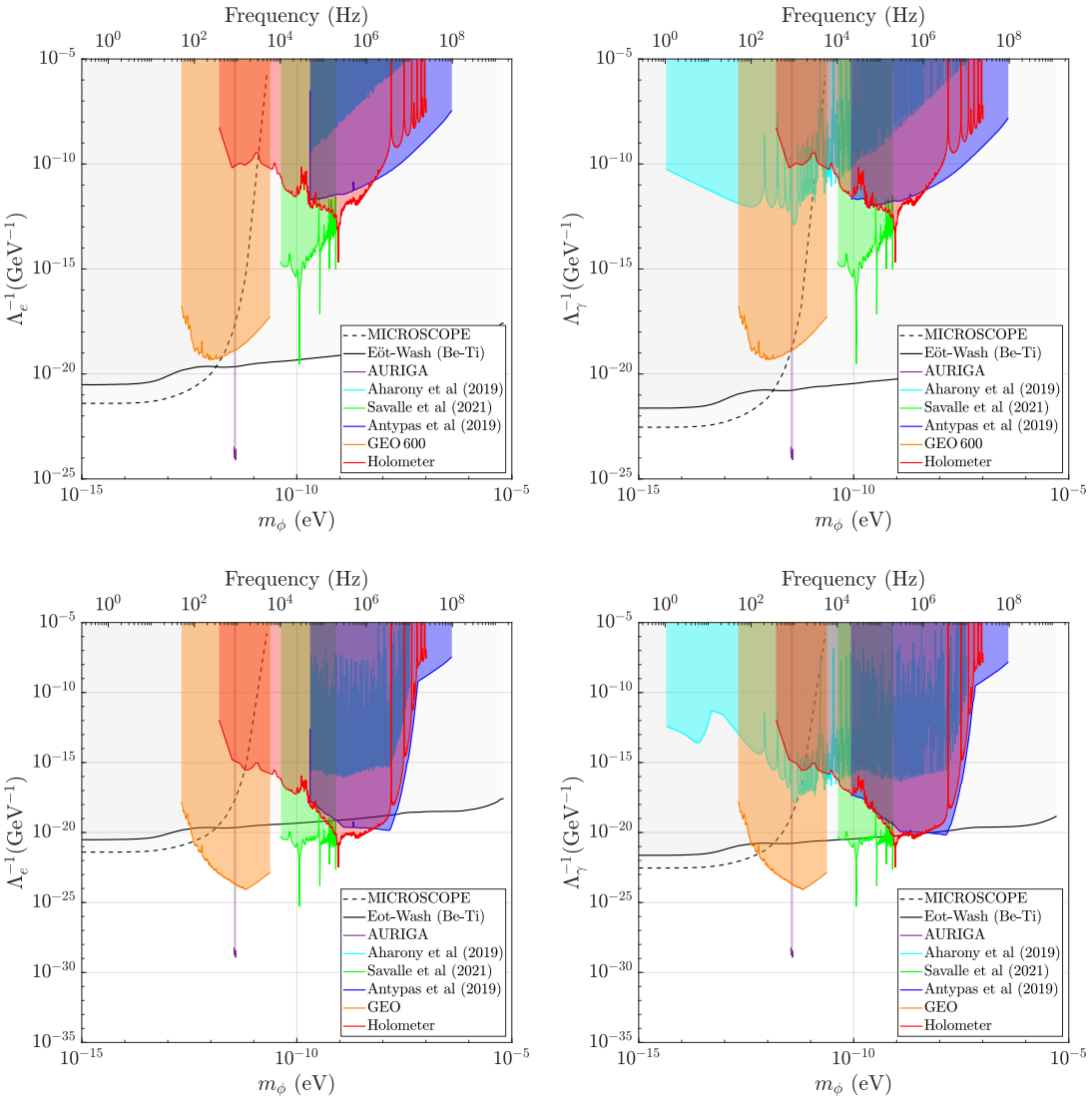

Figure 3.9. Computed constraints on the coupling parameters Λ_e (left) and Λ_γ (right) as a function of the field's mass m_ϕ for scalar field DM as in the *Basic Scalar* scenario (top), the *Dilaton/Modulus* scenario (top) and the *Relaxion Halo* scenario bottom). See caption of Fig. 3.8.

between $2.4 \cdot 10^{-11}$ and $4.3 \cdot 10^{-11}$ eV, and improve over the existing constraints [138] in the mass range $8.2 \cdot 10^{-9} - 6.2 \cdot 10^{-8}$ eV by up to three orders of magnitude.

Better constraints on scalar field DM can be achieved through upgrades of current experiments [138], by increasing the measurement time of correlated instruments, or from new, more sensitive experiments (e.g. [2]).

3.5 Polarimetry Experiments to Search for Scalar and Pseudoscalar DM

3.5.1 Introduction

In this section, we present a new way to use high-sensitivity polarimetry to identify potential couplings of scalar field DM and axion-like particles. In 1979, E. Iacopini and E. Zavattini published seminal work outlining how to detect vacuum magnetic birefringence [149, 150] with polarimetry [151]. Unlike Michelson interferometry, which looks for the relative phase difference between light in two orthogonal arms, polarimetry is sensitive to the relative phase variation of two orthogonal polarisation components. Polarimetry is still being used for measuring minute amounts of birefringence [152], and it provides the highest sensitivity for measuring the vacuum magnetic birefringence [153].

In the polarimetry setup proposed here, an oscillating scalar or pseudoscalar DM field is expected to produce a relative phase modulation between the two orthogonal polarisations at the same frequency as the DM field oscillation, which could be detected. Low-mass bosonic dark matter is assumed to have a long coherence length (relative to the measurement apparatus' dimensions), such that two identical polarimeters close together would measure the same signal and may be cross-correlated in a search for these dark-matter fields, in much the same way as done with two Michelson interferometers before (as detailed in Sec. 3.4).

3.5.2 Coupling of Scalar Field DM to a Polarimeter

We first show through an analytical calculation how thickness variations of a birefringent optical element, induced by scalar field DM, would produce a measurable phase difference between orthogonal polarisation components of laser light in a polarimeter.

The size and refractive properties of solids depend on the fine structure constant and the electron mass (see Sec. 3.2). We consider the effect of scalar field DM on the optical parameter

$$\beta = \frac{2\pi d \Delta n}{\lambda}, \tag{3.19}$$

which is the difference in the accumulated phase between orthogonal polarisations in radians, where d is the path length inside the solid, $\Delta n = n_e - n_o$ is the intrinsic birefringence of the solid (i.e. the difference of the refractive indices for the two orthogonal polarisations) and λ is the wavelength of light. As described in Sec. 3.2, scalar field dark matter would induce variations of the size and index of refraction of a solid, which would in turn produce changes in the parameter β. Relative changes in β are the sum of

relative changes in d and Δn

$$\frac{\delta\beta}{\beta} = \frac{\delta d}{d} + \frac{\delta\Delta n}{\Delta n}, \tag{3.20}$$

to first order. The DM-induced changes in the thickness of the solid can be described by substituting $l \to d$ in Eq. 3.6. The DM-induced changes in the birefringence of the solid $\delta\Delta n$ can be found using Eq. 3.7, which gives

$$\frac{\delta\Delta n}{n} \approx C_{\rm disp}\left(2\frac{\delta\alpha}{\alpha} + \frac{\delta m_e}{m_e}\right). \tag{3.21}$$

We thus expect that in the presence of an oscillating scalar field ϕ (Eq. 3.2), there will be oscillatory changes of the parameter β:

$$\frac{\delta\beta}{\beta} = \phi_0 \cos\left(\omega_\phi t - \vec{k}_\phi \cdot \vec{r}\right)\left[\left(\frac{1}{\Lambda_\gamma} + \frac{1}{\Lambda_e}\right)\left(\left|1 - \frac{\omega_\phi^2}{\omega_0^2}\right|\right)^{-1} + C_{\rm disp}\left(\frac{1}{\Lambda_e} + \frac{2}{\Lambda_\gamma}\right)\right]. \tag{3.22}$$

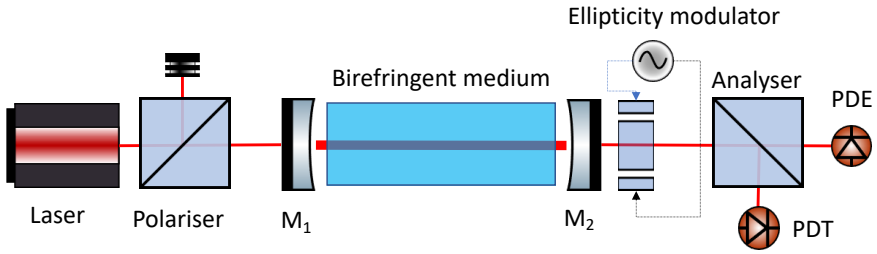

Figure 3.10. The proposed polarimetry experiment for searching for scalar field dark matter, which uses a birefringent medium in a Fabry-Pérot cavity. M_1/M_2 are mirrors that delimit the Fabry-Pérot cavity, and PDT, PDE are the photodiodes in the transmission and in the extinction port of the analyser, respectively.

We consider a polarimeter configured as in Fig. 3.10. To find the effect of the changes $\delta\beta/\beta$ in the birefringent medium on the optical output of the polarimeter, we use the Jones matrix formalism. After passing through a polariser, the input laser light will be in the following state:

$$\mathcal{E} = E_0\, e^{-i(kz-\omega t)} \cdot \begin{pmatrix} 1 \\ 0 \end{pmatrix}, \tag{3.23}$$

where E_0 is the electric field's initial magnitude. The Jones matrix of a birefringent solid with an optic axis oriented at an angle ϕ relative to the input polarisation is:

$$\mathbf{B}(\beta,\phi) = \mathbf{O}(\phi) \cdot \begin{pmatrix} e^{\frac{1}{2}i\beta} & 0 \\ 0 & e^{-\frac{1}{2}i\beta} \end{pmatrix} \cdot \mathbf{O}(-\phi), \tag{3.24}$$

where $\mathbf{O}(\phi)$ is the rotation matrix:

$$\mathbf{O}(\phi) = \begin{pmatrix} \cos(\phi) & -\sin(\phi) \\ \sin(\phi) & \cos(\phi) \end{pmatrix}. \tag{3.25}$$

The experiment is configured such that the optic axis of the birefringent solid is oriented at an angle of $\phi = \pi/4$. The total phase difference between polarisation components induced by the solid is $\beta = n\pi + \delta\beta,\ n \in \mathbb{Z}$, where $\delta\beta \ll 1$ represents the phase modulation due to DM-induced solid thickness and refractive index variation. A photoelastic modulator (PEM) and an analyser are represented by the Jones matrices $\mathbf{H}$ and $\mathbf{A}$, respectively,

$$\mathbf{H} = \begin{pmatrix} 1 & i\eta \\ i\eta & 1 \end{pmatrix}, \quad \mathbf{A} = \begin{pmatrix} 1 & 0 \\ 0 & 1 \end{pmatrix}. \tag{3.26}$$

We compute the output electric field after multiple reflections in the Fabry-Pérot cavity as follows:

$$\begin{aligned} \mathbf{E}_{\text{out}} &= \begin{pmatrix} E_{\text{out},0} \\ E_{\text{out},\perp} \end{pmatrix} \\ &= Te^{\frac{i\varphi}{2}} \sum_{n=0}^{\infty} \left[Re^{i\varphi}\, \mathbf{B}^2(\beta, \frac{\pi}{4}) \right]^n \cdot\ \mathbf{B}(\beta, \frac{\pi}{4}) \cdot \mathcal{E} \\ &= Te^{\frac{i\varphi}{2}} \left[\mathbf{I} - Re^{i\varphi}\, \mathbf{B}^2(\beta, \frac{\pi}{4}) \right]^{-1} \cdot\ \mathbf{B}(\beta, \frac{\pi}{4}) \cdot \mathcal{E}, \end{aligned} \tag{3.27}$$

where φ is the round-trip phase shift of light propagating between the two-cavity mirrors, R is the reflectance of the mirrors, T is the transmittance of the mirrors, and $\mathbf{I}$ represents the identity matrix.

We then use the heterodyne method to read out the polarimetric signal in the output field of the polarimeter, which involves placing a photoelastic modulator (PEM) next to an analyser oriented at 45° with respect to the input polarisation (see Fig. 3.10). The electric field at the extinguished port of the analyser is:

$$\mathbf{E}_{\text{ext}} = \mathbf{A} \cdot \mathbf{H} \cdot \mathbf{E}_{\text{out}}. \tag{3.28}$$

The extuinguished intensity $I_{\text{ext}} = |\mathbf{E}_{\text{ext}}|^2$, normalised by the intensity of the input light I_0, is

$$\frac{I^{\text{ext}}}{I_0} = \frac{T^2}{1 - 2R\cos\varphi + R^2} \left(\sigma^2 + \eta^2 + \eta\ \delta\beta \frac{(1 - R^2)}{1 - 2R\cos\varphi + R^2} + \mathcal{O}\left[(\delta\beta)^2 \right] \right), \tag{3.29}$$

where $\delta\beta$ represents the phase difference due to the birefringent solid thickness and refractive index variations, $\eta(t) = \eta_0 \cos(2\pi\nu_{\text{PEM}} t)$ describes the modulation imparted

by the PEM, and σ^2 is the extinction ratio of the crossed polarisers. The term linear in $\eta(t)$ is the heterodyne signal, which is used to detect the effect of interest. Furthermore, we must consider that the Fabry-Pérot cavity operates as a low-pass first-order filter for a time-dependent signal such as the one induced by scalar field DM. Specifically, the transfer function of a Fabry-Pérot cavity for a time-dependent ellipticity signal is [154]

$$h_{\mathrm{T}}(\nu) = \frac{T}{\sqrt{1+R^2-2R\cos 2\pi\nu\tau}}, \quad \phi_{\mathrm{T}}(\nu) = \arctan\left[\frac{R\sin 2\pi\nu\tau}{1-R\cos 2\pi\nu\tau}\right], \tag{3.30}$$

where ν is the frequency of the signal, $\tau = 2/c\int_0^L ndL$ is one round-trip time in the cavity, and n, L, and c are the refractive index, the length of the cavity, and the speed of light, respectively.

The input laser light should be kept resonant in the Fabry-Pérot cavity, such that $\varphi = 0$, using e.g. the Pound-Drever-Hall method. The signal from the photodiode at the extinguished port can be demodulated at the frequency ν_{PEM}, and the RMS magnitude of the phase shift $|\delta\beta|$ can then be inferred:

$$|\delta\beta(\nu)| = \frac{\mathcal{I}^{\mathrm{ext}}(\nu)}{NI_0\eta_0 h_{\mathrm{T}}(\nu)}, \tag{3.31}$$

where $N = 2/(1-R)$ is the cavity buildup and $\mathcal{I}^{\mathrm{ext}}$ is the demodulated signal of the extinguished intensity at frequency ν_{PEM}.

3.5.3 Coupling of Pseudoscalar DM to a Polarimeter

We now consider the case of pseudoscalar axion-like DM, which produces a rotation of the polarisation of light according to Eq. 3.14. We derive below how a pseudoscalar field may produce an observable signal in a polarimeter as configured in Fig. 3.11.

Figure 3.11. The proposed polarimetry experiment for searching for axion-like pseudoscalar fields, which uses a Fabry-Pérot cavity and two quarter-wave plates (QWP_1 and QWP_2). PDT, PDE are the photodiodes in the transmission and in the extinction port of the analyser, respectively, and $\mathrm{M}_1/\mathrm{M}_2$ are mirrors that delimit the Fabry-Pérot cavity.

The Jones matrix (on a linear basis) for the propagation of light that parameterises the rotation of its plane of polarisation in the presence of an axion-like field is given by

$$\mathbf{A}_\gamma(t,\tau) \approx \begin{pmatrix} 1 & -\rho(t,\tau)/2 \\ \rho(t,\tau)/2 & 1 \end{pmatrix}, \tag{3.32}$$

for angles $\rho \ll 1$.

We first consider a setup where polarized laser light is injected into an empty Fabry-Pérot cavity, without any optical elements inside. The rotation of the plane of polarisation of the light inside the cavity due to an axion-like field is

$$\begin{aligned} \mathbf{E}_{\text{out}} &= \sum_{n=0}^{\infty} \left[e^{i\varphi} \left(\mathbf{A}_\gamma(\rho) \cdot \mathbf{M} \right)^2 \right]^n \cdot T e^{i\varphi/2} \, \mathbf{A}_\gamma(\rho) \cdot \mathcal{E} \\ &= \frac{T e^{i\varphi/2}}{(1 - R e^{i\varphi})} \, \mathbf{A}_\gamma(\rho) \cdot \mathcal{E}, \end{aligned} \tag{3.33}$$

to first order, where $\mathbf{M} = \begin{pmatrix} -r & 0 \\ 0 & r \end{pmatrix}$ is the Jones matrix representing the reflection of a mirror for normal incidence and φ is the round-trip phase shift. Note that over a round trip the element $(\mathbf{A}_\gamma(t,\tau) \cdot \mathbf{M})^2 = R\,\mathbf{I}$, where $R = r^2$ is the reflectance of the mirror and $\mathbf{I}$ is the identity matrix. Therefore, when the light is resonant with the cavity, the DM-induced polarisation rotation, also known as dichroism, cancels out over round trips.

To counteract this cancellation effect, two quarter-wave plates (QWPs) can be placed next to the mirrors at either end of the cavity, as shown in Fig. 3.11. This is similar to the approaches in [124, 126]. In this configuration, the polarisation rotation due to the axion-like field will accumulate over multiple round trips. A quarter-wave plate with its fast axis aligned with the incident polarisation is represented by the matrix $\mathbf{Q} = \mathbf{B}(\pi/2, 0)$. The quarter-wave plate converts any rotation of the polarisation of the light to ellipticity:

$$\mathbf{Q} \cdot \mathbf{A}_\gamma \cdot \mathbf{Q} \cdot \mathcal{E} = \tilde{E}_0 \begin{pmatrix} 1 \\ -\frac{i\rho}{2} \end{pmatrix}, \tag{3.34}$$

where $\tilde{E}_0 = E_0 e^{-i\zeta}$ is the amplitude of the electric field with an overall phase ζ. The electric field at the exit of the Fabry-Pérot cavity including the QWPs is:

$$\begin{aligned} \mathbf{E}_{\text{out}} &= T e^{\frac{i\varphi}{2}} \sum_{n=0}^{\infty} \left[e^{i\varphi} \, \left(\mathbf{Q} \cdot \mathbf{A}_\gamma(\rho) \cdot \mathbf{Q} \cdot \mathbf{M} \right)^2 \right]^n \cdot \, \mathbf{Q} \cdot \mathbf{A}_\gamma(\rho) \cdot \mathbf{Q} \cdot \mathcal{E} \\ &= T e^{\frac{i\varphi}{2}} \left[\mathbf{I} - e^{i\varphi} \, \left(\mathbf{Q} \cdot \mathbf{A}_\gamma(\rho) \cdot \mathbf{Q} \cdot \mathbf{M} \right)^2 \right]^{-1} \cdot \mathbf{Q} \cdot \mathbf{A}_\gamma(\rho) \cdot \mathbf{Q} \cdot \mathcal{E} \end{aligned} \tag{3.35}$$

Using heterodyne readout, the intensity of the output light at the extinguished port (relative to the input intensity) is

$$\frac{I^{\text{ext}}}{I_0}(\rho) \approx \sigma^2 + \eta^2 - 2N\eta\frac{\rho}{2} + O\left[\rho^2\right]. \tag{3.36}$$

When the frequency response of the Fabry-Pérot cavity (see Eq. 3.30) is taken into consideration, the RMS magnitude of the pseudoscalar-induced phase shift can be inferred as

$$|\rho(\nu)| = \frac{\mathcal{I}^{\text{ext}}(\nu)}{Nh_{\text{T}}(\nu)I_0\eta_0}. \tag{3.37}$$

This expression shows that with the addition of the two quarter-wave plates, the phase shift between orthogonal polarisations induced by an axion-like field builds over multiple cavity trips N. The approach presented here shares similarities with the method described in Nagano et al. [125] for detecting axion dark matter using interferometric gravitational wave detectors. However, our method differs in the use of quarter-wave plates to accumulate the rotation induced by axion-like pseudoscalar dark matter over multiple round trips and subsequently convert it into ellipticity for detection through polarimetry [124].

Eqs. 3.31 and 3.37 show that a polarimeter can be used for a direct search for both scalar and pseudoscalar dark matter, by configuring the device either as in Fig. 3.10 or as in Fig. 3.11, respectively.

3.5.4 Noise budget

We carried out an inventory of expected noises that can limit the performance of the proposed polarimetry experiments. Specifically we considered photon shot noise, seismic (environmental) noise, relative laser intensity noise (RIN), and electronic noise. These noises produce fluctuations in the (demodulated) extinguished intensity $\mathcal{I}_{\text{ext}}$ with an RMS variation amplitude $S_{\mathcal{I}^{\text{ext}}}$. Such intensity fluctuations are equivalent to polarimetric phase noise with RMS amplitude

$$S_{\text{P}} = \frac{S_{\mathcal{I}^{\text{ext}}}}{I_0\eta_0}. \tag{3.38}$$

which determines the sensitivity of the experiment, as DM signals manifest as the polarimetric phase variations given in Eqs. 3.31, 3.37. The different noises add together in quadrature to yield an equivalent total phase RMS amplitude

$$S_{\text{P}}^{(\text{tot})} \approx \sqrt{{S_{\text{P}}^{(\text{shot})}}^2 + {S_{\text{P}}^{(\text{seismic})}}^2 + {S_{\text{P}}^{(\text{RIN})}}^2 + {S_{\text{P}}^{(\text{elec})}}^2}. \tag{3.39}$$

Given a set of proposed operating parameters (see Table 3.1), the shot noise in terms of polarimetric phase is estimated to be $S_{\mathrm{P}}^{(\mathrm{shot})} \approx 6 \times 10^{-10}$ rad/$\sqrt{\mathrm{Hz}}$ [4], corresponding to shot noise levels encountered in existing polarimeters [153]. We estimate that this shot noise level will be at least an order of magnitude above the contributions from RIN and electronic noise at all frequencies of interest [4].

Input power	I_0	1 W
Extinction ratio	σ^2	2×10^{-7}
Modulation amplitude	η_0	1.5×10^{-3}
Modulation frequency	ν_{PEM}	50 kHz
Seismic noise coupling	γ	0.1
Cavity build-up	N	20 000
Solid/QWP wedge	θ	1 μrad
Yttrium vanadate	C_{disp}	12×10^{-3}
Sapphire	C_{disp}	6.6×10^{-3}

Table 3.1. Relevant characteristics of the proposed polarimetry setups

Seismic noise

Seismic noise will be significant in the polarimeter configuration for detecting scalar field DM (Fig. 3.10) if the back and front surfaces of the birefringent crystal are not parallel and the point of incidence of the laser beam on the solid varies. In this situation, the laser light will traverse a time-varying distance through the solid, thereby generating unwanted polarisation phase noise. If the optical components of the polarimeter are installed on a perfectly rigid platform, the seismic disturbance should have no effect on their relative position, and the point of incidence of the laser light on the solid will be constant. Nevertheless, the coherence length of seismic noise above 1.5 Hz can be as little as $1 - 16$ m [155], which would mean the cavity mirrors experience a differential displacement. To estimate the coupling of seismic noise into the polarimeter, we consider our birefringent solid to have uniform birefringence and a small wedge, θ. We assume the solid's transverse position relative to the incidence of the laser beam is randomly modulated by seismic noise with displacement amplitude spectral density δr. Further, we assume that the seismic noise is broadband and has the same magnitude in all directions. The coupling of the seismic noise to birefringence noise in the polarimeter can then be calculated using the wedge angle θ as follows:

$$S_{\mathrm{P}}^{(\mathrm{seismic})} = 2\pi \frac{N\,\delta r\,\theta}{\lambda}\,\Delta n\,[1 - \gamma(L, f)] \tag{3.40}$$

Here, Δn is the birefringence of the solid, N is the cavity build-up, and the coupling parameter $\gamma(L, f)$ represents the two-point correlation of the seismic noise between the laser and the solid, which are separated by a distance L, as a function of frequency. The expected displacement amplitude noise spectral density due to seismic noise is estimated from data taken at the advanced Laser Interferometer Gravitational-Wave Observatory (aLIGO) [156, 157]. We use measurements of the seismic displacement noise as mitigated through a two-stage seismic isolation platform and a single silica pendulum suspension, which is only part of the multi-stage seismic isolation and suspension system used at LIGO. Similar seismic isolation can be employed for the proposed polarimetry setup.

In Fig. 3.12 we show the projected total phase noise $S_{\rm P}^{(\rm tot)}$. It can be seen that the shot noise is expected to be the dominant contribution to the total noise at high frequencies; at lower frequencies, it is expected that seismic noise will be dominant. The other noise contributions are estimated have a relative contribution to the total noise of $\lesssim 10\%$ [4].

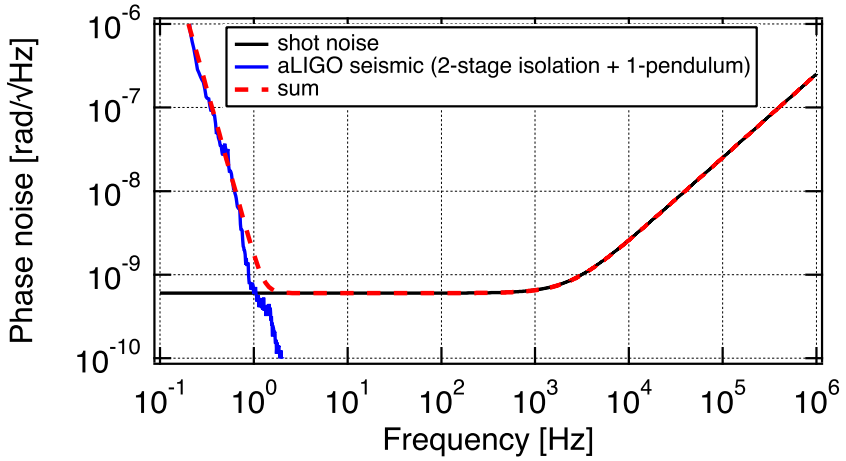

Figure 3.12. A projection of phase noise expected in the proposed polarimetry experiment is shown. The total expected noise is expected to be dominated by shot noise and seismic noise. For calculating the curves in this plot, we used Eq. 3.40, and the parameters in Table 3.1. The seismic phase noise amplitude plotted in blue corresponds to the noise as mitigated through a two-stage seismic isolation platform and a single silica pendulum suspension, which is part of the seismic isolation and suspension system used at the advanced Laser Interferometer Gravitational-Wave Observatory (aLIGO) [156, 157].

3.5.5 Prospects for DM searches

Scalar field DM

In the proposed polarimeter setup for detecting scalar field DM, the sensitivity is defined by the observable relative phase variations $\delta\beta(\nu)/\beta$ at frequency ν. From the noise budget above, we find that the condition where the shot noise readout phase is the dominant noise, i.e. $\delta\beta_{\text{noise}} = S_{\text{P}}^{(\text{tot})} \approx 6 \times 10^{-10}\ /\sqrt{\text{Hz}}$ can be achieved. The sensitivity to scalar field DM can be improved by increasing $\beta = 2\pi d\Delta n/\lambda$, where the effective path length in the solid in a Fabry-Pérot cavity $d = d_0 N$, i.e. the product of the solid thickness d_0 and the average number of round trips in the cavity N. We assume that absorption is the main loss, limiting the number of round trips, i.e. $P \gg T$, which would be the case for this experiment. The total losses in the cavity P will likely be dominated by those due to imperfections in the AR coating P_{AR} and the solid's bulk absorption loss $P = P_{\text{AR}} + \mu d$ (where μ is the linear absorption coefficient of the bulk). We evaluate the frequency response of the polarimeter given these conditions:

$$Nh_{\text{T}} = \frac{2}{(T+P)\sqrt{1 + \frac{4}{(T+P)^2}\sin^2\pi\nu\tau}} \approx \frac{2}{\sqrt{P^2 + 4\sin^2\pi\nu\tau}}. \tag{3.41}$$

The sensitivity to scalar field DM can be defined by a signal-to-noise ratio (SNR) equal to one, which means the magnitude of the signal of interest as observed in the extinguished intensity is equal to the magnitude of the noise-induced fluctuations in the extuinguished intensity:

$$\mathcal{I}^{\text{ext}}(\nu) = S_{\mathcal{I}^{\text{ext}}}(\nu), \tag{3.42}$$

or

$$S_{\text{P}}^{\text{tot}}(\nu) = Nh_T\delta\beta(\nu), \tag{3.43}$$

which gives,

$$\frac{\delta\beta(\nu)}{\beta} = \frac{S_{\text{P}}^{(\text{tot})}\lambda\sqrt{P^2 + 4\sin^2\pi\nu\tau}}{2\pi d\Delta n}. \tag{3.44}$$

This shows that the sensitivity depends on the performance of the polarimeter, parameterised by $S_{\text{P}}^{(\text{tot})}$, the properties of the solid, and the frequency response of the cavity. Specifically, the sensitivity scales linearly with the differential optical path length $d\Delta n$ and the total absorption caused by the solid P.

As a consequence of this, if coating loss is the dominant effect, the sensitivity will increase linearly with both the intrinsic birefringence of the solid and its thickness. If,

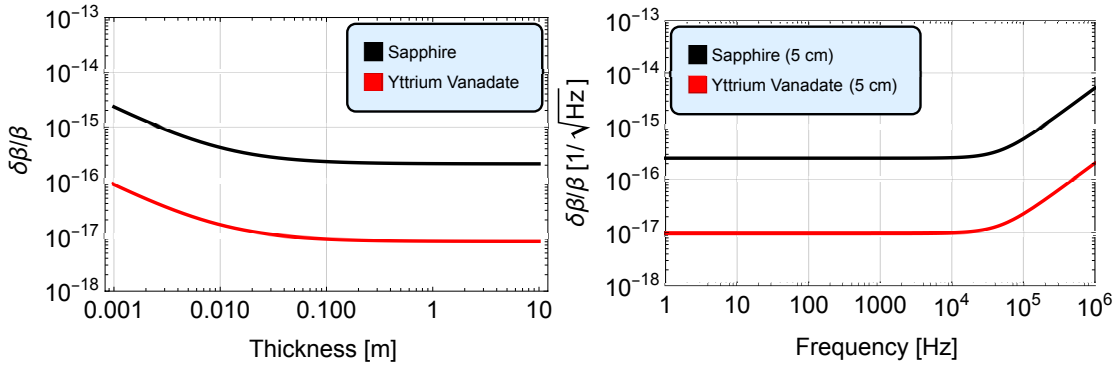

Figure 3.13. Left: sensitivity of the polarimeter (Eq. 3.44) as a function of the crystal thickness for sapphire ($\Delta n = 0.008$) and pure yttrium vanadate ($\Delta n = 0.208$) with absorption of $P = 100$ ppm/cm. **Right:** sensitivity of the polarimeter (Eq. 3.44) using yttrium vanadate (YVO4) or sapphire crystals as a function of frequency for a $d = 5$-cm-thick crystal.

on the other hand, the bulk absorption contributes the majority of the total loss, the sensitivity will not improve with increased thickness. Therefore, the cross-over point between sensitivity gain due to increased thickness and sensitivity loss due to bulk absorption will be the most important consideration when choosing the optimal solid thickness. Fig. 3.13 shows the expected $\delta\beta/\beta$ sensitivity as a function of crystal thickness and frequency for two types of birefringent crystals: sapphire ($\Delta n = 0.008$) and pure yttrium vanadate ($\Delta n = 0.208$) crystals. These calculations were made using a linear bulk absorption coefficient of 100 ppm/cm [158], and an AR coating loss of 25 ppm per incidence. We have used a Fabry-Pérot cavity length of 30 cm and a thickness of 5 cm for the birefringent solid. Because bulk absorption increases linearly with crystal thickness, a crystal thicker than 5 cm would not yield a meaningful improvement.

Absorption of light in the birefringent solid will heat up the material. This could produce thermal lensing and thermo-elastic deformation, which could produce additional noise at the extinguished port of the output analyser and limit the resonant cavity build-up. It was estimated that these thermal effects could be compensated for in the experiment by using a specialised thermal actuator, such as a CO2 laser projector or ring heater [4, 159].

Given the expected sensitivity in terms of $\delta\beta/\beta$, we use Eq. 3.22 to estimate the sensitivity of the proposed experiment in terms of the DM coupling constants $\Lambda_\gamma, \Lambda_e$, which are shown in Fig. 3.14. These projections were made for a setup that uses a 5-cm-thick yttrium vanadate crystal. The black dashed lines represent the sensitivity that would be attained after measuring for a time equal to the coherence time of the DM, while the red dashed lines represent the sensitivty for cross-spectral integration

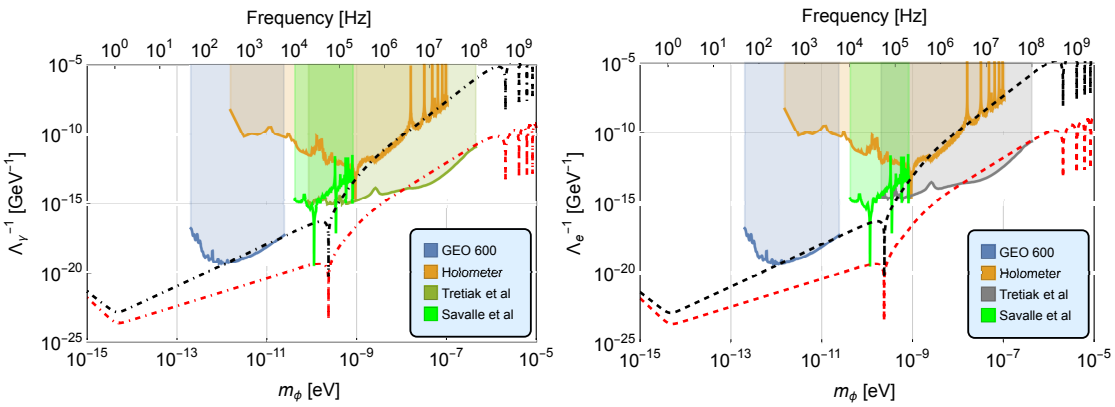

Figure 3.14. Prospects for sensitivity to scalar field dark matter using polarimetry with a 30-centimeter-long Fabry-Pérot cavity and a 5-centimeter-thick yttrium vanadate birefringent crystal are shown; the lines give the upper sensitivity in terms of the electron coupling constant (left) and photon coupling constant (right), as a function of scalar field mass. The black dashed/dotted-dashed lines represent the integrated sensitivity over the coherence time of dark matter, while the red dashed/dotted-dashed lines represent one year of integration using twin polarimetry and cross-correlation. Existing constraints from other interferometry experiments [2, 3, 139, 160] are also shown.

using twin cross-correlated polarimeters for a total of one year. Existing constraints from other interferometry experiments [2, 3, 139, 160] are shown for comparison.

Pseudoscalar DM

To calculate the sensitivity to pseudoscalar DM, we must estimate the sensitivity of a polarimeter configured as in Fig. 3.11, including two thin quarter-wave plates inside the Fabry-Pérot cavity. Following a similar argument as for scalar DM, we find that the DM-induced polarisation rotation angle we can expect to observe with a signal-to-noise ratio equal to one is

$$|\rho(\nu)| = \frac{S_{\mathrm{P}}^{(\mathrm{tot})}}{N h_{\mathrm{T}}(\nu)} \tag{3.45}$$

$$\approx S_{\mathrm{P}}^{(\mathrm{tot})} \frac{\sqrt{P_{\mathrm{AR}}^2 + 4\sin^2 \pi\nu\tau}}{2} \tag{3.46}$$

where we have made the approximation that the total losses are dominated by the losses in the AR coatings of the quarter-wave plates P_{AR}.[2] Any thermal effects due to the

[2] A quarter wave plate, constructed as a zero-order wave plate (where the relative phase retardation is $\pi/2$ rather than an integer multiple thereof) can be very thin, so bulk absorption can be assumed to be less than 10 ppm. Thus, the losses caused by the AR coating of the two wave plates will be the most

small absorption in the wave plates could be easily compensated for using a thermal actuator [4].

Using Using Eq. 3.14, we can compute the projected sensitivity in terms of the DM coupling constant $g_{a\gamma}$:

$$g_{a\gamma} = \frac{S_{\rm P}^{(\rm tot)}}{2\tau}\sqrt{\frac{P_{\rm AR}^2 + 4\sin^2(\pi\omega_a\tau)}{2\rho_{\rm local}}}, \tag{3.47}$$

where τ is the cavity round-trip travel time. Fig. 3.15 shows the sensitivity for a polarimeter configured as in Fig. 3.11 for two scenarios: the black solid line shows the sensitivity for an integration time up to the coherence time of the axion-like field ($t_{\rm int} = 10^6/\omega_{\rm a}$), and the red dashed line shows the senstivity given two co-located identical polarimeters with a one-year cross-correlation time. For these estimates, we assumed a 5-meter cavity length. Existing constraints from the solar CERN Axion Solar Telescope (CAST) [161], the design sensitivity for Any Light Particle Search (ALPS II) [162], and an interferometric experiment being built in Birmingham [126] are shown for comparison.

3.5.6 Conclusion

In this section we proposed the use of polarimetry for direct searches for low-mass axion-like pseudoscalar and scalar dark matter. The experimental design outlined in this work represents, to our knowledge, the first table-top experiment that can be used to search for both scalar and pseudoscalar DM, with minimal reconfiguration.

We showed that scalar field DM interacting with a highly birefringent crystal (yttrium vanadate or sapphire) drives thickness and refractive index variation of the crystal at the frequency of the scalar field. This, in turn, produces differential phase oscillations between orthogonal polarisation components of light traversing the crystal. If the birefringent crystal is placed in a Fabry-Pérot cavity, these differential phase oscillations between polarisation components can be measured with a polarimeter at high sensitivity using a heterodyne readout technique. The amplification of the signal by the Fabry-Pérot cavity is limited by absorption in the birefringent crystal. Regardless, with a 5 cm-thick birefringent yttrium vanadate crystal, a polarimeter could probe a large region of the scalar field DM parameter space, with DM masses ranging from $(10^{-15} - 10^{-9})$ eV and frequencies of 1 Hz to 200 kHz, beyond existing constraints [2, 3, 160]. As the sensitivity scales linearly with the solid bulk absorption, potential technological advances that allow

significant effect. With 25 ppm loss per surface, two quarter-wave plates will cause a total of 100 ppm loss per light crossing. Given that the losses far exceed the mirrors' transmittance, e.g. $P \gg T$, the losses that occur in the cavity are $P = P_{\rm AR} + \mu d \approx P_{\rm AR}$

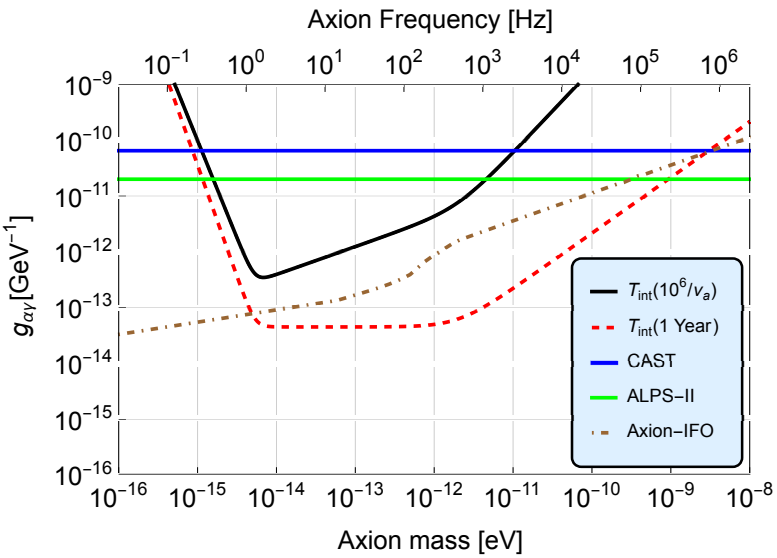

Figure 3.15. Sensitivity of the proposed experiment to the axion-photon coupling coefficient for time integration up to the ALPs coherence time (black solid curve) and using twin polarimeters with a one-year integration time (red dashed curve). We evaluated the sensitivity of the proposed polarimetry experiment with two quarter-wave plates near the mirrors of a 5-meter-long cavity, with 20 kW circulating power and limited by shot-noise. For comparison, the existing constraints from CAST [161] (blue line) and the design sensitivity for ALPS II [162] (green line) and the interferometric detector being built in Birmingham [126] (dotted dashed line) are shown.

the production of purer crystals with less absorption could significantly improve the sensitivity of the proposed polarimetry method.

The same polarimetry setup, reconfigured with two quarter-wave plates placed near the mirrors instead of a thick birefringent solid, could be used to search for axion-like particles with masses ranging from $(10^{-15} - 10^{-8})$ eV and frequencies ranging from 1 Hz to 2.5 MHz. Such axion-like particles may be present in a galactic DM halo; if so, they will manifest themselves by annihilating and producing photons in a polarimeter. This would result in a phase oscillation between the orthogonal polarisations of light. For the axion-like field, the sensitivity will be limited by the AR coating of the QWPs, which will limit the amplification factor of the Fabry-Pérot cavity. A 5-m-cavity polarimeter has the potential to surpass the sensitivity of CAST [161] in the ALPs mass range of 10^{-15} eV all the way up to 10^{-9} eV. The sensitivity can be improved by using a longer cavity. This would improve the signal-to-noise ratio at low frequencies but would limit the sensitive bandwidth, thus decreasing the sensitivity to high axion masses.

3.6 Prospects for Dark Matter Searches with QUEST

The QUEST experiment could be used to search for light scalar field dark matter analogous to how the Fermilab Holometer was used to search for scalar field dark matter (Sec. 3.4). QUEST will similarly use twin co-located interferometers, and a light scalar field would couple to the beamsplitters of both interferometers and produce correlated oscillations in the size and index of refractions of both beamsplitters according to Eq. 3.9, allowing for a cross-correlation search.

The projected sensitivity of the QUEST experiment is shown in Fig. 3.16 (green lines), calculated using Eq. 3.9, assuming shot-noise-limited single interferometer sensitivities with 6 dB of squeezing in the frequency range $1 - 250$ MHz (see Fig. 1.8) and a cross-correlation time of $\sim 10^6$ s. Although the magnitude of the expected noise at lower frequencies is largely uncertain, given the measured sensitivity of e.g. the Fermilab Holometer, it is likely that competitive constraints can be set using QUEST at frequencies below 1 MHz as well.

Given the table-top design of the experiment, it would be relatively easy to modify the interferometers to enhance their sensitivity to scalar field dark matter. For example, mirrors of different thicknesses can be used as end mirrors of the arms. As the size changes in response to scalar field dark matter are proportional to the thickness of the optical substrates, having unequal end mirror thicknesses would produce a differential optical path length between the arms. Given a thickness difference of the mirrors Δd, a signal is then expected equal in magnitude to that produced by a beamsplitter with a thickness $l = \Delta d$ in an adiabatic approximation. The thicknesses and substrate materials could be chosen such that the mechanical frequency response of the mirrors (which depends on the thickness and substrate material) is such that the experiment provides sensitivity in a desired part of the parameter space. For example, several sets of mirrors with different fundamental vibrational frequencies could be used in separate measurements to sensitively probe for resonant interactions between dark matter and the optics and thus explore different narrow regions of the parameter space.

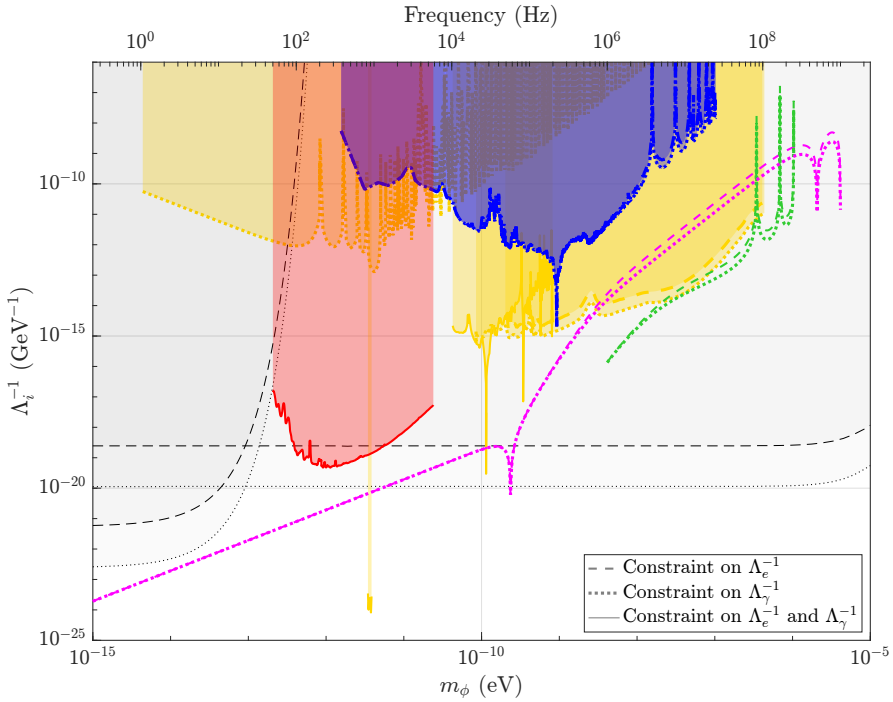

Figure 3.16. Part of the parameter space and constraints therein for light scalar field dark matter in the *Basic Scalar* scenario coupling to the beamsplitter. The green lines shows the projected time-integrated sensitivity of the QUEST experiment in terms of the dark matter coupling coefficients $\Lambda_\gamma, \Lambda_e$ as a function of the field's mass m_ϕ. This estimate assumes a cross-correlation time of 10^6 s, shot-noise-limited sensitivity between 1 and 250 MHz with 6 dB of squeezing, and is for a signal-to-noise ratio of one. The grey shaded areas are constraints from fifth-force searches and equivalence principle tests [116, 141–144]. The yellow shaded areas indicate constraints from direct experimental searches [137, 140, 146, 160]. The red and blue coloured regions are constraints set using GEO600 [2] (Sec. 3.3) and the Fermilab Holometer [3] (Sec. 3.4), respectively. In magenta, we show the projected constraints for the polarimetric experiment proposed in Sec. 3.5 [4].

4: Gravitational Waves

In this chapter, we present a new approach for detecting gravitational waves using existing and future detectors. Gravitational waves modulate the apparent frequencies of other periodic signals, and modulations due to low-frequency gravitational waves would therefore appear in the signals of higher-frequency gravitational waves. We outline an analysis method to systematically search for undetected gravitational waves in the background of well-resolved gravitational waves by looking for correlated frequency modulations of the latter. We show here that this method could allow gravitational-wave detectors to detect gravitational waves at frequencies outside of their designed bandwidth using the same infrastructure. This has the potential to open up unexplored and otherwise inaccessible parts of the gravitational wave spectrum.

We also comment on the prospects of detecting high-frequency (MHz) gravitational waves with the QUEST experiment.

Contributions to published work in this chapter
Sections 4.1 and 4.2 of this chapter are based on the manuscript

- Stegmann, J. & Vermeulen, S. M. "Detecting the heterodyning of gravitational waves". arXiv:2301.02672, to be submitted to a journal. Jan. 2023.

Both authors contributed equally to the manuscript. S.M.V. proposed the frequency-domain representation of the heterodyne signal, developed the cross-correlation analysis method, contributed to the production and analysis of the sensitivity projections, and wrote a large part of the manuscript.

4.1 Introduction: Gravitational Wave Detectors across the Spectrum

The field of gravitational-wave astronomy, as established with the first direct detection of gravitational waves (GWs) [7], is still in its infancy. So far, only GWs with frequencies between $\sim 10-500$ Hz produced by the coalescence of black holes and neutron stars with masses $\sim 1-100$ times the mass of our Sun have been detected [163]. New detectors and techniques are being developed to probe different regions of the GW frequency spectrum and to investigate numerous other potential GW sources; e.g., rotating neutron stars [164], binary white dwarfs (BWDs) [165], intermediate-mass and super-massive binary black holes (SMBBHs) [166], a background of primordial GWs [167], and dark matter [168, 169].

The sensitive bandwidth of laser interferometers (the only proven type of GW detector), is typically limited at low frequencies by spurious accelerations of the test masses, and at high frequencies by quantum uncertainty in the optical state and an intrinsically decreased response to GWs with wavelengths shorter than the interferometer's arms. Laser interferometers can be very sensitive at higher frequencies ($\sim 1-100$ MHz), using cross-correlation and shorter arms, such as in the QUEST experiment [1] and the Fermilab Holometer [16]. Increasing the sensitivity at lower frequencies is not straightforward, and even a space-based instrument such as LISA [170], subject to greatly reduced environmental noise compared to Earth-based instruments, will not be sensitive to GWs below $\sim 10^{-5}$ Hz. While marginal gains have been made in understanding and addressing the complex amalgam of low-frequency noise contributions encountered in laser interferometers (which include fundamental quantum limits) [171], it seems unlikely that their bandwidth will expand into lower frequencies by more than an order of magnitude in the coming decades.

Other detection techniques to probe new areas of the GW spectrum have been proposed and some have been tried; none have proven successful in detecting GWs so far. At high frequencies (kHz – GHz) these include techniques that exploit graviton-to-photon conversion (known as the inverse Gertsenshtein effect) [172, 173], optically levitated sensors, resonant mass detectors [174], and more [175].

At low frequencies, currently the only competitive method to search for GWs is using sets of time-resolved observations of pulsars, known as Pulsar Timing Arrays (PTAs), which are sensitive in the nHz – μHz range [176–185]. GWs incident on the pulsar and/or the detector produce deviations of the apparent frequency or equivalently the arrival time of the radio pulses that are correlated between different pulsars. This detection technique thus exploits the interplay of electromagnetic pulses with GWs which results

in a modulation of the pulse frequency. So far, after observing for $\sim 10\,\mathrm{yr}$, PTAs have not detected GWs [186–189].

4.2 Detecting the Heterodyning of Gravitational Waves

4.2.1 Introduction

In this section we propose a new method for detecting (low-frequency) GWs using interactions between GWs of different frequencies. The basis of the method is the gravitational red- and blueshift induced by one GW onto the other. This mechanism can also be viewed as one GW perturbing the space-time along the direction of travel of the other GW, and thus modulating the arrival times of peaks and troughs of the other GW. Mathematically, the effect can be described as a multiplication or mixing of two GWs. From this description, it can be shown that the resulting GW signal contains Fourier components at the sum and difference of the frequencies of the two waves, with an amplitude proportional to the product of the amplitudes of the individual GWs. This elementary result of the mixing of two waves, also known as heterodyning, has been used in the processing of electromagnetic signals for over a century. Heterodyning effectively produces a frequency-shifted copy of one signal (known as a sideband) in the frequency range of a readily detectable second signal. As we show in this paper, this mechanism can be used in GW astronomy, where GW signals detectable with, e.g., laser interferometers can be used to detect low-frequency background GWs. This method of searching for low-frequency GWs is conceptually similar to the technique used by PTAs, with the crucial difference that instead of looking for disturbances in the periodic electromagnetic signal of pulsars, we look for disturbances in a periodic GW signal. The idea of looking for GW sidebands was recently independently proposed by Bustamante et al. [190], when our paper was in preparation, but their analysis and projections differ significantly from ours.

Our proposed method allows one to expand the sensitive bandwidth of GW detectors into low-frequency regimes using the detectors' existing infrastructures. Moreover, this method could enable a sensitivity to GWs in a bandwidth where no other detection methods exist, e.g., in the μHz regime where the frequency ranges of space-based laser interferometers and PTAs leave a gap.

Although our method is applicable to general periodic GW signals, we focus here on the example of future space-based laser-interferometric GW detectors, i.e., LISA [170] and DECIGO [191], which are expected to be able to observe large numbers of GW signals from BWDs and binary neutron stars (BNSs). Using projected parameters of the detector and signals for these instruments, we show that cross-correlation of many well-resolved GW signals can provide sensitivity to secondary low-frequency GWs.

This section is structured as follows: in subsection 4.2.2 we derive the frequency domain signature of modulation of a primary carrier GW by a secondary low-frequency GW in the background of the carrier. In subsection 4.2.3, we present the proposed analysis method for detecting such background signals in GW detector data. In subsection 4.2.4, we construct a simulated data set of BWD carrier signals observed by LISA, and use this to make projections of the sensitivity that could be obtained with the proposed method. In subsection 4.2.5, we discuss possible limitations of our method and the assumptions made in estimating the achievable sensitivity. We formulate conclusions in subsection 4.2.6.

4.2.2 Theory: Gravitational Modulation of GW Signals

We consider a set of $N \gg 1$ periodic GW sources which could be simultaneously observed for a long time (e.g., BWDs in our Galaxy that could be individually resolved by LISA [170]). We further assume that these sources emit quasi-monochromatic GWs, i.e., that their frequency does not significantly change within the observation time T (see Sec. 4.2.5 for discussion of the implications of relaxing this assumption). In that case we can write the GW signal (in units of strain) from the α-th periodic source at distance d_α as

$$h_\alpha(t) = a_\alpha \cos[2\pi f_\alpha t + \varphi_\alpha], \qquad (\alpha = 1, 2, \ldots, N), \tag{4.1}$$

with constant frequency f_α, amplitude a_α, and initial phase φ_α. We refer to these GWs as carrier signals and to their sources as carrier sources.

If there is an incident GW from a secondary, more distant source, this GW will perturb the space-time at the location of the carrier sources and at the location of the observer. As a consequence, the frequency of the GW carrier signals are no longer constant but are modulated in time. For a secondary GW emitted by a distant point source in the direction $\hat{\boldsymbol{N}}$ this frequency modulation of the carrier signal is given by [192],

$$\frac{f_\alpha - f_\alpha(t)}{f_\alpha} = \frac{n^i_\alpha n^j_\alpha}{2(1 + \hat{\boldsymbol{N}} \cdot \hat{\boldsymbol{n}}_\alpha)} \left[H^{\mathrm{TT}}_{ij}(t, F_L) - H^{\mathrm{TT}}_{ij}(t_\alpha, F_{D,\alpha}) \right], \tag{4.2}$$

where $\hat{\boldsymbol{n}}_\alpha$ and n^i_α is the unit vector from the observer to the α-th carrier source and its components, respectively, and $t_\alpha = t - d_\alpha(1 + \hat{\boldsymbol{N}} \cdot \hat{\boldsymbol{n}}_\alpha)/c$ is the retarded time coordinate that accounts for the propagation of the carrier wave. $H^{\mathrm{TT}}_{ij}(t, F_L) = A \cos[2\pi F_L t + \Phi_L]$ and $H^{\mathrm{TT}}_{ij}(t_\alpha, F_{D,\alpha}) = A \cos[2\pi F_{D,\alpha} t_\alpha + \Phi_{D,\alpha}]$ correspond to the metric perturbation with Fourier frequencies $F_L, F_{D,\alpha}$, amplitude A, and phases $\Phi_L, F_{D,\alpha}$ due to the incident GW at the space-time locations of the observer and the carrier source, respectively (in the terminology of Pulsar Timing Arrays (PTAs) [176, 178], the former is usually

referred to as the 'Earth term' and the latter as the 'pulsar term'). We will from now on refer to the lower-frequency GW of interest that modulates the carrier signal as the background GW.

It can be shown that the single-sided frequency spectrum of the modulated signal can be written as [190]

$$\begin{aligned}\tilde{h}_\alpha(f) \simeq\ & a_\alpha e^{i\varphi_\alpha}\delta(f_\alpha - f) \\ & + \frac{1}{2}a_\alpha A I_{\alpha,L} e^{i(\varphi_\alpha+\Phi_L)}\delta(f - f_\alpha + F_L) \\ & + \frac{1}{2}a_\alpha A I_{\alpha,L} e^{-i(\varphi_\alpha+\Phi_L)}\delta(f - f_\alpha - F_L) \\ & + \frac{1}{2}a_\alpha A I_{\alpha,D} e^{i(\varphi_\alpha+\Phi_{\alpha,D})}\delta(f - f_\alpha + F_{D,\alpha}) \\ & + \frac{1}{2}a_\alpha A I_{\alpha,D} e^{-i(\varphi_\alpha+\Phi_{\alpha,D})}\delta(f - f_\alpha - F_{D,\alpha}),\end{aligned} \tag{4.3}$$

where $I_{\alpha,L,D} = (F_{L,D}/f_\alpha)\, K(\hat{\boldsymbol{N}}, \hat{\boldsymbol{n}}_\alpha, H_{ij}^{\mathrm{TT}}, d_\alpha)$, and K is a purely geometrical factor of order unity that accounts for the polarisation, propagation direction, and propagation distance of the background and carrier GWs. The first term in the spectrum given by Eq. 4.3 is the Fourier component corresponding to the carrier signal at the frequency $f = f_\alpha$. The modulation due to the background GW at the location of the observer manifests as two Fourier components with frequencies $f = f_\alpha \pm F_L$ (second and third term in Eq. 4.3), which we will refer to as the 'local' sideband terms. Similarly, the modulation of the carrier signal due to the background GW at the location of the carrier source produces sidebands with frequencies $f = f_\alpha \pm F_{D,\alpha}$ (fourth and fifth term), which we will refer to as the 'distant' sideband terms. Note that the frequency and phase offsets, F_L, Φ_L, of the 'local' terms are independent of the carrier (they are equal to the frequency and phase of the modulating GW at the location of the observer), whereas the 'distant' terms have frequency and phase offsets $F_{D,\alpha}, \Phi_{D,\alpha}$, which depend on the location of the carrier source.

This mechanism, a sort of 'GW heterodyning' could allow the indirect detection of low-frequency GWs that may otherwise be undetectable when a GW detector is not sensitive to signals down to a frequency F, but is sensitive at much higher frequencies $f_\alpha + F$. Using this method, the upconverted background signal amplitude is $A_{\mathrm{sideband}} = A a_\alpha K F/f_\alpha$. For example, if we take the carrier signal to be the GWs emitted by a typical BWD (such as the BWDs that LISA aims to detect), with frequency $f_\alpha \sim 10^{-2}\,\mathrm{Hz}$, and we take the background signal to be GWs emitted by a SMBBH with amplitude $A \sim 10^{-12}$ and frequency $F_L \sim 10^{-8}\,\mathrm{Hz}$, the background sideband signal appears at an amplitude $a_\alpha A I_{\alpha,L} \sim a_\alpha 10^{-6}$.

The suppression relative to the carrier would mean the background signal amplitude

is below the typical noise level of the detector. In the following section, we propose a method to amplify the signal which utilises the coherence of the modulation of multiple carrier signals. To this end, we construct and add $N_p = N(N-1)/2 \gg 1$ different cross-spectra (one for each pair of carrier sources) such that the sideband terms sum up coherently to exceed the incoherent random noise.

4.2.3 Cross-Correlation of Carrier Signals

We propose a cross-correlation method for detecting a background gravitational wave signal that produces phase modulation of carrier GW signals. We will later use this method to make quantitative estimates of the expected signal-to-noise ratio that can be obtained for potential astrophysical GW sources using planned GW detectors.

We consider the time-domain output signal of the GW detector $s(t)$ to be given by the sum of N carrier signals, all modulated by a single background GW signal with frequency F corresponding to either the 'local' ($F = F_L$) or the 'distant' ($F = F_D$) term, and noise $n(t)$ characteristic of the detector

$$s(t) = \sum_{\alpha=1}^{N} h_\alpha(t) + n(t). \tag{4.4}$$

For any carrier, we can apply a demodulation and phase-shift to the time-domain detector output and normalise it by the carrier amplitude and the constant I_α,

$$s_\alpha(t) = \frac{\sqrt{2}}{a_\alpha I_\alpha} e^{-i(2\pi f_\alpha t + \varphi_\alpha)}\, s(t). \tag{4.5}$$

This demodulation shifts the frequency of all Fourier components in the output by an amount f_α, such that all sideband (heterodyne) signals are frequency shifted to the frequency $\pm F$ of the modulating background GW that produces them. Moreover, any heterodyne signals from background GWs will now appear with a Fourier amplitude equal to the background GW strain amplitude that produces them. In general, the demodulation frequency need not be constant in time, but could be adjusted over time to account for time-dependent changes in the carrier frequency. Specifically, the demodulation frequency and phase could be varied according to a predetermined carrier signal model, or they could be fit to the data post hoc (e.g., through maximising the demodulated carrier amplitude) when the frequency evolution is unknown a priori. After this frequency and phase shift, we can apply an appropriate low-pass filter to the data such that other terms, as long as they are well-separated from the carrier and modulation sideband, need not be considered [1].

[1] The sidebands due to the local modulation can be considered well-separated in the frequency domain from the sidebands due to the distant modulation (pulsar/distant term) when $|F_L - F_D| \gg 1/T$. We also assume all carrier signals are well-separated from each other ($|f_\alpha - f_\beta| \gg 1/T \;\forall\; \alpha, \beta$).

We consider the case where the time-domain detector output is discretised with a constant sampling frequency f_s for a total observation time T. Next, we take the single-sided discrete Fourier transform of the detector output, which yields a discrete complex amplitude spectrum S_α^j for each carrier signal, which will have the form

$$S_\alpha^j = Ae^{i\Phi_\alpha}\delta_{jl(F)} + \frac{\sqrt{2}}{a_\alpha I_\alpha}\sqrt{\frac{\rho_\alpha^j}{T}}\, e^{i\eta_\alpha^j}, \tag{4.6}$$

where the index $j = 1, 2, \ldots, Tf_s/2$ runs over the frequency bins, $l(F)$ [2] is the index of the bin that contains the background signal (δ_{jl} is the Kronecker delta), ρ_α^j is the noise power spectral density of the detector, and η_α^j are the random noise phases (where both noise parameters have undergone the frequency and phase shift described by Eq. 4.5). The spectrum S_α^j is unique for each carrier signal. As background GWs would modulate all carrier signals coherently (i.e., the sideband phase is deterministic), whereas the noise has a random phase, cross-correlating different carrier signals is advantageous. For each pair of carrier signals $(\alpha\beta)$, a cross-spectrum $S_{\alpha\beta}^j = S_\alpha^j S_\beta^{j*}$, can be constructed which has the form

$$S_{\alpha\beta}^j = A^2 e^{i(\Phi_\alpha - \Phi_\beta)}\delta_{jl(F)} + \frac{2}{a_\alpha a_\beta I_\alpha I_\beta}\frac{\sqrt{\rho_\alpha^j \rho_\beta^j}}{T}\, e^{i\left(\eta_\alpha^j - \eta_\beta^j\right)}, \tag{4.7}$$

where $\Phi_\alpha - \Phi_\beta = \Phi_{\alpha\beta}$ is the phase difference of the modulating signal between the two carrier signals. Here, we neglect cross-terms between the sideband and the noise, as these are expected to be smaller than the pure noise terms. From this expression it can be seen that Φ_{ab} is deterministic, and $\eta_\alpha^j - \eta_\beta^j = \eta_{\alpha\beta}^j$ is random (the neglected sideband-noise cross-terms would likewise have random phases). Therefore, we can add up signal terms from different cross-spectra coherently, and the noise will average out. If we have N individually resolved carriers at our disposal we can construct $N_p = N(N-1)/2$ different cross spectra and take a coherent weighted average of them

$$S^j = \frac{\sum_{(\alpha\beta)}^{N_p} \lambda_{\alpha\beta}^j S_{\alpha\beta}^j\, e^{-i\Phi_{\alpha\beta}}}{\sum_{(\alpha\beta)}^{N_p} \lambda_{\alpha\beta}^j}, \tag{4.8}$$

where $\lambda_{\alpha\beta}^j$ are the weights of each cross-spectrum. Performing this coherent summation is possible as long as the relative modulation sideband phase $\Phi_{\alpha\beta}$ can be determined for each carrier pair $(\alpha\beta)$. For the modulation produced by the background GW at the detector ('local' term), $\Phi_{\alpha\beta} = 0\ \forall\, \alpha\beta$. For the sideband due to the modulation produced at the source of the carrier GW signal ('distant' term), $\Phi_{\alpha\beta}$ is a function of the relative

[2] $l(F) = \lceil FT + \frac{1}{2} \rceil$

positions of the background GW source and the carrier signal sources. In this case, Φ_{ab} can be taken as free parameters that are fit to the data by maximising the total SNR for a particular sideband frequency, which would yield an upper estimate of the maximum background GW signal power at a certain frequency. Alternatively, a hypothetical background source position and frequency could be assumed, which prescribes a certain set of $\Phi_{\alpha\beta}$ given the geometry of the source positions, which would then yield an upper limit of the estimated background GW strain at that frequency and sky position.

Note that the coherent average is constructed such that the expected real part of the signal bin is $\mathrm{E}\left[\mathrm{Re}[S^{l(F)}]\right] = A^2$. The squared signal-to-noise ratio can thus be defined for each bin

$$(\mathrm{SNR}^j)^2 = \frac{\left(\mathrm{Re}[S^j]\right)^2}{\mathrm{Var}\left(\mathrm{Re}[S^j]\right)}. \tag{4.9}$$

It can be shown that an optimal signal-to-noise ratio is found by taking the weights [193]

$$\lambda^j_{\alpha\beta} = \sum_{(\gamma\delta)}^{N_p} ([C^j]^{-1})_{\alpha\beta,\gamma\delta} \simeq \left(\frac{1}{\sigma^j_\alpha \sigma^j_\beta}\right)^2 = \frac{(a_\alpha a_\beta I_\alpha I_\beta)^2 T^2}{4\rho^j_\alpha \rho^j_\beta}, \tag{4.10}$$

where $C^j_{\alpha\beta,\delta\gamma}$ is the pair-wise cross-covariance matrix of the cross-spectra $S^j_{\alpha\beta}, S^j_{\delta\gamma}$, and $\sigma^j_{\alpha,\beta}$ are the variances of frequency bin j in each carrier spectrum (Eq. 4.6); the approximation holds in the weak-signal limit [193]. The SNR of a modulating background GW with frequency F and amplitude A can now be evaluated

$$(\mathrm{SNR}^{l(F)})^2 \simeq \frac{A^4}{2} \sum\nolimits_{(\alpha\beta)}^{N_p} \left(\frac{1}{\sigma^{l(F)}_\alpha \sigma^{l(F)}_\beta}\right)^2. \tag{4.11}$$

4.2.4 Sensitivity Projections using Simulated Carrier GW Signals

Simulating carrier GW signals

The GW detector LISA is expected to observe a large number of continuous, periodic GW signals from BWDs in our Galaxy [165, 170, 194–199]. These BWDs could potentially serve as carrier sources that allow for the detection of low-frequency background GWs as described above.

The total number and properties of Galactic BWDs is subject to large uncertainty. To obtain a quantitative projection for the number, frequency, and amplitude of BWD GW signals that may be detected with LISA, we use an observationally driven parametric model of the Galactic white dwarf population, constructed by Korol et al. [199]. This model builds upon the spectroscopic samples of single white dwarfs and BWDs from

Table 4.1. Input parameters used for generating synthetic populations of Galactic binary white dwarfs. The parameters $\rho^{\mathrm{Korol}}_{\mathrm{WD},\odot}$, $f^{\mathrm{Korol}}_{\mathrm{BWD},4\,\mathrm{AU}}$, $f^{\mathrm{Korol}}_{\mathrm{BWD},a_{\max}}$, and α^{Korol} are used as input for the algorithm described by [199] to model the sets of BWD carrier signals. These parameters represent the local WD density, the fraction of binaries with semi-major axes $< 4\,\mathrm{AU}$, the fraction of binaries with semi-major axes less than the maximum separation detectable with LISA ($a_{\max}$), and a power-law index specifying the BWD semi-major axis distribution, respectively (see [199] for details). The values of these parameters were chosen to correspond to upper (`Optimistic`), median (`Moderate`), and lower (`Pessimistic`) observational limits. We chose observation times T between 1.0 and 10.0 yr. N indicates the resulting number of BWDs which are individually resolvable with LISA.

Model		`Pessimistic`	`Moderate`	`Optimistic`
$\rho^{\mathrm{Korol}}_{\mathrm{WD},\odot}$	$[10^{-3}\,\mathrm{pc}^{-3}]$	4.11	4.49	4.87
$f^{\mathrm{Korol}}_{\mathrm{BWD},4\,\mathrm{AU}}$		0.112	0.095	0.078
$f^{\mathrm{Korol}}_{\mathrm{BWD},a_{\max}}$		0.008	0.009	0.010
α^{Korol}		-1.18	-1.30	-1.45
T	[yr]	1.0	4.0	10.0
N		7.0×10^4	1.1×10^5	1.9×10^5

the Sloan Digital Sky Survey (SDSS) and the Supernova Ia Progenitor surveY (SPY) to produce a synthetic population of Galactic BWDs which are specified by their component masses, orbital frequencies, sky positions, and orientations. These source parameters are then used to calculate the GW signals of each BWD in the population. Part of the BWDs would emit GWs at low frequencies $f \lesssim 3\,\mathrm{mHz}$ and are predicted to be so numerous that they are not individually resolvable but constitute a confusion-limited foreground noise [196]. The rest, an estimated number of $\sim \mathcal{O}(10^3 - 10^5)$ BWDs emit GWs at higher frequencies and are expected to be sufficiently loud that they are individually resolvable; these are the BWDs which can be used as carrier sources in our method.

We consider three models with different carrier source and observation parameters, `Pessimistic`, `Moderate`, and `Optimistic`. For these models, we synthesised three BWD populations using different input parameters for the model of [199]; specifically we vary the local WD density $\rho^{\mathrm{Korol}}_{\mathrm{WD},\odot}$, the WD binary fraction $f^{\mathrm{Korol}}_{\mathrm{BWD}}$, and the power-law index α^{Korol}, which describes the BWD semi-major axis distribution (see [199]). On the observation side we use three different values for the LISA mission lifetime $T = 1.0$, 4.0, and 10.0 yr, which sets the length of observation. To get an upper and lower limit for the resulting sensitivity to background GWs, we choose the model parameters such that `Pessimistic` and `Optimistic` models yield the lowest and highest number of

BWDs within the current observational uncertainty while `Moderate` model corresponds to median values. The parameter values of the three different models are summarised in Table 4.1.

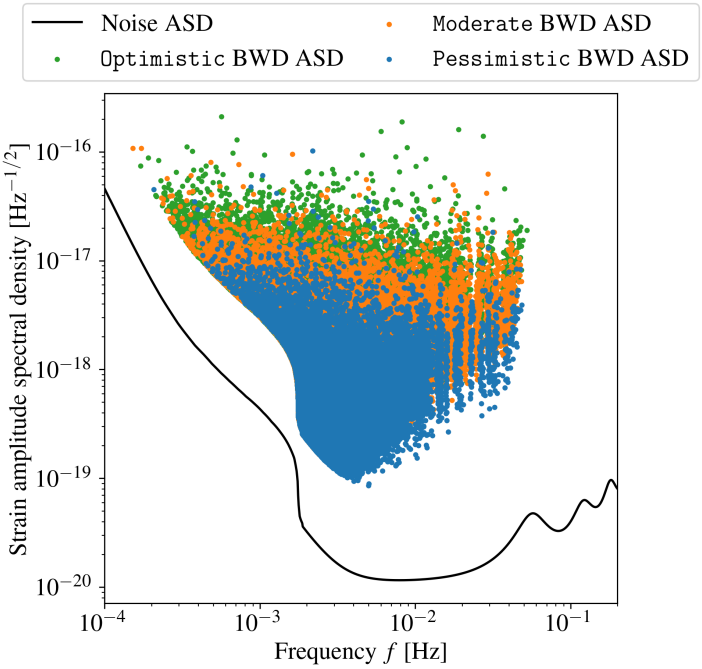

Figure 4.1. Amplitude spectral densities $a_\alpha\sqrt{T}$ of gravitational wave signals from individually resolvable binary white dwarfs (BWDs) in three different models [199] as a function of their frequency $f = f_\alpha$. The solid line indicates the root of the projected noise power spectral density $\sqrt{\rho}$ of LISA [199, 200]. BWDs are assumed to be individually resolvable if $a_\alpha\sqrt{T/\rho_\alpha} > 7$.

In Figure 4.1, we show the amplitude spectral density (ASD) of the BWD carriers for each model together with LISA's projected detector noise amplitude spectral density, as in [200], modified to account for the confusion noise due to unresolved BWDs derived by [199]. Throughout this work we assume a BWD to be individually resolvable if $a_\alpha\sqrt{T/\rho_\alpha} > 7$, although the precise threshold does not affect the resulting sensitivity due to the dominant contribution of loud sources (see Sec. 4.2.5).

Sensitivity projections

We estimate the sensitivity to background gravitational waves for the three models using our method, as in Eq. (4.11). Figure 4.2 shows the amplitude A versus frequency F of a background GW that could be detected with SNR = 2, corresponding to a $\simeq 95\,\%$ detection probability. The differences between the `Pessimistic` and `Optimistic`

models are less than one order of magnitude in A. Our method is sensitive to GWs with frequencies as low as $F \sim 10^{-8}\,\mathrm{Hz}$. GWs of these frequencies could be present in our Universe, e.g., as part of a (stochastic) background of GWs emitted by numerous individual sources [201]. At a frequency of $F \simeq 10^{-8}\,\mathrm{Hz}$ our method would be sensitive to amplitudes $A \gtrsim 10^{-10}$; GWs of that amplitude at that frequency could, e.g., be emitted by a very massive SMBBH with a chirp mass of several $\sim 10^{10}\,\mathrm{M}_\odot$ at a distance $D = 10\,\mathrm{Mpc}$, which is the order of magnitude of the distance to the Virgo cluster.

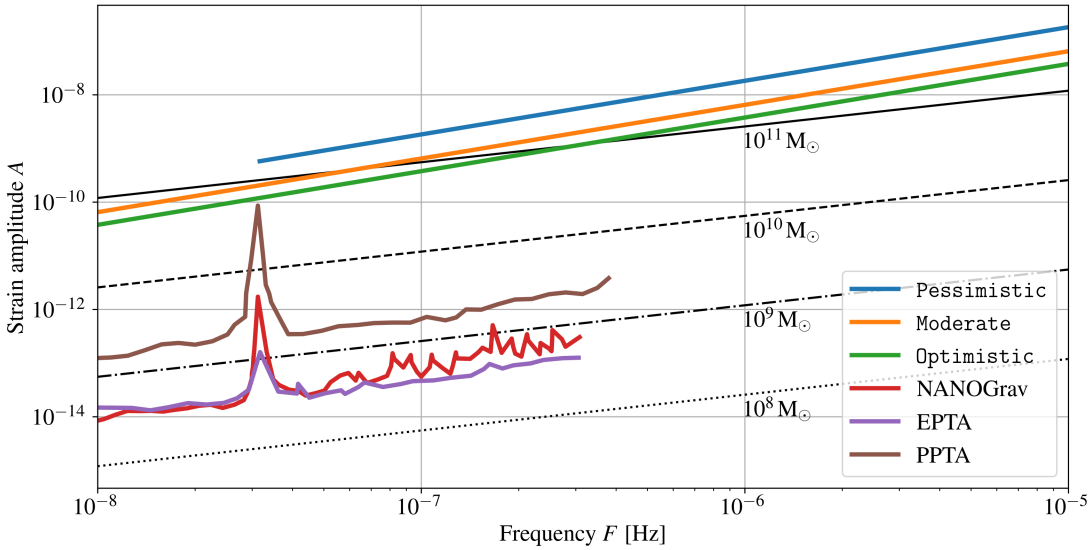

Figure 4.2. Sensitivity to low-frequency gravitational waves (GWs) that can be obtained by searching for correlated modulations in a set of well-resolved GW signals from binary white dwarfs (BWDs), as expected to be detected with LISA. For reference, we show the expected GW amplitudes of super-massive binary black holes with chirp masses ranging from 10^8 to $10^{11}\,\mathrm{M}_\odot$ at a fiducial distance $D = 10\,\mathrm{Mpc}$. We also show sensitivity curves from Pulsar Timing Arrays (PPTA [186]; EPTA [188]; NANOGrav [202]). The detection threshold (SNR = 2) is chosen to allow a consistent comparison to reported PTA sensitivities. In practice, we expect our method to show a reduction in sensitivity around $F \simeq 1/\mathrm{yr} \simeq 32\,\mathrm{nHz}$ as seen for PTAs, where it would be difficult to distinguish a background GW from the Doppler modulation due the annual motion of LISA around the sun. The sensitivity of our method is limited to frequencies $F \gtrsim 1/T$ (e.g., 32 nHz in the `Pessimistic` model), below which the sensitivity is limited by the finite width of the frequency bins.

We also consider the more general case of a number of carrier GW signals observed with any GW detector. For this case we assume that all N carrier signals have a similar frequency and are detected with the same SNR $\sim a_\alpha \sqrt{T/\rho_\alpha} = \mathrm{const}$. In Figure 4.3, we show the correlated background GW amplitude that can be detected at an SNR of one,

as a function of the number and individual SNR of the carrier signals.

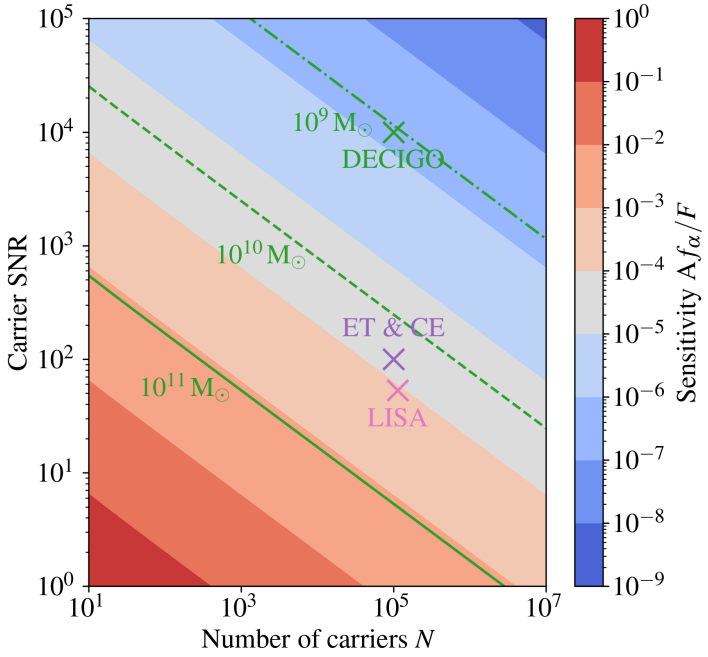

Figure 4.3. Order-of-magnitude estimate for the sensitivity to background gravitational waves (GWs) by cross-correlating a generic set of a number of GW signals N that are each detected with a certain SNR ('Carrier SNR'). The sensitivity (given by the colour scale) is expressed as the product of the background amplitude A times the typical frequency ratio of the background and carrier signals f_α/F, where the detection threshold corresponds to an SNR equal to one. Furthermore, we indicate the sensitivity that could be obtained using a set of GW signals in the dHz regime from binary neutron stars as carriers, which could be done using data from DECIGO [203], and similarly the sensitivity using carrier signals detected using ET and CE [204]. We also show the sensitivity that could be obtained using the average SNR of binary white dwarf signals detected by LISA (in the `Moderate` model), as explicated in Fig. 4.2. For these detectors we assume typical carrier frequencies of $f_\alpha \simeq 0.1\,\mathrm{Hz}$ (DECIGO), 10 Hz (ET/CE), and $10^{-3}\,\mathrm{Hz}$ (LISA). For reference, we show contour lines that correspond to GW amplitudes from super-massive binary black holes with chirp masses ranging from 10^9 to $10^{11}\,\mathrm{M}_\odot$ at a fiducial distance $D = 10\,\mathrm{Mpc}$, with a background frequency $F = 10^{-8}\,\mathrm{Hz}$, and a carrier frequency $f_\alpha = 0.1\,\mathrm{Hz}$.

We can apply this result to a proposed next-generation GW detector such as DECIGO [203, 205, 206], which operates in the dHz regime and is expected to observe GWs from a large number of compact binary stars. Assuming DECIGO observes GW signals from a population of $N = 10^5$ binary neutron stars (BNSs) each observed with an SNR of $\sim 10^4$ [203] at a typical frequency of $f_\alpha = 0.1\,\mathrm{Hz}$, it would be possible to detect

background GWs from SMBBHs with chirp masses of about $\sim 10^9\,\mathrm{M}_\odot$ (at a fiducial distance $D = 10\,\mathrm{Mpc}$ and frequency $F = 10^{-8}\,\mathrm{Hz}$). This would make the sensitivity of DECIGO to low-frequency GWs competitive with that of current PTAs (cf. Figure 4.2).

For reference, we also indicate in Figure 4.3 the sensitivity that could be obtained using $\sim 10^5$ carrier signals with an SNR $\sim 10^2$ from compact binary coalescences, as expected to be detected using both Einstein Telescope (ET) and Cosmic Explorer (CE) [204]. These carrier signals would have frequencies between 10 and 10^3 Hz and could be observed for a duration $T \lesssim 10^3$ s, which means the minimum detectable background GW frequency using our method is $F \sim 10^{-3}\,\mathrm{Hz}$. Coherent background GW signals may be searched for using non-coincident carrier signals with a slight modification of the method described in Sec. 4.2.3; a frequency-dependent phase correction ($\phi_{\mathrm{corr}} = 2\pi T_{\mathrm{diff}} F$) must be applied to each carrier's demodulated spectrum (Eq. 4.6), for a time difference between the signals T_{diff}. In case the background GW signal has a coherence time much shorter than the total observation time for all signals (i.e., the detector's lifetime), only coincident carrier signals can be cross-correlated to gain sensitivity.

The sensitivity of our method is fundamentally limited to frequencies $F \gtrsim 1/T$, as for lower frequencies the background signal cannot be distinguished from the carrier [190]. The same low-frequency limit due to observation time exists for PTAs. The high-frequency limit of our method is set by the Nyquist frequency of the detector output sampling, $f_s/2$, where for LISA $f_s \sim 1\,\mathrm{Hz}$ [190]. PTAs have a much smaller sensitive bandwidth due to the low observation cadence of radio telescopes (once every several days or less).

4.2.5 Discussion

There are several effects that could in practice degrade the sensitivity that would be obtained using our method.

We first consider stochastic effects due to which the carrier signal cannot be considered to be monochromatic, and their impact on the analysis. Of particular concern is phase noise imparted by the data acquisition system of the gravitational-wave detector. As this noise would appear as modulations of the carrier signal, it would obfuscate any background GWs that produce the same effect. Phase noise in the data acquisition system, due to, e.g., timing jitter of the sampling clocks, would produce irreducible correlated noise in the demodulated cross-spectra of different carriers. This effect might only be reduced by cross-correlating data obtained with different uncorrelated oscillators. Similarly, stochastic phase noise intrinsic to the carrier GW signal would reduce sensitivity to background GWs. In this case the effect on the sensitivity is limited as this noise will be uncorrelated between carriers and will be reduced in the average cross-spectrum (Eq. 4.8). However, uncertainty of the frequency of the carrier (due to

noise) would also lead to an uncertainty in the correct demodulation frequency, and this would lead to a sub-optimal (i.e. not fully coherent) addition of sidebands. A quantitative assessment of the impact on the sensitvity of our method due to these effects could performed using e.g. the Fisher information (if all noise sources are quantified), which we leave for future work.

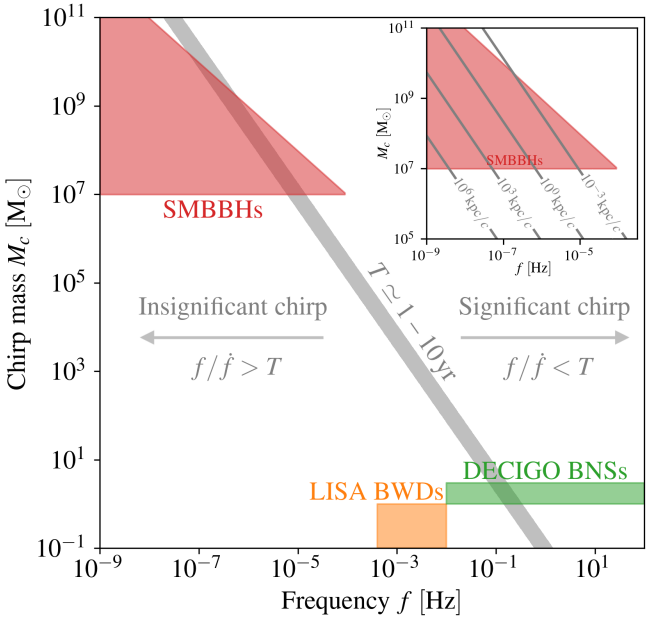

Figure 4.4. Timescale $f/\dot{f} = (5/96)(c^3/GM_c)^{5/3}(\pi f)^{-8/3}$ at which the frequency f of a compact binary with chirp mass M_c significantly increases due to energy loss through gravitational-wave emission. Coloured boxes indicate the parameter regions of background super-massive binary black holes (SMBBHs), LISA binary white dwarfs (BWDs), and DECIGO binary neutron stars (BNSs). This shows that LISA BWDs and most of the SMBBHs would not undergo significant frequency changes within the observation time $T \simeq 1 - 10\,\mathrm{yr}$, whereas most DECIGO BNSs would. The inset shows whether the SMBBHs would exhibit significant frequency changes within typical light travel times between a carrier source and the observer, i.e., whether 'local' and 'distant' sidebands overlap or not. For this figure we take the maximum GW frequency emitted by SMBBHs to correspond to the Innermost Stable Circular Orbit $f \lesssim 1\,\mathrm{kHz}\,(\mathrm{M}_\odot/M_c)$ evaluated for equal-mass binaries [73], which causes the diagonal cut-off.

In addition to these effective stochastic fluctuations of the carrier signal, there could be deterministic frequency changes of the carrier and background GWs. If the frequency of the background GWs changes significantly over the measurement time, i.e., if the GW background power spectral density is non-stationary, the coherent signal power would be spread over multiple frequency bins, leading to a lower SNR in each bin. An SMBBH

background source might undergo a significant frequency evolution as its orbital period decays due to energy loss by GW emission. Figure 4.4 shows that this frequency change $\dot{F}$ ('chirp') would not not be significant for SMBBHs ($M_c \gtrsim 10^9$) over the duration of observation $T \simeq 1 - 10\,\mathrm{yr}$. Figure 4.4 also shows the expected frequency changes of the LISA and DECIGO carrier signals. In particular, it shows that most DECIGO BNSs undergo significant frequency evolution over the duration of the detected signal. As discussed in Sec. 4.2.3, these frequency changes could be compensated for at the demodulation stage.

Non-stationarity of the background GW PSD has another effect; the frequency change over a time equal to the typical light travel time between the carrier source and observer determines the frequency-space separation of the 'local' and 'distant' sideband terms, i.e., $|F_L - F_D| \propto d_\alpha \dot{F}/c$. If these terms are not separated in the spectrum, i.e., when $|F_L - F_D| \lesssim 1/T$, coherent summation of the 'local' terms of different cross-spectra is still possible but the 'distant' terms would add a small incoherent noise-like contribution to any signal bin. The inset of Figure 4.4 shows that given typical light travel times between BWDs and the LISA detector of $d_\alpha/c \simeq 10^{-1} - 10^{1}\,\mathrm{kpc}/c$ [198], both separated and non-separated sidebands could be observed for background SMBBH GW sources. On the other hand, DECIGO will observe carrier signals from BNSs at much larger distances, e.g., $d_\alpha \simeq 10^4\,\mathrm{kpc}$ for a GW170817-like event [207], and therefore 'local' and 'distant' sidebands produced by a background SMBBH source ($M_c \gtrsim 10^9\,\mathrm{M}_\odot$) would be well-separated in DECIGO data.

We note that for the sensitivity projections for LISA, the number N of individually resolvable BWDs in our models (see Table 4.1) is larger by a factor up to ~ 10 compared to previous estimates from Galaxy models combined with a binary population model [165, 196, 198, 208, 209] which reflects the large uncertainty of current predictions about the detectable BWD population. However, the exact total number of BWDs does not significantly affect the estimated sensitivity because the $\sim \mathcal{O}(10^3)$ loudest BWDs signals provide the dominant contribution to the sensitivity. This is shown in Figure 4.5; where we plot the normalised cumulative contribution of BWDs to the total SNR. It can be seen that several 10^2 to 10^3 BWDs are enough to achieve similar sensitivities to the total BWD population.

4.2.6 Conclusion

In this work, we have outlined a method to use a set of carrier gravitational wave sources to search for correlated frequency modulations caused by low-frequency background gravitational waves. In this method demodulated cross-spectra of carrier sources are added coherently and with optimal weights such that any modulation common to the carrier sources is amplified with respect to random detector noise.

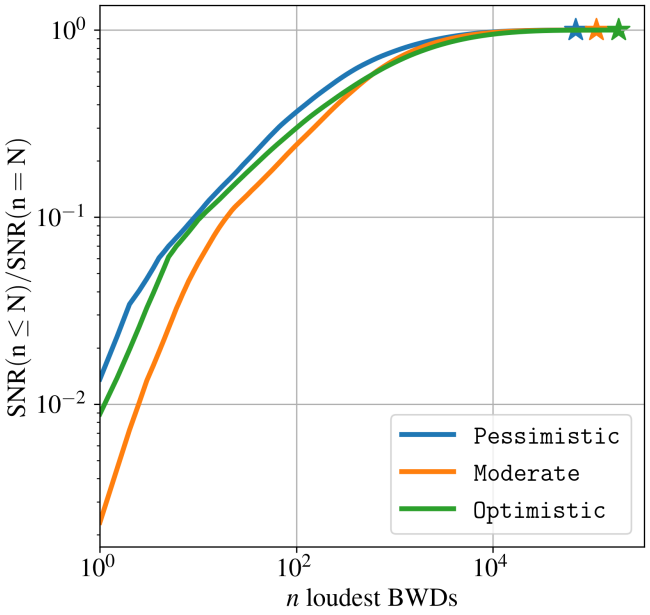

Figure 4.5. Cumulative SNR of a background gravitational wave signal as a function of the n loudest binary white dwarfs (BWDs) in the set of carrier signals. Stars at the end of each line indicate the total number N of binaries in each model. In any model several 10^2 to 10^3 of the loudest BWDs are enough to achieve sensitivities similar to the entire sample.

We considered the case of using our method to search for low-frequency GWs in data from LISA, which is expected to detect GWs from a large number of Galactic binary white dwarfs. The projected sensitivity that could thus be obtained (Figure 4.2) ranges from strain amplitudes of $A \sim 10^{-10}$ at $F \sim 10^{-8}$ Hz to $\sim 10^{-7}$ at $\sim 10^{-5}$ Hz, and would cover a part of the GW spectrum where no other detection methods are currently available.

This sensitivity could potentially enable the detection of very massive SMBBHs with a chirp mass of several $10^{10}\,\mathrm{M}_\odot$ at a distance of $D = 10\,\mathrm{Mpc}$, if such systems exist. Single super-massive BHs of several $\sim 10^{10}\,\mathrm{M}_\odot$ would be close to theoretical mass upper limits above which they cannot grow through luminous gas accretion [210], and so far candidates have only been observed at distances of more than several $\sim 100\,\mathrm{Mpc}$ [211, 212].

Our results show that an even better sensitivity could be achieved using GW signals from compact binary stars detectable with next-generation GW detectors that operate in the dHz regime. In particular, using signals of binary neutron stars expected to be detected with DECIGO would yield a sensitivity competitive with that of current pulsar

timing arrays.

Our results show that future detectors designed to detect GW signals in a higher frequency range could be used to indirectly probe GWs down to the frequencies given by the inverse instrument lifetime. Conveniently, this could be achieved without modification of the detector designs and with the same data outputs. This method could therefore prove a valuable tool in the exploration of the gravitational-wave spectrum and the development of gravitational-wave astronomy in general.

4.3 Prospects for Detecting Gravitational Waves with QUEST

Gravitational Waves (GWs) are predicted to exist at virtually all frequencies. The QUEST experiment will be uniquely sensitive to GWs in the MHz band.

The QUEST experiment is designed to allow for long measurement times over which data of the twin co-located interferometers can be continuously cross-correlated. The sensitivity to transient GW signals, such as those detected from the coalescence of compact binary objects of the kind detected so far [6], does not benefit greatly from this approach; the gain in sensitivity compared to a single detector for a transient signal is limited to a factor $\sqrt{2}$. On the other hand, for continuous gravitational wave signals, such as the set of signals that collectively form a stochastic background, cross-correlation will yield a sensitivity in the cross-spectrum that increases with the square root of the measurement time. While in theory the same statistical sensitivity (up to a factor $\sqrt{2}$) can obtained using a single interferometer, this is not be feasible in practice, and a cross-correlation approach is preferred (see Sec. 1.2.1). To use this cross-correlation method, the GW signals are required to have a coherence length greater than the separation between the two interferometers. Given the large separation between the LIGO/Virgo detectors, a cross-correlation approach with those detectors only works for much more coherent signals. QUEST could thus provide a gravitational wave strain sensitivity in the MHz band that approaches that of the LIGO/Virgo detectors in the $10^2 - 10^3$ Hz range for measurement times on the order of months.

In Fig. 4.6, we show the projected cross-correlated sensitivity to gravitational waves of the QUEST experiment compared to that of the Fermilab Holometer. The integrated strain sensitivity of the Holometer is taken as given in [18], where the integration time was $2.5 \cdot 10^6$ s. The projection of the sensitivity of the QUEST experiment assumes an equal cross-correlation time. The sensitivity is defined by a signal-to-noise ratio equal to one, and is computed for a GW incident perpendicular to the plane of the interferometer arms (as is conventional). The peaks in the sensitivity curves are due to the null response of interferometers to GW periods equal to twice the light-crossing time $2L/c$ (for normal incidence) [33]. We note that the constraints set on MHz GWs using the Fermilab Holometer in [14] erroneously assume a flat frequency response of the instrument. To correctly show the sensitivity to isotropic GW sources, such as a stochastic background, a sky-averaged antenna pattern needs to be used, such as done for LISA sensitivity curves (see e.g. Fig. 4.1).

Continuous MHz gravitational waves are predicted to be emitted by various astrophysical sources. Specifically, high-frequency GWs are likely present in an unresolved

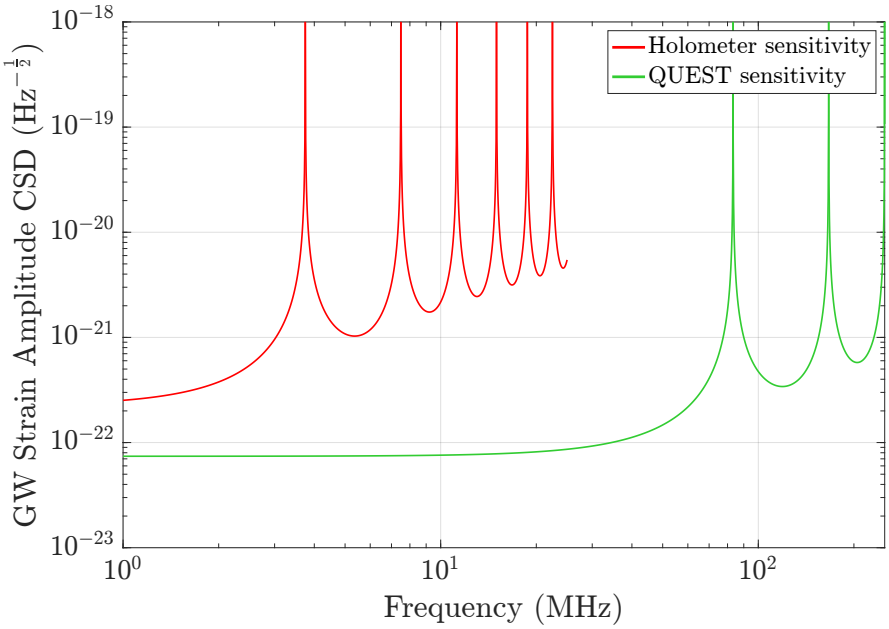

Figure 4.6. Projected sensitivity of the QUEST experiment (with 1.8-m arms) to gravitational-waves assuming a shot-noise-limited instrument with 6 dB of squeezing (see Sec. 1.5), compared to that attained with the Fermilab Holometer (with 40-m arms) for an equal cross-correlation time of $2.5 \cdot 10^6$ s [18], measured in strain noise amplitude cross-spectral density. The pattern of repeating peaks is due to the frequency response of a Michelson interferometer to gravitational waves incident perpendicular to the plane of the interferometer arms.

stochastic background [15], as they may be produced by e.g. primordial black holes [213, 214], cosmic strings [215], anisotropic inflation [216], and other sources in the early universe [217]. The merging of binary primordial black holes that exist to this day may also produce high-frequency GWs [14, 218]. In addition, it has been theorised that superradiant instabilities of rotating black holes due to undiscovered low-mass fields (e.g. dark matter) can be a source of monochromatic gravitational waves [219, 220], and the experiment would be sensitive to these GWs for certain parameter ranges.

While detections are not very likely, it seems worthwhile to explore this frequency range and develop the interferometer technology to unprecedented sensitivity [175, 221].

5: Conclusion

Through extensive development in the campaign to detect gravitational waves, laser interferometery has achieved a superlative sensitivity to optical path length changes; the technique now allows measurements of length variations on the order of 10^{-19} m. In this thesis, we have demonstrated how laser interferometry can be applied to measure fundamental physical phenomena with unrivalled sensitivity, specifically quantum space-time fluctuations, dark matter, and gravitational waves.

The QUEST experiment comprises a pair a pair of co-located laser interferometers with 3-m arms currently being commissioned at Cardiff University, and is expected to be sensitive to displacements $\sim 10^{19}$ m/$\sqrt{\text{Hz}}$ in a frequency band between 1 and 250 MHz, surpassing previous experiments. To achieve this sensitivity, the experiment uses a custom high-frequency data acquisition system that samples the output signals from the interferometers at 500 MHz and performs real-time Fourier transforms, cross-correlation, and averaging. We have expanded on the design, configuration, and performance of this FPGA-based system.

No theory exists that provides a description of the phenomenon of gravity consistent with the laws of quantum mechanics. It has been argued that space-time, inherent to General Relativity's geometrical description of gravity, must have quantum mechanical properties. More specifically it has been proposed that, if gravity is geometrical, and if gravity is quantum mechanical, geometry must be quantum mechanical, and hence lengths must exhibit quantum fluctuations. Partial theories of quantum gravity predict that if the covariant entropy bound holds for causal diamonds (in concordance with the holographic principle), and if there are quantum fluctuations associated with the bounding horizon of the causal diamond, length fluctuations of the order of the square root of the Planck length occur in laser interferometric measurements. If true, the QUEST experiment could measure these fluctuations in the length of its arms after ~ 1 year of measurement time and provide the first observation of a quantum gravity phenomenon.

Dark matter is a concept that was conceived to reconcile astronomical observations with General Relativity. A great number of different theoretical descriptions of dark matter exist, and despite extensive efforts to detect dark matter, its nature remains unclear. A class of theories posits that dark matter is made up of a low-mass ($\ll 1$ eV)

scalar field that interacts weakly with electrons and photons. This interaction would lead to oscillations of the size and index of refraction of solids. The optics in laser interferometers would thus exhibit such oscillations, and this would produce a signal in the output at the Compton frequency of the dark matter. We have demonstrated a novel optimised analysis method to search for such signals in data from the GEO600 gravitational-wave detector. Having ruled out the presence of scalar field dark matter signals at frequencies within the sensitive band of GEO600, we set upper limits on the strength of the coupling of dark matter to the electron and the photon for possible dark matter masses between 10^{-13} and 10^{-11} eV. These constraints improve on previous constraints set by purpose-built dark matter detectors by six orders of magnitude. We also performed a search for dark matter using cross-correlated measurements from the twin interferometers of the Fermilab Holometer, and set new bounds on the interaction strength for possible dark matter masses between 10^{-12} and 10^{-7} eV.

Laser interferometers are the only proven means of detecting gravitational waves to date, but the frequency range in which they are sensitive is intrinsically limited. While interferometers with shorter arms can offer sensitivity at very high frequencies (e.g. QUEST will be sensitive at frequencies up to 250 MHz), current and planned laser interferometers, including the space-based LISA detector, have very limited sensitivity at low frequencies ($\lesssim 10^{-5}$ Hz) due to an amalgam of instrumental and environmental noise. We proposed a new method to indirectly detect low-frequency gravitational waves by looking for the modulations they impart on well-resolved higher frequency gravitational wave signals. We consider that a low-frequency background gravitational wave will impart a periodic gravitational red- and blueshift on a higher-frequency gravitational wave signal; this effectively produces gravitational waves with an amplitude linear in the amplitudes of both the original waves at frequencies equal to the sum and difference of the original frequencies (i.e., frequency modulation sidebands are created). We showed that by cross-correlating the gravitational-wave signals from the large number of binary white dwarfs expected to be observed with LISA, this method would enable the detection of background gravitational waves with a strain amplitude of, e.g., $A \sim 10^{-10}$ at a frequency $F \sim 10^{-8}$ Hz, which may be emitted by a binary system of supermassible black holes.

Acknowledgements

We thank the Leverhulme Trust for support of this work under grant RPG-2019-022, and we thank the Science and Technology Facilities Council (STFC) for support of this work.

Bibliography

1. Vermeulen, S. M. *et al.* "An experiment for observing quantum gravity phenomena using twin table-top 3D interferometers". *Classical and Quantum Gravity* **38,** 085008. ISSN: 0264-9381, 1361-6382 (Apr. 2021).
2. Vermeulen, S. M. *et al.* "Direct limits for scalar field dark matter from a gravitational-wave detector". *Nature* **600.** ISSN: 1476-4687 (Dec. 2021).
3. Aiello, L. *et al.* "Constraints on Scalar Field Dark Matter from Colocated Michelson Interferometers". *Phys. Rev. Lett.* **128,** 121101 (12 Mar. 2022).
4. Ejlli, A., Vermeulen, S. M., Schwartz, E., Aiello, L. & Grote, H. "Probing dark matter with polarimetry techniques". arXiv:2211.09922, accepted for publication in Phys. Rev. D. Nov. 2022.
5. Stegmann, J. & Vermeulen, S. M. "Detecting the heterodyning of gravitational waves". arXiv:2301.02672, to be submitted to a journal. Jan. 2023.
6. LIGO Scientific Collaboration and Virgo Collaboration *et al.* "GWTC-2: Compact Binary Coalescences Observed by LIGO and Virgo during the First Half of the Third Observing Run". *Physical Review X* **11,** 021053 (June 9, 2021).
7. Abbott, B. P. et al. "Observation of Gravitational Waves from a Binary Black Hole Merger". *Physical Review Letters* **116,** 061102 (Feb. 2016).
8. Verlinde, E. P. & Zurek, K. M. "Observational signatures of quantum gravity in interferometers". *Physics Letters B* **822,** 136663. ISSN: 0370-2693 (Nov. 10, 2021).
9. Amelino-Camelia, G. "Gravity-wave interferometers as quantum-gravity detectors". *Nature* **398,** 216–218. ISSN: 0028-0836, 1476-4687 (Mar. 1999).
10. Ng, Y. J. & van Dam, H. "Measuring the foaminess of space-time with gravity-wave interferometers". *Foundations of Physics* **30,** 795–805. ISSN: 00159018 (2000).
11. Hogan, C. J. "Interferometers as probes of Planckian quantum geometry". *Physical Review D* **85,** 064007 (Mar. 2012).
12. Grote, H. & Stadnik, Y. V. "Novel signatures of dark matter in laser-interferometric gravitational-wave detectors". *Physical Review Research* **1,** 033187 (Dec. 2019).
13. Pierce, A., Riles, K. & Zhao, Y. "Searching for Dark Photon Dark Matter with Gravitational Wave Detectors". *Physical Review Letters* **121,** 061102. ISSN: 0031-9007, 1079-7114 (Aug. 8, 2018).
14. Chou, A. S. *et al.* "MHz Gravitational Wave Constraints with Decameter Michelson Interferometers". *Physical Review D* **95.** arXiv: 1611.05560, 063002. ISSN: 2470-0010, 2470-0029 (Mar. 2017).
15. Cruise, A. M. "The potential for very high-frequency gravitational wave detection". *Classical and Quantum Gravity* **29,** 095003. ISSN: 0264-9381, 1361-6382 (May 2012).
16. Chou, A. *et al.* "The Holometer: An Instrument to Probe Planckian Quantum Geometry". *Classical and Quantum Gravity* **34.** arXiv: 1611.08265, 065005. ISSN: 0264-9381, 1361-6382 (Mar. 2017).
17. Hogan, C. J. "Measurement of Quantum Fluctuations in Geometry". *Physical Review D* **77,** 104031. ISSN: 1550-7998, 1550-2368 (May 28, 2008).

18. Chou, A. *et al.* "Interferometric Constraints on Quantum Geometrical Shear Noise Correlations". *Classical and Quantum Gravity* **34.** arXiv: 1703.08503, 165005. ISSN: 0264-9381, 1361-6382 (Aug. 2017).

19. Hogan, C. "Exotic Rotational Correlations in Quantum Geometry". *Physical Review D* **95.** arXiv: 1509.07997, 104050. ISSN: 2470-0010, 2470-0029 (May 2017).

20. Hogan, C. J. & Kwon, O. "Statistical measures of Planck scale signal correlations in interferometers". *Classical and Quantum Gravity* **34,** 075006. ISSN: 0264-9381 (Mar. 2017).

21. Richardson, J. W. *et al.* "Interferometric Constraints on Spacelike Coherent Rotational Fluctuations". *Physical Review Letters* **126.** Publisher: American Physical Society, 241301 (June 14, 2021).

22. 't Hooft, G. "Black hole unitarity and antipodal entanglement". *Foundations of Physics* **46.** arXiv: 1601.03447, 1185–1198. ISSN: 0015-9018, 1572-9516 (Sept. 2016).

23. Gardner, W. A. "Statistical spectral analysis: a nonprobabilistic theory". ISBN: 978-0-13-844572-0 (USA, 1986).

24. McCuller, L. "Single-Photon Signal Sideband Detection for High-Power Michelson Interferometers". arXiv:2211.04016. Nov. 2022.

25. Schnier, D. *et al.* "Power recycling in the Garching 30 m prototype interferometer for gravitational-wave detection". *Physics Letters A* **225,** 210–216. ISSN: 03759601 (Feb. 1997).

26. Vahlbruch, H. *et al.* "The GEO600 squeezed light source". *Classical and Quantum Gravity* **27.** arXiv: 1004.4975, 084027. ISSN: 0264-9381, 1361-6382 (Apr. 2010).

27. Walls, D. F. "Squeezed states of light". *Nature* **306,** 141–146. ISSN: 1476-4687 (Nov. 1983).

28. Hild, S. *et al.* "DC-readout of a signal-recycled gravitational wave detector". *Classical and Quantum Gravity* **26,** 055012. ISSN: 0264-9381, 1361-6382 (Mar. 2009).

29. Fricke, T. T. *et al.* "DC readout experiment in Enhanced LIGO". *Classical and Quantum Gravity* **29.** arXiv: 1110.2815, 065005. ISSN: 0264-9381, 1361-6382 (Mar. 2012).

30. Caves, C. M. "Quantum-mechanical noise in an interferometer". *Physical Review D* **23,** 1693–1708. ISSN: 0556-2821 (Apr. 1981).

31. Davenport, W. B. & Root, W. L. "An Introduction to the Theory of Random Signals and Noise". ISBN: 978-0-87942-235-6 (1958).

32. Grote, H., Reitze, D. H. & Saulson, P. R. "Advanced Interferometric Gravitational-wave Detectors (In 2 Volumes)". ISBN: 978-981-314-609-9 (Mar. 2019).

33. Bond, C., Brown, D., Freise, A. & Strain, K. A. "Interferometer techniques for gravitational-wave detection". *Living Reviews in Relativity* **19,** 3. ISSN: 2367-3613, 1433-8351 (Dec. 2016).

34. Regehr, M. W., Raab, F. J. & Whitcomb, S. E. "Demonstration of a power-recycled Michelson interferometer with Fabry–Perot arms by frontal modulation". *Optics Letters* **20,** 1507–1509. ISSN: 1539-4794 (July 1995).

35. Pradyumna, S. T. *et al.* "Twin beam quantum-enhanced correlated interferometry for testing fundamental physics". *Communications Physics* **3,** 104. ISSN: 2399-3650 (2020).

36. Lough, J. *et al.* "First Demonstration of 6 dB Quantum Noise Reduction in a Kilometer Scale Gravitational Wave Observatory". *Physical Review Letters* **126,** 041102 (Jan. 26, 2021).

37. Tse et al, M. “Quantum-Enhanced Advanced LIGO Detectors in the Era of Gravitational-Wave Astronomy”. *Phys. Rev. Lett.* **123** (Dec. 2019).

38. Siegman, A. E. & Sziklas, E. A. “Mode Calculations in Unstable Resonators with Flowing Saturable Gain. 1:Hermite-Gaussian Expansion”. *Applied optics* **13** (Dec. 1974).

39. Chou, A. *et al.* “The Holometer: An Instrument to Probe Planckian Quantum Geometry”. *Classical and Quantum Gravity* **34.** arXiv: 1611.08265, 065005. ISSN: 0264-9381, 1361-6382 (Mar. 2017).

40. Zucker, M. & Whitcomb, S. “Proceedings of the Seventh Marcel Grossman Meeting on recent developments in theoretical and experimental general relativity, gravitation, and relativistic field theories”, 1434–1436 (1996).

41. E, F. E. & S, T. K. “Noise due to backscatter off baffles, the nearby wall, and objects at the far end of the beam tube; and recommended actions”. *Technical Report LIGO* **T940063-00-R** (1994).

42. labVIEW FPGA Module. `https://www.ni.com/en-gb/shop/software/products/labview-fpga-module.html` (2023).

43. Freise, A., Brown, D. & Bond, C. “Finesse, Frequency domain INterferomEter Simulation SoftwarE”. arXiv: 1306.2973 (June 2013).

44. Penrose, R. “On Gravity’s role in Quantum State Reduction”. *General Relativity and Gravitation* (1996).

45. Zych, M., Costa, F., Pikovski, I. & Brukner, Č. “Bell’s theorem for temporal order”. *Nature Communications* **10,** 3772. ISSN: 2041-1723 (Dec. 2019).

46. Donoghue, J. F. “Introduction to the Effective Field Theory Description of Gravity”. Dec. 11, 1995.

47. Ashtekar, A. & Geroch, R. “Quantum theory of gravitation”. *Reports on Progress in Physics* **37,** 1211. ISSN: 0034-4885 (Oct. 1974).

48. Wray, K. “An Introduction to String Theory”. Lecture Notes (2009).

49. Ashtekar, A. “Introduction to Loop Quantum Gravity”. arXiv: 1201.4598, 31–56 (2013).

50. Wigner, E. P. “Relativistic Invariance and Quantum Phenomena”. *Reviews of Modern Physics* **29,** 255–268. ISSN: 0034-6861 (July 1957).

51. Salecker, H. & Wigner, E. P. “Quantum Limitations of the Measurement of Space-Time Distances”. *Physical Review* **109,** 571–577. ISSN: 0031-899X (Jan. 1958).

52. Karolyhazy, F. “Gravitation and quantum mechanics of macroscopic objects”. *Il Nuovo Cimento A* **42,** 390–402. ISSN: 0369-3546, 1826-9869 (Mar. 1966).

53. Jack Ng, Y. & Van Dam, H. “LIMIT TO SPACE-TIME MEASUREMENT”. *Modern Physics Letters A* **09,** 335–340. ISSN: 0217-7323, 1793-6632 (Feb. 1994).

54. Amelino-Camelia, G. “Limits on the Measurability of Space-time Distances in (the Semi-classical Approximation of) Quantum Gravity”. *Modern Physics Letters A* **09.** arXiv: gr-qc/9603014, 3415–3422. ISSN: 0217-7323, 1793-6632 (Dec. 1994).

55. Ng, Y. J. “Selected topics in Planck-scale physics”. *Modern Physics Letters A* **18.** arXiv: gr-qc/0305019, 1073–1097. ISSN: 0217-7323, 1793-6632 (May 2003).

56. Christiansen, W. A., Floyd, D. J. E., Ng, Y. J. & Perlman, E. S. “Limits on Spacetime Foam”. *Physical Review D* **83.** arXiv: 0912.0535, 084003. ISSN: 1550-7998, 1550-2368 (Apr. 2011).

57. Singh, T. P. “Quantum gravity, minimum length and holography”. *Pramana* **95,** 40. ISSN: 0973-7111 (Feb. 20, 2021).

58. Garay, L. J. “Quantum gravity and minimum length”. *International Journal of Modern Physics A* **10,** 145–165. ISSN: 0217-751X, 1793-656X (Jan. 1995).

59. Hossenfelder, S. “Minimal Length Scale Scenarios for Quantum Gravity”. *Living Reviews in Relativity* **16.** arXiv: 1203.6191, 2. ISSN: 2367-3613, 1433-8351 (Dec. 2013).

60. Amelino-Camelia, G. “Quantum Spacetime Phenomenology”. *Living Reviews in Relativity* **16.** arXiv: 0806.0339, 5. ISSN: 2367-3613, 1433-8351 (Dec. 2013).

61. Zurek, K. M. “On vacuum fluctuations in quantum gravity and interferometer arm fluctuations”. *Physics Letters B* **826,** 136910. ISSN: 03702693 (Mar. 2022).

62. Verlinde, E. & Zurek, K. M. “Modular fluctuations from shockwave geometries”. *Physical Review D* **106,** 106011 (Nov. 17, 2022).

63. Li, D., Lee, V. S. H., Chen, Y. & Zurek, K. M. “Interferometer response to geontropic fluctuations”. *Physical Review D* **107,** 024002 (Jan. 4, 2023).

64. Kwon, O. “Phenomenology of Holography via Quantum Coherence on Causal Horizons”. July 13, 2022.

65. Hogan, C. J. “Quantum Gravitational Uncertainty of Transverse Position”. Sept. 26, 2007.

66. Hogan, C. J. “Quantum Entanglement of Matter and Geometry in Large Systems”. arXiv: 1412.1807 (Dec. 2014).

67. Hogan, C., Kwon, O. & Richardson, J. “Statistical model of exotic rotational correlations in emergent space-time”. *Classical and Quantum Gravity* **34,** 135006. ISSN: 0264-9381, 1361-6382 (July 2017).

68. Hogan, C. & Kwon, O. “Models of Exotic Interferometer Cross-Correlations in Emergent Space-Time”. *Classical and Quantum Gravity* **35,** 204001. ISSN: 0264-9381, 1361-6382 (Oct. 25, 2018).

69. Verlinde, E. & Zurek, K. M. “Spacetime fluctuations in AdS/CFT”. *Journal of High Energy Physics* **2020,** 209. ISSN: 1029-8479 (Apr. 30, 2020).

70. Banks, T. “Holographic Space-Time and Quantum Information”. *Frontiers in Physics* **8.** ISSN: 2296-424X (2020).

71. Bousso, R. “The holographic principle”. *Reviews of Modern Physics* **74.** arXiv: hep-th/0203101, 825–874. ISSN: 0034-6861, 1539-0756 (Aug. 2002).

72. Bekenstein, J. D. “Universal upper bound on the entropy-to-energy ratio for bounded systems”. *Physical Review D* **23,** 287–298 (Jan. 15, 1981).

73. Maggiore, M. “Gravitational Waves: Volume 1: Theory and Experiments”. ISBN: 978-0198570745 (Oxford, 2008).

74. Lewkowycz, A. & Maldacena, J. “Generalized gravitational entropy”. *Journal of High Energy Physics* **2013,** 90. ISSN: 1029-8479 (Aug. 2013).

75. Hogan, C. “Nonlocal entanglement and directional correlations of primordial perturbations on the inflationary horizon”. *Physical Review D* **99,** 063531. ISSN: 2470-0010, 2470-0029 (Mar. 2019).

76. 't Hooft, G. "The Quantum Black Hole as a Hydrogen Atom: Microstates Without Strings Attached". arXiv: 1605.05119 (May 2016).

77. Perlman, E. S. *et al.* "New Constraints on Quantum Gravity from X-ray and Gamma-Ray Observations". *The Astrophysical Journal* **805,** 10. ISSN: 1538-4357 (May 2015).

78. Ng, Y. J. & Perlman, E. S. Probing Spacetime Foam with Extragalactic Sources of High-Energy Photons. arXiv:2205.12852 (May 25, 2022).

79. Hogan, C. "Pattern of perturbations from a coherent quantum inflationary horizon". *Classical and Quantum Gravity* **37,** 095005. ISSN: 0264-9381 (Apr. 2020).

80. Hogan, C., Kwon, O. & Selub, N. "Angular spectrum of quantum fluctuations in causal structure". Mar. 2023.

81. Pitkin, M., Reid, S., Rowan, S. & Hough, J. "Gravitational Wave Detection by Interferometry (Ground and Space)", 75 (2011).

82. Martynov, D. V. *et al.* "Sensitivity of the Advanced LIGO detectors at the beginning of gravitational wave astronomy". *Physical Review D* **93,** 112004. ISSN: 2470-0010, 2470-0029 (June 2, 2016).

83. Kwon, O. & Hogan, C. J. "Interferometric tests of Planckian quantum geometry models". *Classical and Quantum Gravity* **33,** 105004. ISSN: 0264-9381 (Apr. 2016).

84. Balamurugan, S., Vermeulen, S. M. & Datta, A. "Extracting optical signatures of quantum space-time fluctuations". Manuscript in preparation. 2023.

85. Rakhmanov, M. "Response of LIGO to Gravitational Waves at High Frequencies and in the Vicinity of the FSR (37.5 kHz) (LIGO Document T060237-x0)". Apr. 2005.

86. Schutz, B. F. "A first course in general relativity". ISBN: 9780521257701 (1985).

87. Czech, B., Lamprou, L., McCandlish, S. & Sully, J. "Integral geometry and holography". *Journal of High Energy Physics* **2015,** 175. ISSN: 1029-8479 (Oct. 27, 2015).

88. Bub, M. W. *et al.* "Quantum Gravity Background in Next-Generation Gravitational Wave Detectors". May 18, 2023.

89. Banks, T. "Holographic Space-Time: The Takeaway". arXiv: 1109.2435 (Sept. 2011).

90. Gibbons, G. W. & Solodukhin, S. N. "The geometry of small causal diamonds". *Physics Letters B* **649,** 317–324. ISSN: 0370-2693 (June 2007).

91. Zwicky, F. "Die Rotverschiebung von extragalaktischen Nebeln". *Helvetica Physica Acta* **6.** ADS Bibcode: 1933AcHPh...6..110Z, 110–127. ISSN: 0018-0238 (Jan. 1933).

92. Rubin, V. C. & Ford, W. K. "Rotation of the Andromeda Nebula from a Spectroscopic Survey of Emission Regions". *The Astrophysical Journal* **159,** 379. ISSN: 0004-637X (Feb. 1970).

93. Gavazzi, R. *et al.* "The Sloan Lens ACS Survey. IV. The Mass Density Profile of Early-Type Galaxies out to 100 Effective Radii". *The Astrophysical Journal* **667.** ADS Bibcode: 2007ApJ...667..176G, 176–190. ISSN: 0004-637X (Sept. 2007).

94. McGaugh, S. S., Lelli, F. & Schombert, J. M. "Radial Acceleration Relation in Rotationally Supported Galaxies". *Physical Review Letters* **117** (Nov. 9, 2016).

95. McGaugh, S., Lelli, F., Li, P. & Schombert, J. "Dynamical Regularities in Rotating Galaxies". *Proceedings of the International Astronomical Union. International Astronomical Union* **353** (2019).

96. Moore, B. “Evidence against dissipation-less dark matter from observations of galaxy haloes”. *Nature* **370,** 629–631. ISSN: 1476-4687 (Aug. 1994).

97. Blok, D. & G, W. J. “The Core-Cusp Problem”. *Advances in Astronomy* **2010,** e789293. ISSN: 1687-7969 (Nov. 25, 2009).

98. Bertone, G. & Tait, T. “A new era in the search for dark matter”. *Nature* **562,** 51–56 (2018).

99. Hall, E. D., Frolov, T. C. V. V., Müller, H., Pospelov, M. & Adhikari, R. X. “Laser Interferometers as Dark Matter Detectors”. *Physical Review D* **98.** arXiv: 1605.01103, 083019. ISSN: 2470-0010, 2470-0029 (Oct. 2018).

100. Adams, A. W. & Bloom, J. S. “Direct Detection of Dark Matter with Space-based Laser Interferometers”. arXiv: astro-ph/0405266 (May 2004).

101. Tsuchida, S., Kanda, N., Itoh, Y. & Mori, M. “Dark matter signals on a laser interferometer”. *Physical Review D* **101,** 023005 (Jan. 2020).

102. Derevianko, A. & Pospelov, M. “Hunting for topological dark matter with atomic clocks”. *Nature Physics* **10,** 933–936. ISSN: 1745-2473, 1745-2481 (Dec. 2014).

103. Arvanitaki, A., Baryakhtar, M. & Huang, X. “Discovering the QCD Axion with Black Holes and Gravitational Waves”. *Physical Review D* **91,** 084011. ISSN: 1550-7998, 1550-2368 (Apr. 7, 2015).

104. Arvanitaki, A., Huang, J. & Van Tilburg, K. “Searching for dilaton dark matter with atomic clocks”. *Physical Review D* **91,** 015015. ISSN: 1550-7998, 1550-2368 (Jan. 21, 2015).

105. Stadnik, Y. V. & Flambaum, V. V. “Can dark matter induce cosmological evolution of the fundamental constants of Nature?” *Physical Review Letters* **115,** 201301. ISSN: 0031-9007, 1079-7114 (Nov. 12, 2015).

106. Read, J. I. “The local dark matter density”. *Journal of Physics G: Nuclear and Particle Physics* **41,** 063101. ISSN: 0954-3899 (May 2014).

107. Derevianko, A. “Detecting dark matter waves with precision measurement tools”. *Physical Review A* **97,** 042506. ISSN: 2469-9926, 2469-9934 (Apr. 26, 2018).

108. Ringwald, A. “Exploring the role of axions and other WISPs in the dark universe”. *Physics of the Dark Universe. Next Decade in Dark Matter and Dark Energy* **1,** 116–135. ISSN: 2212-6864 (Nov. 1, 2012).

109. Hees, A., Minazzoli, O., Savalle, E., Stadnik, Y. V. & Wolf, P. “Violation of the equivalence principle from light scalar dark matter”. *Physical Review D* **98,** 064051. ISSN: 2470-0010, 2470-0029 (Sept. 25, 2018).

110. Damour, T. & Polyakov, A. M. “The String Dilaton and a Least Coupling Principle”. *Nuclear Physics B* **423.** arXiv: hep-th/9401069, 532–558. ISSN: 05503213 (July 1994).

111. Arvanitaki, A., Dimopoulos, S. & Van Tilburg, K. “Sound of Dark Matter: Searching for Light Scalars with Resonant-Mass Detectors”. *Physical Review Letters* **116.** arXiv: 1508.01798, 031102. ISSN: 0031-9007, 1079-7114 (Jan. 2016).

112. Damour, T. & Donoghue, J. F. “Equivalence Principle Violations and Couplings of a Light Dilaton”. *Physical Review D* **82.** arXiv: 1007.2792, 084033. ISSN: 1550-7998, 1550-2368 (Oct. 2010).

113. Flacke, T., Frugiuele, C., Fuchs, E., Gupta, R. S. & Perez, G. "Phenomenology of relaxion-Higgs mixing". *Journal of High Energy Physics* **2017.** arXiv: 1610.02025 version: 3, 50. ISSN: 1029-8479 (June 2017).

114. Banerjee, A., Kim, H. & Perez, G. "Coherent relaxion dark matter". *Physical Review D* **100.** arXiv: 1810.01889, 115026. ISSN: 2470-0010, 2470-0029 (Dec. 2019).

115. Banerjee, A., Budker, D., Eby, J., Kim, H. & Perez, G. "Relaxion stars and their detection via atomic physics". *Communications Physics* **3,** 1. ISSN: 2399-3650 (Dec. 2020).

116. Wagner, T. A., Schlamminger, S., Gundlach, J. H. & Adelberger, E. G. "Torsion-balance tests of the weak equivalence principle". *Classical and Quantum Gravity* **29,** 184002. ISSN: 0264-9381 (Aug. 2012).

117. Morisaki, S. & Suyama, T. "Detectability of ultralight scalar field dark matter with gravitational-wave detectors". *Physical Review D* **100,** 123512 (Dec. 2019).

118. Pašteka, L. F., Hao, Y., Borschevsky, A., Flambaum, V. V. & Schwerdtfeger, P. "Material Size Dependence on Fundamental Constants". *Physical Review Letters* **122,** 160801 (Apr. 2019).

119. Antypas, D. *et al.* "New Horizons: Scalar and Vector Ultralight Dark Matter". arXiv:2203.14915 (Mar. 2022).

120. Marsh, D. J. "Axion cosmology". *Physics Reports* **643.** Axion cosmology, 1–79. ISSN: 0370-1573 (2016).

121. Sakharov, A., Sokoloff, D. & Khlopov, M. Y. "Large-scale modulation of the distribution of coherent oscillations of a primordial axion field in the universe". *Physics of Atomic Nuclei* **59,** 1005–1010 (1996).

122. Berezhiani, Z. & Khlopov, M. Y. "Cosmology of spontaneously broken gauge family symmetry with axion solution of strong CP-problem". *Zeitschrift für Physik C Particles and Fields* **49,** 73–78 (1991).

123. Berezhiani, Z., Sakharov, A. & Khlopov, M. Y. "Primordial background of cosmological axions." *Soviet Journal of Nuclear Physics* **55,** 1063–1071 (1992).

124. DeRocco, W. & Hook, A. "Axion interferometry". *Physical Review D* **98,** 035021. ISSN: 2470-0010, 2470-0029 (Aug. 2018).

125. Nagano, K., Fujita, T., Michimura, Y. & Obata, I. "Axion Dark Matter Search with Interferometric Gravitational Wave Detectors". *Physical Review Letters* **123,** 111301 (Sept. 2019).

126. Martynov, D. & Miao, H. "Quantum-enhanced interferometry for axion searches". *Physical Review D* **101,** 095034 (May 2020).

127. Dooley, K. L. *et al.* "GEO 600 and the GEO-HF upgrade program: successes and challenges". *Classical and Quantum Gravity* **33,** 075009 (2016).

128. Geraci, A. A., Bradley, C., Gao, D., Weinstein, J. & Derevianko, A. "Searching for ultra-light dark matter with optical cavities". *Physical Review Letters* **123,** 031304. ISSN: 0031-9007, 1079-7114 (2019).

129. Hewitson, M., Heinzel, G., Smith, J. R., Strain, K. A. & Ward, H. "Principles of calibrating the dual-recycled GEO 600". *Review of Scientific Instruments* **75,** 4702–4709. ISSN: 0034-6748, 1089-7623 (Nov. 2004).

130. Tröbs, M. & Heinzel, G. "Improved spectrum estimation from digitized time series on a logarithmic frequency axis". *Measurement* **39,** 120–129. ISSN: 02632241 (Feb. 2006).

131. Miller, A. L. *et al.* "Adapting a semi-coherent method to directly detect dark photon dark matter interacting with gravitational-wave interferometers". arXiv:2010.01925 (2020).

132. Abbott, B. P. *et al.* "Properties of the Binary Neutron Star Merger GW170817". *Phys. Rev. X* **9,** 011001 (1 2019).

133. Freese, K., Lisanti, M. & Savage, C. "Annual Modulation of Dark Matter: A Review". *Reviews of Modern Physics* **85,** 1561–1581. ISSN: 0034-6861, 1539-0756 (Nov. 1, 2013).

134. Welch, P. "The use of fast Fourier transform for the estimation of power spectra: A method based on time averaging over short, modified periodograms". *IEEE Transactions on Audio and Electroacoustics* **15,** 70–73 (1967).

135. Van Tilburg, K., Leefer, N., Bougas, L. & Budker, D. "Search for Ultralight Scalar Dark Matter with Atomic Spectroscopy". *Physical Review Letters* **115,** 011802 (2015).

136. Hees, A., Guéna, J., Abgrall, M., Bize, S. & Wolf, P. "Searching for an oscillating massive scalar field as a dark matter candidate using atomic hyperfine frequency comparisons". *Physical Review Letters* **117,** 061301. ISSN: 0031-9007, 1079-7114 (2016).

137. Aharony, S. *et al.* "Constraining rapidly oscillating scalar dark matter using dynamic decoupling". *Physical Review D* **103,** 075017 (Apr. 20, 2021).

138. Antypas, D. *et al.* "Scalar Dark Matter in the Radio-Frequency Band: Atomic-Spectroscopy Search Results". *Physical Review Letters* **123,** 141102 (Oct. 2019).

139. Savalle, E. *et al.* "Searching for dark matter with an unequal delay interferometer". *Physical Review Letters* **126,** 051301. ISSN: 0031-9007, 1079-7114 (Feb. 4, 2021).

140. Branca, A. *et al.* "Search for an Ultralight Scalar Dark Matter Candidate with the AURIGA Detector". *Physical Review Letters* **118,** 021302. ISSN: 0031-9007, 1079-7114 (2017).

141. Smith, G. L. *et al.* "Short-range tests of the equivalence principle". *Physical Review D* **61,** 022001 (1999).

142. Schlamminger, S., Choi, K.-Y., Wagner, T. A., Gundlach, J. H. & Adelberger, E. G. "Test of the Equivalence Principle Using a Rotating Torsion Balance". *Physical Review Letters* **100,** 041101 (Jan. 2008).

143. Bergé, J. *et al.* "MICROSCOPE Mission: First Constraints on the Violation of the Weak Equivalence Principle by a Light Scalar Dilaton". *Physical Review Letters* **120,** 141101 (2018).

144. Leefer, N., Gerhardus, A., Budker, D., Flambaum, V. V. & Stadnik, Y. V. "Search for the Effect of Massive Bodies on Atomic Spectra and Constraints on Yukawa-Type Interactions of Scalar Particles". *Physical Review Letters* **117,** 271601 (2016).

145. Kennedy, C. J. *et al.* "Precision Metrology Meets Cosmology: Improved Constraints on Ultralight Dark Matter from Atom-Cavity Frequency Comparisons". *Physical Review Letters* **125,** 201302 (Nov. 2020).

146. Savalle, E. *et al.* "Novel approaches to dark-matter detection using space-time separated clocks". arXiv:1902.07192 (2019).

147. Chou, A. S. *et al.* "First Measurements of High Frequency Cross-Spectra from a Pair of Large Michelson Interferometers". *Phys. Rev. Lett.* **117,** 111102 (11 2016).

148. Martinez, J. G. C. & Kamai, B. “Searching for MHz gravitational waves from harmonic sources”. *Classical and Quantum Gravity* **37,** 205006. ISSN: 1361-6382 (Sept. 2020).

149. Euler, H. & Kockel, B. “Über die Streuung von Licht an Licht nach der Diracschen Theorie”. *Naturwissenschaften* **23,** 246–247. ISSN: 1432-1904 (Apr. 1935).

150. Erber, T. “Velocity of Light in a Magnetic Field”. *Nature* **190,** 25–27. ISSN: 1476-4687 (Apr. 1961).

151. Iacopini, E. & Zavattini, E. “Experimental method to detect the vacuum birefringence induced by a magnetic field”. *Physics Letters B* **85,** 151–154. ISSN: 0370-2693 (July 1979).

152. Zavattini, G. *et al.* “Polarimetry for measuring the vacuum magnetic birefringence with quasi-static fields: a systematics study for the VMB@CERN experiment”. *The European Physical Journal C* **82,** 159. ISSN: 1434-6052 (May 2022).

153. Ejlli, A. *et al.* “The PVLAS experiment: A 25 year effort to measure vacuum magnetic birefringence”. *Physics Reports. The PVLAS experiment: A 25 year effort to measure vacuum magnetic birefringence* **871,** 1–74. ISSN: 0370-1573 (Aug. 2, 2020).

154. Ejlli, A., Della Valle, F. & Zavattini, G. “Polarisation dynamics of a birefringent Fabry–Perot cavity”. *Applied Physics B* **124,** 22. ISSN: 0946-2171, 1432-0649 (Feb. 2018).

155. Satari, H. *et al.* “Low coherency of wind induced seismic noise: implications for gravitational wave detection”. *Classical and Quantum Gravity* **39,** 215015 (Nov. 2022).

156. Schwartz, E. *et al.* “Improving the robustness of the advanced LIGO detectors to earthquakes”. *Classical and Quantum Gravity* **37,** 235007 (Nov. 2020).

157. Cahillane, C. & Mansell, G. “Review of the Advanced LIGO Gravitational Wave Observatories Leading to Observing Run Four”. *Galaxies* **10,** 36 (Nov. 2022).

158. Marchiò, M., Leonardi, M., Bazzan, M. & Flaminio, R. “3D characterization of low optical absorption structures in large crystalline sapphire substrates for gravitational wave detectors”. *Sci. Rep.* **11,** 2654 (2021).

159. Aiello, L. *et al.* “Thermal compensation system in advanced and third generation gravitational wave interferometric detectors”. *Journal of Physics: Conference Series* **1226,** 012019 (May 2019).

160. Tretiak, O. *et al.* “Improved Bounds on Ultralight Scalar Dark Matter in the Radio-Frequency Range”. *Phys. Rev. Lett.* **129,** 031301 (3 July 2022).

161. Anastassopoulos, V. *et al.* “New CAST limit on the axion-photon interaction”. *Nature Physics* **13,** 584–590 (2017).

162. Bähre, R. *et al.* “Any light particle search II — Technical Design Report”. *Journal of Instrumentation* **8,** T09001 (Sept. 2013).

163. Abbott, R. *et al.* “Population of Merging Compact Binaries Inferred Using Gravitational Waves through GWTC-3”. *Physical Review X* **13,** 011048 (Mar. 29, 2023).

164. Owen, B. J. *et al.* “Gravitational waves from hot young rapidly rotating neutron stars”. *Physical Review D* **58,** 084020 (Oct. 1998).

165. Nelemans, G., Yungelson, L. R. & Portegies Zwart, S. F. “The gravitational wave signal from the Galactic disk population of binaries containing two compact objects”. *Astronomy & Astrophysics* **375,** 890–898 (Sept. 2001).

166. Klein, A. *et al.* "Science with the space-based interferometer eLISA: Supermassive black hole binaries". *Physical Review D* **93,** 024003 (Jan. 2016).

167. Mandic, V. & Buonanno, A. "Accessibility of the pre-big-bang models to LIGO". *Physical Review D* **73,** 063008 (Mar. 2006).

168. Carr, B., Kühnel, F. & Sandstad, M. "Primordial black holes as dark matter". *Physical Review D* **94,** 083504 (Oct. 2016).

169. Brito, R. *et al.* "Gravitational wave searches for ultralight bosons with LIGO and LISA". *Physical Review D* **96.** arXiv: 1706.06311. ISSN: 2470-0010, 2470-0029 (Sept. 2017).

170. P. Amaro-Seoane et al. "Laser Interferometer Space Antenna". arXiv:1702.00786. Feb. 2017.

171. A. Buikema et al. "Sensitivity and performance of the Advanced LIGO detectors in the third observing run". *Physical Review D* **102,** 062003. ISSN: 2470-0010, 2470-0029 (Sept. 2020).

172. Gertsenshtein, M. E. "Wave resonance of light and gravitional waves". *Sov Phys JETP* **14,** 84–85 (1962).

173. Ejlli, A., Ejlli, D., Cruise, A. M., Pisano, G. & Grote, H. "Upper limits on the amplitude of ultra-high-frequency gravitational waves from graviton to photon conversion". *The European Physical Journal C* **79,** 1032. ISSN: 1434-6052 (Dec. 2019).

174. Goryachev, M. & Tobar, M. E. "Gravitational wave detection with high frequency phonon trapping acoustic cavities". *Physical Review D* **90,** 102005 (Nov. 2014).

175. Aggarwal, N. *et al.* "Challenges and opportunities of gravitational-wave searches at MHz to GHz frequencies". *Living Reviews in Relativity* **24,** 4. ISSN: 2367-3613, 1433-8351 (Dec. 2021).

176. Detweiler, S. "Pulsar timing measurements and the search for gravitational waves". *The Astrophysical Journal* **234,** 1100–1104 (Dec. 1979).

177. Hobbs, G. *et al.* "TEMPO2: a new pulsar timing package - III. Gravitational wave simulation". *Monthly Notices of the Royal Astronomical Society* **394,** 1945–1955 (Apr. 2009).

178. Sazhin, M. V. "Opportunities for detecting ultralong gravitational waves". *Sov. Astron.* **22,** 36–38 (Feb. 1978).

179. Mashhoon, B. "On the contribution of a stochastic background of gravitationnal radiation to the timing noise of pulsars." *Monthly Notices of the Royal Astronomical Society* **199,** 659–666 (May 1982).

180. Bertotti, B., Carr, B. J. & Rees, M. J. "Limits from the timing of pulsars on the cosmic gravitational wave background." *Monthly Notices of the Royal Astronomical Society* **203,** 945–954 (June 1983).

181. Hellings, R. W. & Downs, G. S. "Upper limits on the isotropic gravitational radiation background from pulsar timing analysis." *The Astrophysical Journal Letters* **265,** L39–L42 (Feb. 1983).

182. Foster, R. S. & Backer, D. C. "Constructing a Pulsar Timing Array". *The Astrophysical Journal* **361,** 300 (Sept. 1990).

183. Kaspi, V. M., Taylor, J. H. & Ryba, M. F. "High-Precision Timing of Millisecond Pulsars. III. Long-Term Monitoring of PSRs B1855+09 and B1937+21". *The Astrophysical Journal* **428,** 713 (June 1994).

184. Jenet, F. A., Hobbs, G. B., Lee, K. J. & Manchester, R. N. "Detecting the Stochastic Gravitational Wave Background Using Pulsar Timing". *The Astrophysical Journal Letters* **625,** L123–L126 (June 2005).

185. Jenet, F. A. *et al.* "Upper Bounds on the Low-Frequency Stochastic Gravitational Wave Background from Pulsar Timing Observations: Current Limits and Future Prospects". *The Astrophysical Journal* **653,** 1571–1576 (Dec. 2006).

186. Yardley, D. R. B. *et al.* "The sensitivity of the Parkes Pulsar Timing Array to individual sources of gravitational waves". *Monthly Notices of the Royal Astronomical Society* **407,** 669–680 (Sept. 2010).

187. J. P. W. Verbiest et al. "The International Pulsar Timing Array: First data release". *Monthly Notices of the Royal Astronomical Society* **458,** 1267–1288 (May 2016).

188. S. Babak et al. "European Pulsar Timing Array limits on continuous gravitational waves from individual supermassive black hole binaries". *Monthly Notices of the Royal Astronomical Society* **455,** 1665–1679 (Jan. 2016).

189. Z. Arzoumanian et al. "The NANOGrav 12.5 yr Data Set: Search for an Isotropic Stochastic Gravitational-wave Background". *The Astrophysical Journal Letters* **905,** L34 (Dec. 2020).

190. Bustamante-Rosell, M. J., Meyers, J., Pearson, N., Trendafilova, C. & Zimmerman, A. "Gravitational wave timing array". *Physical Review D* **105,** 044005 (Feb. 2022).

191. S. Kawamura et al. "The Japanese space gravitational wave antenna: DECIGO". *Classical and Quantum Gravity* **28,** 094011 (May 2011).

192. Maggiore, M. "Gravitational Waves: Volume 2: Astrophysics and Cosmology". ISBN: 0198570899 (Oxford, 2018).

193. Romano, J. D., Hazboun, J. S., Siemens, X. & Archibald, A. M. "Common-spectrum process versus cross-correlation for gravitational-wave searches using pulsar timing arrays". *Phys. Rev. D* **103,** 063027 (6 Mar. 2021).

194. Hils, D., Bender, P. L. & Webbink, R. F. "Gravitational Radiation from the Galaxy". *The Astrophysical Journal* **360,** 75 (Sept. 1990).

195. Ruiter, A. J., Belczynski, K., Benacquista, M. & Holley-Bockelmann, K. "The Contribution of Halo White Dwarf Binaries to the Laser Interferometer Space Antenna Signal". *The Astrophysical Journal* **693,** 383–387 (Mar. 2009).

196. Ruiter, A. J., Belczynski, K., Benacquista, M., Larson, S. L. & Williams, G. "The LISA Gravitational Wave Foreground: A Study of Double White Dwarfs". *The Astrophysical Journal* **717,** 1006–1021 (July 2010).

197. Toonen, S., Nelemans, G. & Portegies Zwart, S. "Supernova Type Ia progenitors from merging double white dwarfs. Using a new population synthesis model". *Astronomy & Astrophysics* **546,** A70 (Oct. 2012).

198. Lamberts, A. *et al.* "Predicting the LISA white dwarf binary population in the Milky Way with cosmological simulations". *Monthly Notices of the Royal Astronomical Society* **490,** 5888–5903 (Dec. 2019).

199. Korol, V., Hallakoun, N., Toonen, S. & Karnesis, N. "Observationally driven Galactic double white dwarf population for LISA". *Monthly Notices of the Royal Astronomical Society* **511,** 5936–5947 (Apr. 2022).

200. Robson, T., Cornish, N. J. & Liu, C. "The construction and use of LISA sensitivity curves". *Classical and Quantum Gravity* **36,** 105011 (May 2019).

201. Sesana, A., Vecchio, A. & Colacino, C. N. "The stochastic gravitational-wave background from massive black hole binary systems: implications for observations with Pulsar Timing Arrays". *Monthly Notices of the Royal Astronomical Society* **390,** 192–209 (Oct. 2008).

202. K. Aggarwal et al. "The NANOGrav 11 yr Data Set: Limits on Gravitational Waves from Individual Supermassive Black Hole Binaries". *The Astrophysical Journal* **880,** 116 (Aug. 2019).

203. Seto, N., Kawamura, S. & Nakamura, T. "Possibility of Direct Measurement of the Acceleration of the Universe Using 0.1 Hz Band Laser Interferometer Gravitational Wave Antenna in Space". *PRL* **87,** 221103 (Nov. 2001).

204. Maggiore, M. *et al.* "Science case for the Einstein telescope". *Journal of Cosmology and Astroparticle Physics* **2020,** 050 (Mar. 2020).

205. Yagi, K. & Seto, N. "Detector configuration of DECIGO/BBO and identification of cosmological neutron-star binaries". *Physical Review D* **83,** 044011 (Feb. 2011).

206. Isoyama, S., Nakano, H. & Nakamura, T. "Multiband gravitational-wave astronomy: Observing binary inspirals with a decihertz detector, B-DECIGO". *Progress of Theoretical and Experimental Physics* **2018,** 073E01 (July 2018).

207. Abbott, B. P. et al. "Multi-messenger Observations of a Binary Neutron Star Merger". *The Astrophysical Journal Letters* **848,** L12 (Oct. 2017).

208. Nelemans, G., Portegies Zwart, S. F., Verbunt, F. & Yungelson, L. R. "Population synthesis for double white dwarfs. II. Semi-detached systems: AM CVn stars". *Astronomy & Astrophysics* **368,** 939–949 (Mar. 2001).

209. Nissanke, S., Vallisneri, M., Nelemans, G. & Prince, T. A. "Gravitational-wave Emission from Compact Galactic Binaries". *The Astrophysical Journal* **758,** 131 (Oct. 2012).

210. King, A. "How big can a black hole grow?" *Monthly Notices of the Royal Astronomical Society* **456,** L109–L112 (Feb. 2016).

211. Dullo, B. T., Graham, A. W. & Knapen, J. H. "A remarkably large depleted core in the Abell 2029 BCG IC 1101". *Monthly Notices of the Royal Astronomical Society* **471,** 2321–2333 (Oct. 2017).

212. Dullo, B. T. "The Most Massive Galaxies with Large Depleted Cores: Structural Parameter Relations and Black Hole Masses". *The Astrophysical Journal* **886,** 80 (Dec. 2019).

213. Wang, S., Wang, Y.-F., Huang, Q.-G. & Li, T. G. F. "Constraints on the Primordial Black Hole Abundance from the First Advanced LIGO Observation Run Using the Stochastic Gravitational-Wave Background". *Physical Review Letters* **120.** arXiv: 1610.08725, 191102. ISSN: 0031-9007, 1079-7114 (May 2018).

214. Carr, B. J. & Hawking, S. W. "Black holes in the early Universe". *Monthly Notices of the Royal Astronomical Society* **168,** 399–416. ISSN: 0035-8711 (Aug. 1974).

215. Siemens, X., Mandic, V. & Creighton, J. "Gravitational-Wave Stochastic Background from Cosmic Strings". *Physical Review Letters* **98,** 111101 (Mar. 2007).

216. Ito, A. & Soda, J. "MHz Gravitational Waves from Short-term Anisotropic Inflation". *Journal of Cosmology and Astroparticle Physics* **2016.** arXiv: 1603.00602, 035–035. ISSN: 1475-7516 (Apr. 2016).

217. Bisnovatyi-Kogan, G. S. & Rudenko, V. N. "Very high frequency gravitational wave background in the universe". *Classical and Quantum Gravity* **21,** 3347–3359. ISSN: 0264-9381, 1361-6382 (July 2004).

218. Raidal, M., Vaskonen, V. & Veermäe, H. "Gravitational Waves from Primordial Black Hole Mergers". *Journal of Cosmology and Astroparticle Physics* **2017.** arXiv: 1707.01480, 037–037. ISSN: 1475-7516 (Sept. 2017).

219. Arvanitaki, A. & Geraci, A. A. "Detecting high-frequency gravitational waves with optically-levitated sensors". *Physical Review Letters* **110.** arXiv: 1207.5320, 071105. ISSN: 0031-9007, 1079-7114 (Feb. 2013).

220. Rosa, J. G. & Kephart, T. W. "Stimulated axion decay in superradiant clouds around primordial black holes". *Physical Review Letters* **120.** arXiv: 1709.06581, 231102. ISSN: 0031-9007, 1079-7114 (June 2018).

221. Martinez Garcia Cors, J. & Kamai, B. L. "Searching for Harmonic Sources Emitting Gravitational Waves at MHz Frequencies". *Classical and Quantum Gravity.* ISSN: 0264-9381, 1361-6382 (July 2020).